Characterization of Single-Sided CdZnTe Strip Detectors for High Energy Astrophysics Applications

BY

Burçin Dönmez

B.S., Middle East Technical University, Ankara, Turkey, 1997
M.S., Middle East Technical University, Ankara, Turkey, 2000

DISSERTATION

Submitted to the University of New Hampshire
in partial fulfillment of
the requirements for the degree of

Doctor of Philosophy

in

Physics

September 2006

This dissertation has been examined and approved.

Dissertation Director, James M. Ryan, Professor of Physics

James Connell, Associate Professor of Physics

Maurik Holtrop, Assistant Professor of Physics

Mark L. McConnell, Associate Professor of Physics

Tomohiko Narita, Assistant Professor of Physics, College of the Holy Cross

Date

Dedication

To my parents

Acknowledgments

I would like to thank my supervisor Professor James Ryan for giving me an opportunity to work with him, and for his guidance and insight throughout the research. It has been a privilege to work for him and to work with him.

I would like to thank John Macri for his guidance, suggestions, discussions and his endless help with the problems that I encountered in the laboratory. I would also like to acknowledge Dr. Richard Miller and Mark Widholm for their helpful discussions and suggestions. I also thank Jason Legere for making my work with CZT more enjoyable.

I thank the committee members for their useful suggestions and helpful comments.

I thank my parents and my sister for their love and constant support for all these years.

This work was financially supported by the National Aeronautics and Space Administration (NASA) under grants NAG5-5327 and NNG05WC25G.

Contents

List of Tables

List of Figures

ABSTRACT

Characterization of Single-Sided CdZnTe Strip Detectors for High Energy Astrophysics Applications

by

Burçin Dönmez
University of New Hampshire, September, 2006

Cadmium zinc telluride (CdZnTe or CZT) was introduced as a new room temperature semiconductor detector due to its good energy resolution, high atomic number, high density and good stopping power in the early 1990s. UNH has focused on developing CZT strip detector designs for astrophysical measurement applications in the 0.05 to 1 MeV photon energy range. This thesis presents characterization efforts of two types of single-sided CZT strip detector: non-charge sharing orthogonal coplanar strip detectors and charge-sharing strip detectors. The characterization includes spectroscopy, imaging, uniformity and efficiency measurements. Measured energy resolutions with both detector designs are better than those obtainable with NaI(Tl), the scintillator detector material most often used in this energy range. The 3-D imaging capabilities of the detectors were studied using collimated 122 keV photons. Spatial resolution is better than the unit cell pitch in the x and y dimension, and less than 1 mm in the z dimension for both designs. The detection efficiency for photopeak events was calculated for the single-sided charge-sharing CZT strip detector. We also report on Monte Carlo simulations (GEANT4 v7.1) to investigate the effect of multi-hits on detector performance for both spectroscopy and imaging. We compare simulation results with data obtained from laboratory measurements and discuss the implications for future strip detector designs.

Chapter 1

Introduction

For astrophysical applications, good sensitivity and spatial resolution with good energy range are essential. Position sensitivity is important for imaging purposes. Good sensitivity requires a large detector area. CZT is a popular choice for high energy astrophysics due to its material properties.

Thermal bremmstrahlung, blackbody radiation, synchrotron emission and inverse Compton scattering are some of the physical processes that produce high energy X-rays. High energy X-ray sources include compact objects such as neutron stars and black holes, gamma-ray bursts, active galactic nuclei and supernova remnants. The spectra of astrophysical sources have important features that can help identify the prevailing physical processes and conditions, such as temperature, density and elemental abundances. Accretion onto compact objects can heat matter to $10^8 - 10^9$ K and produce emission up to hundreds of keV. For example, understanding accretion on black holes is important, because they represent an environment where we can test general relativity.

Gamma-ray bursts (GRBs) are sudden, intense flashes of gamma rays that occur uniformly throughout the universe. Most burst spectra peak in power around 150 keV (Band, 1995). There are two classes of bursts: short, hard events and long (> 2 s), soft spectrum bursts. There has been considerable progress understanding the nature of the long bursts. They are typically observed at high redshifts ($z \approx 1$) and found in star-forming host galaxies. They are most likely produced by the core-collapse explosions of massive stars (van

Paradijs et al., 1995). The story with short bursts is different, because it has been difficult to localize them until the launch of the *Swift* satellite. The isotropic sky distribution and brightness distribution of the short bursts also suggest cosmological origin (Kouveliotou et al., 1993; Schmidt, 2001), where short bursts are the result of merger of compact objects (neutron star - neutron star or neutron star - black hole) binaries (Eichler et al., 1989).

Active galactic nuclei (AGN) appear to be powered by a supermassive black holes with masses between $10^6 - 10^{10} M_\odot$. AGNs show activity throughout the entire range of the electromagnetic spectrum with peak power often occurring in two simultaneous energy bands, typically X-rays and γ-rays.

Observation of nuclear lines such as ^{26}Al, ^{44}Ti and ^{22}Na are also important. ^{26}Al (1.809 MeV) can be used to study the galactic star-formation regions. Many candidate ^{26}Al sources in our galaxy include novae, Wolf-Rayet stars, red giants and energetic cosmic-ray particle interactions (Prantzos and Diehl, 1996). ^{44}Ti (1.157 MeV) is produced by the supernova events and the existence of the decay product ^{44}Ca makes this production mandatory (Knödlseder and Vedrenne, 2000). First discovery of this kind is made by Iyudin et al. (1994).

A major goal in developing high energy astrophysics X- and γ-ray instruments is to combine good detector spectral resolution for spectroscopy and good position sensitivity for imaging. Monolithic silicon (Si) and germanium (Ge) have good spectral resolution but imaging capabilities are poor because the spatial resolution is the physical dimension of the detector. On the other hand, Anger cameras (Anger, 1958) and scintillation arrays can have good position resolution but their energy resolution is seldom better than 7% at 662 keV. Much research is now being conducted to combine spectroscopy and imaging into one instrument. This includes the use of Si strip detectors, segmented high purity germanium detectors (HpGe), cadmium telluride (CdTe) and cadmium zinc telluride (CdZnTe).

CdZnTe can be made up in planar geometry, pixellated or strip detectors. This is also true for both Si and Ge detectors.

The first semiconductor detectors using Ge surface barrier devices with gold electrodes were fabricated in the late 1950s. These devices were solid state analogues of gas-filled detectors. Solid state devices have great advantages over gas-filled detectors. For detectors of equal stopping power, detector dimensions are much smaller due to the high densities of solid materials. Also, the stopping power is greatly increased with the semiconductor detectors due to their higher atomic number (Z). Scintillation detectors also provide a solid detection medium, but relatively poor energy resolution is their main limitation. The energy required to produce a photoelectron is 100 eV or more in scintillation detectors viewed by photomultiplier tubes. For gas detectors this number is about 30 eV. This limits the achievable energy resolution for gas-filled and scintillation detectors. To reduce the statistical limits on energy resolution, one must increase the number of charge carriers. Semiconductor detectors with low ionization energy (3 to 5 eV per photoelectron) result in a larger number of charge carriers for an incident radiation event, more than either gas-filled or scintillation detectors.

Semiconductor detectors thus have an advantage over scintillation detectors, when the energy resolution is most important. For this purpose, lithium drifted silicon (Si(Li)) and germanium (Ge) are commonly used for gamma-ray spectroscopy. The main drawback with these materials is that they must be operated at low temperature to keep thermal noise to a minimum. Another problem with silicon is its low atomic number. This reduces the efficiency of silicon detectors at high energies and limits their use in gamma-ray astronomy. Because silicon and germanium must be cooled, they can be heavy and consume power. Thus, a search for new semiconductor materials was started in the early 1970s. Cadmium telluride (CdTe) and mercuric iodide (HgI_2) were the first materials to have been operated

successfully at room temperature (Whited and Schieber, 1979). Their high atomic number also increases their efficiency. The main drawback of CdTe and HgI_2 is relatively poor charge carrier mobilities, especially for holes. A short discussion about Si, Ge, CdTe and HgI_2 will be given in Chapter 2.

More recently, cadmium zinc telluride (CdZnTe) was introduced as a new candidate for a room temperature spectrometer (Butler et al., 1992). It has similar gamma-ray absorption efficiency to CdTe, but its larger band gap reduces the operating leakage current. CdZnTe detectors have shown great improvement in gamma-ray spectroscopy over other room temperature semiconductor detectors. However, typical planar CdZnTe detectors show low energy tailing from hole losses during transport. This means that induced charge can not be fully collected and incident photon energy is not calculated correctly. A variety of geometric designs have been fabricated for CdZnTe detectors, such as pixellated and single-sided strip detectors. CdZnTe detectors have been used for nuclear medicine, homeland security and astrophysics applications.

The main aim in nuclear medicine applications is to achieve a high detection efficiency with good energy resolution (Verger et al., 2001) and spatial resolution. Detection efficiency determines the examination times required for imaging and in some cases, patient's radiation dosage. More information about medical applications of CdZnTe can be found in Verger et al. (2001), El-Hanany et al. (1999), Parnham et al. (2001) and Mueller et al. (2003). Small detectors with good energy resolution are used in homeland security applications.

CZT is a good choice for gamma-ray line spectroscopy to study astrophysical sources and objects because of its high atomic number and density. Good spectral resolution of CZT is also important resolving nuclear lines and measuring the line profiles.

CZT can be used as a detector in the following instrument and telescope systems:

1. **Coded mask telescopes**

Coded mask telescopes include a detector array and a coded mask (Caroli et al., 1987) located some distance in front of the detector. The coded mask is made of cells arranged in a particular pattern of open and opaque regions. A point source at infinity will produce a distinct shadow on the position sensitive detector. This information (shadow pattern) is deconvolved to determine the source position and intensity.

The burst alert telescope (BAT) on board *Swift* uses 32,768 pieces of $4 \times 4 \times 2$ mm CZT detector. The BAT has a D-shaped coded mask, made of about 54,000 Pb tiles mounted 1 m in front of the detector plane. *Swift* is a multiwavelength observatory for GRB astronomy that was launched in 2004. A detailed description of *Swift* can be found in Gehrels et al. (2004).

Another example use of CZT detectors as a coded mask telescope is the high-energy telescope (HET) on board of the energetic X-ray imaging telescope (EXIST). EXIST is a conceptual instrument and is being studied for the proposed black hole finder probe (Grindlay, 2005). The HET is an array of coded aperture telescopes with ~ 6 m^2 of imaging CZT.

2. **Focusing X-ray telescopes**

This type of telescope uses a long focal length mirror to focus X-rays. This results in much better angular resolution and sensitivity compared to non-focusing techniques, but the field of view is very limited. This technique uses nested parabolic and hyperbolic surfaces to focus X-rays with a position sensitive detector at the focal point. SIMBOL-X, on the drawing boards, will consists of two spacecraft, one with a mirror to focus X-rays and the other with the detector system 20-30 m away from the mirror (Fernando et al., 2006). The SIMBOL-X mission will use CZT detector system as focal plane detector.

Another example instrument of this kind is *NuSTAR* (Koglin et al., 2005). It consists

of an array of three aligned hard X-ray telescopes. Mirrors focus onto a solid-state pixel detectors, separated by a mast that extends the focal length to 10 meters after lunch.

3. **Compton telescopes**

   The basic Compton telescope consist of two layers, a forward detector to Compton scatter the photons and a calorimeter to absorb the scattered photons. The forward scatterer consists of low Z material to increase the probability of Compton scattering, while the calorimeter is often made up of high Z material to favor photoelectric absorption. Since CZT has high Z and high stopping power, it can be used as the calorimeter in Compton telescopes.

In this thesis, we will discuss the characterization efforts of CZT detectors. In Chapter 2, we will discuss the interaction of photons with matter. The basic idea of semiconductor detector operation is also given. The next chapter presents a brief history of CZT detector evolution. Chapter 4 explains the laboratory work on UNH's single-sided CZT strip detectors. This work consists of spectroscopy, uniformity, imaging, depth measurement and efficiency measurements. The effect of multi-hits on strip detector performance is given in Chapter 5.

Chapter 2

Theoretical Background

2.1 Introduction

This chapter consists of two parts. The first part, briefly discusses the interaction processes of gamma rays with matter which are photoelectric absorption, Compton scattering and pair production. The second part summarizes basic semiconductor detector operation. Properties of semiconductor materials used as a detector is also discussed. These materials include silicon (Si), germanium (Ge), mercuric iodide (HgI_2), cadmium telluride (CdTe) and cadmium zinc telluride (CdZnTe).

2.2 Interaction of Photons with Matter

There are three main interaction processes of high energy photons with matter. These are the photoelectric effect, Compton scattering and pair production. In each of these processes the incident gamma-ray photon transfers some or all of its energy to the electron in the material. The energy of the incident photon (E_γ) and the atomic number (Z) of the material determine which process will dominate. Figure 2-1 shows the relative importance of these loss mechanisms for gamma rays as a function of incident photon energy and the atomic number of the material. In this thesis, photoelectric absorption and Compton scattering are more important than the pair production due to the energy range of interest and the properties of CdZnTe material.

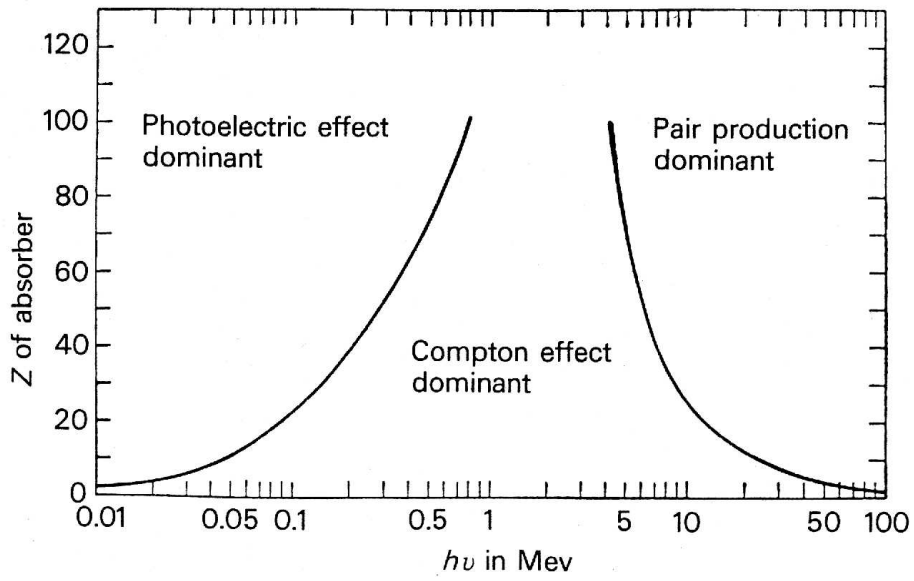

Figure 2-1: The relative importance of different types of energy loss mechanisms for gamma rays as a function of photon energy and the atomic number of the material (Evans, 1955).

2.2.1 Photoelectric Absorption

Photoelectric (or bound-free) absorption is the dominant process for photons at low energies, $E_\gamma = h\nu \ll m_e c^2$. In this process, the incident gamma-ray photon is absorbed and a photoelectron is produced. If the incident gamma-ray photon energy is greater than the electron binding energy E_b, the electron is ejected from the atom. The ejected electron will have kinetic energy equal to the difference between the incident photon energy and the binding energy of the electron in its original shell, i.e. $E_k = E_\gamma - E_b$.

For typical gamma energies, the photoelectron is most likely to come out from the K-shell of the atom, i.e. from the 1s level. The typical binding energies range from a few keV for low-Z materials to tens of keV for high-Z materials. Since the electron is ejected from its shell, there will be a vacancy in its place. This vacancy is quickly filled by capture of a free electron from the medium and/or rearrangement of electrons from the outer shells of the atom. Therefore, one or more characteristics X-ray photons are generated. In most cases, these X-ray photons are not able to escape from the detector volume, and the total

incident photon energy is transmitted to the medium. In the case where the interaction is near a detector surface, escape of these X-rays results in a characteristic escape peak in the spectrum.

The photoelectric absorption is the dominant interaction process for gamma-rays of relatively low energy (see Figure 2-1). The atomic number Z of the material is also very important. The cross-section for photoelectric absorption is

$$\sigma = 4\sqrt{2}\sigma_T \alpha^4 Z^5 \left(\frac{m_e c^2}{E_\gamma}\right)^{3.5} \propto \frac{Z^5}{E_\gamma^{3.5}} \tag{2.1}$$

where α is the fine structure constant, $\alpha = e^2/4\pi\epsilon_0\hbar c$ and σ_T is the Thomson cross-section, $\sigma_T = 8\pi r_e^2/3 = e^2/6\pi\epsilon_0^2 m_e^2 c^4$ and r_e is the classical radius of the electron (Longair, 1992). Due to the strong Z dependence, heavy elements make an important contribution to the absorption cross section.

2.2.2 Compton Scattering

In Compton scattering only a part of the incident photon energy is transferred to the electron that is assumed to be initially at rest (see Figure 2-2). The remaining energy is carried away by the scattered photon. The scattered electron, as in the case of a photo-electron, loses its energy mainly by ionization of atoms along its trajectory. The scattered photon may also interact with the medium by a subsequent Compton scattering or by a photoelectric absorption or by pair production if energy is high enough. The directions of the incident and the scattered photon are determined by the conservation of momentum and energy.

The initial electron four-momentum is $\boldsymbol{P_e^i} = (m_e c, \mathbf{0})$. The initial photon four-momentum is $\boldsymbol{P_\gamma^i} = (E_\gamma^i/c)(1, \hat{\boldsymbol{u}})$. The four-momentum of electron and photon after the collision is given by $\boldsymbol{P_e^f} = (E_e^f/c, \boldsymbol{p})$ and $\boldsymbol{P_\gamma^f} = (E_\gamma^f/c)(1, \hat{\boldsymbol{u}}')$, respectively.

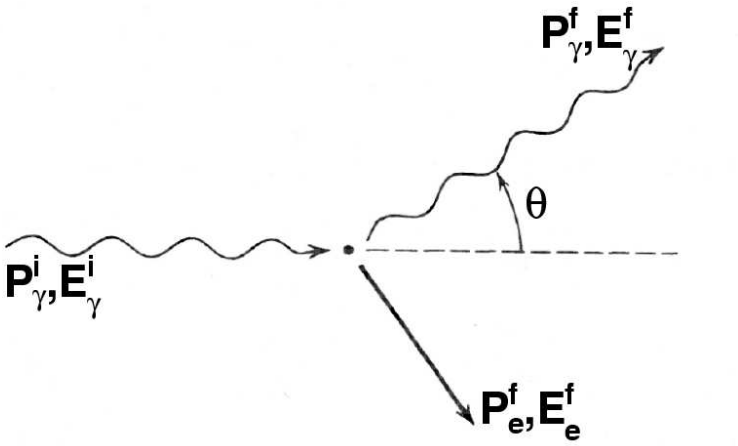

Figure 2-2: Geometry of Compton scattering of a photon by an electron initially at rest (Rybicki and Lightman, 1979).

Conservation of four-momentum gives

$$\boldsymbol{P_e^i} + \boldsymbol{P_\gamma^i} = \boldsymbol{P_e^f} + \boldsymbol{P_\gamma^f}. \tag{2.2}$$

Now, solving equation (2.2) for $\boldsymbol{P_e^f}$ and squaring gives

$$(\boldsymbol{P_e^f})^2 = (\boldsymbol{P_e^i} + \boldsymbol{P_\gamma^i} - \boldsymbol{P_\gamma^f})^2 \text{ (Rybicki and Lightman, 1979).} \tag{2.3}$$

Since, the collision is elastic, we have $(\boldsymbol{P_e^i})^2 = (\boldsymbol{P_e^f})^2$. We also have $(\boldsymbol{P_\gamma^i})^2 = (\boldsymbol{P_\gamma^f})^2 = 0$. Then, equation (2.3) can be written as

$$\boldsymbol{P_\gamma^i P_e^i} - \boldsymbol{P_\gamma^i P_\gamma^f} - \boldsymbol{P_e^i P_\gamma^f} \Longrightarrow \boldsymbol{P_e^i}(\boldsymbol{P_\gamma^i} - \boldsymbol{P_\gamma^f}) = \boldsymbol{P_\gamma^i P_\gamma^f}. \tag{2.4}$$

But in the frame where the electron is initially at rest,

$$\boldsymbol{P_e^i}(\boldsymbol{P_\gamma^i} - \boldsymbol{P_\gamma^f}) = m_e c \left(\frac{E_\gamma^i}{c} - \frac{E_\gamma^f}{c} \right) = m_e (E_\gamma^i - E_\gamma^f), \tag{2.5}$$

$$\boldsymbol{P_\gamma^i P_\gamma^f} = \frac{E_\gamma^i}{c}\frac{E_\gamma^f}{c}(1 - \hat{\boldsymbol{u}}.\hat{\boldsymbol{u}}') = \frac{E_\gamma^i E_\gamma^f}{c^2}(1 - \cos\theta). \tag{2.6}$$

Substituting equation (2.5) and (2.6) into equation (2.4) and solving for E_γ^f gives

$$E_\gamma^f = \frac{E_\gamma^i}{1 + \dfrac{E_\gamma^i}{m_e c^2}(1 - \cos\theta)} \tag{2.7}$$

where θ is the scattering angle of the photon. The kinetic energy of the electron is simply given by the photon's kinetic energy difference before and after the scattering

$$E_e^f = E_\gamma^i - E_\gamma^f = \frac{{E_\gamma^i}^2}{m_e c^2}\frac{1 - \cos\theta}{1 + (E_\gamma^i/m_e c^2)(1 - \cos\theta)}. \tag{2.8}$$

There are two extreme cases for Compton scattering. The first extreme is scattering at very small angles, $\theta \sim 0$. In this case, the scattered gamma ray photon has nearly the same energy as the incident gamma ray photon ($E_\gamma^f \sim E_\gamma^i$) and the electron has very little energy ($E_e^f \sim 0$). The second extreme is a head-on collision, $\theta = \pi$. In this case, the incident gamma ray photon backscatters toward its direction of origin, whereas the electron recoils along the direction of incidence. This case represents the maximum kinetic energy (the 'Compton Edge') that can be transferred to an electron in a single Compton scattering. For $E_\gamma^i \gg m_e c^2$, the maximum electron energy is $E_e^f = m_e c^2/2$.

The dependence of the differential cross section on the scattering angle θ is given by the *Klein-Nishina formula*

$$\frac{\mathrm{d}\sigma}{\mathrm{d}\Omega} = \frac{1}{2} r_e^2 \frac{E_\gamma^f}{E_\gamma^i}\left(\frac{E_\gamma^i}{E_\gamma^f} + \frac{E_\gamma^f}{E_\gamma^i} - \sin^2\theta\right) \tag{2.9}$$

where $r_e (= e^2/m_e c^2)$ is the classical electron radius, and $\mathrm{d}\Omega$ is the element of solid angle around direction θ. The total cross section is approximately given by (Léna et al., 1998)

$$\sigma \propto Z E^{-1}. \tag{2.10}$$

2.2.3 Pair Production

If the incident photon has energy greater than $2m_ec^2$ (1.022 MeV), it is possible to produce an electron-positron pair in the electric field of the nucleus. If the incident photon energy is larger than this value, the excess is shared between the electron-positron pair as kinetic energy. During propagation, these particles lose their energy, mainly by ionization, bremsstrahlung and the Cherenkov effect. Once its energy is very low ($\approx$ 1 keV), the positron will annihilate with an electron in the medium. Then, two photons of energy 511 keV will be created, if the density of the medium is great enough. These photons may escape, or they may interact with the medium, by Compton scattering or photoelectric absorption.

The total cross-section for pair production is given by (Longair, 1992)

$$\sigma \propto \alpha\sigma_T Z^2. \tag{2.11}$$

2.3 Semiconductor Detectors

All solid-state[1] (semiconductor) detectors consist of a semiconducting material, subdivided by impurity doping into regions of different conductivity (junction diode detector) or intrinsic compound semiconductors, in which a charge collecting electric field can be established between the surface contacts. In this study, we worked with the intrinsic compound semiconductor detectors.

[1]Detailed information on semiconductor detectors can be found in Fraser (1989) chapter 4, Leo (1994) chapter 10 and Knoll (2000) chapters 11, 12 and 13.

2.3.1 Basic Operation Principles

The basic operation of semiconductor detectors is similar to ionization gas detectors. Instead of a gas, the medium is a solid semiconducting material. The ionizing radiation creates electron-hole pairs which then drift in an applied electric field. The main advantage of semiconductor detectors over other detectors is that the ionization energy (w) required to create an electron-hole pair is small, of order 3-5 eV. The ionization energy depends on the nature of the incident radiation and temperature. If the energy of the incident radiation is E, many charge carriers will be created, $N = E/w$. A large value of N is important for obtaining better energy resolution with semiconductor detectors, because, statistical fluctuation in the number of carriers per energy becomes a smaller fraction of the total as the number increases. The non statistical variation in the number of charge carriers is also an important parameter for energy resolution. The Fano factor F (Fano, 1946; Fano, 1947) is introduced to adjust for the difference between the observed variance to the Poisson predicted variance and it is given by

$$F = \frac{\text{observed statistical variance}}{E/w}. \tag{2.12}$$

For good energy resolution, the Fano factor should be small. It is measured by eliminating all other factors causing degraded energy resolution, such as electronic noise.

When a particle deposits its energy in a semiconductor detector, N electron-hole pairs are created. The electrons and holes move to the appropriate electrode depending on the direction of the applied electric field. This movement creates a current that will last until all charge carriers are collected at the electrodes. The output pulse in semiconductor detectors relies on the collection of both electrons and holes to measure the deposited energy of the incident particle. Therefore, the mobility of the charge carriers plays an important role in

the performance of the detector. The electron and hole drift velocities in a uniform electric field E are given by

$$\begin{aligned} v_e &= \mu_e E \\ v_h &= \mu_h E \end{aligned} \tag{2.13}$$

where μ_e and μ_h are the electron and hole mobilities, respectively. The mobility of the charge carriers determine the current in a semiconductor. Since the current density $J = \rho v$, where ρ is the charge density and v is the velocity, J in a semiconductor is given by

$$J = en_i(\mu_e + \mu_h)E \tag{2.14}$$

where n_i is the intrinsic carrier density. From Ohm's law, we know $J = \sigma E$, where σ is the conductivity. Comparing with equation (2.14), gives

$$\sigma = en_i(\mu_e + \mu_h). \tag{2.15}$$

Charge carriers in semiconductor materials are subject to trapping or recombination that may degrade the spectroscopic performance of the detector. Impurities in the semiconductor may immobilize electrons or holes, this is known as trapping. Such centers temporarily hold the electron or hole. Impurities in the crystal can also create recombination centers. These centers are capable of capturing both electrons and holes, causing them to recombine. Both mechanisms contribute to finite lifetimes for electrons and holes in the material. The trapping lengths λ_e and λ_h are given by

$$\begin{aligned} \lambda_e &= \mu_e \tau_e E \\ \lambda_h &= \mu_h \tau_h E \end{aligned} \tag{2.16}$$

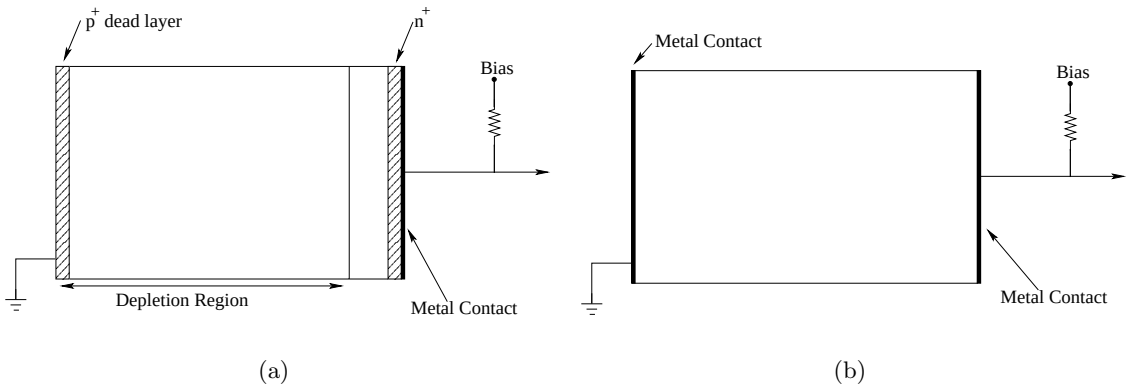

Figure 2-3: Basic structure of a junction diode detector (a) and intrinsic semiconductor detector (b).

where τ_e and τ_h are lifetimes for electrons and holes, respectively. The trapping length represents the average distance that the charge carriers travel before being trapped. Trapping introduces constraints on the geometry of semiconductor detectors. The physical thickness of any detector must be smaller than the trapping length of the charge carriers.

An electric field applied to the detector should be large enough to achieve an efficient charge collection of the carriers from semiconductor detectors. This is achieved by applying a voltage typically hundreds or thousands of volts, across the detector volume. Even in the absence of ionizing radiation, all semiconductor detectors under bias exhibit a conductivity. Therefore, a steady leakage current is observed that directly affects the performance of the detector.

Most practical silicon (Si) and germanium (Ge) detectors consist of reverse biased p-n or p-i-n junction diodes as shown in Figure 2-3(a). The region in the vicinity of the junction is the active volume of the detector which is called the depletion region (or space charge region). Any electron and hole created or entering into this zone is swept out by the electric field. Width of the depletion region, d, can be derived from Poisson's equation and it is given by

$$d \cong \left(\frac{2\epsilon V}{eN}\right)^{1/2} \tag{2.17}$$

where ϵ is the dielectric constant of the medium, V is the applied reverse bias and N is the dopant concentration (either donors or acceptors) on the side of the junction that has a lower dopant level. Because of the fixed charges at the junction, the depletion region has some capacitance given by

$$C = \frac{\epsilon}{d} \cong \left(\frac{e\epsilon N}{2V}\right)^{1/2}. \tag{2.18}$$

For good energy resolution, a small detector capacitance is advantageous. This will also lead the application of larger voltage values.

For compound semiconductor detectors, such as CdZnTe detectors studied for this thesis, the planar configuration as shown in Figure 2-3(b) is used. This configuration consist of two conductive electrodes, usually ohmic, on opposite sides of the crystal. Electron-hole pairs created within the semiconductor will be swept away to the appropriate electrodes under the applied bias voltage. The collected charge on the electrodes is a measure of the incident radiation.

2.3.2 Energy Resolution

The energy resolution (FWHM) of any semiconductor detector can be given by the following quadratic term

$$\Delta E = 2.35(\sigma_N^2 + \sigma_X^2 + \sigma_E^2)^{1/2} \tag{2.19}$$

where σ values are the observed standard deviations due to the effects of carrier statistics (σ_N), charge carrier collection (σ_X) and electronic noise (σ_E). It should be noted that these terms are independent of each other.

The first term on the right is the statistical fluctuations in the number of charge carriers created and given by

$$\sigma_N^2 = FwE \tag{2.20}$$

where F is the Fano factor, w is the energy necessary to create electron-hole pair and E is the energy of the incident radiation.

The second term is due to the incomplete charge collection in the detector. This is always an asymmetric process which deviate pulse height spectra toward lower energy. This effect is usually more important in detectors of large volume and low electric field. Inhomogeneity of the crystal material may also contribute to the energy resolution of the semiconductor detector.

The last term is the broadening due to the all electronic components in the circuit. σ_E is linearly dependent on the input capacitance of the preamplifier. It also depends on the leakage current of the detector.

2.4 Semiconductor Materials Used as Detectors

2.4.1 Silicon (Si) Detectors

Silicon is the most used semiconductor material for charged particle detection. It is widely available and room temperature operation is possible. Properties of silicon can be seen in Table 2.1. Due to its low Z, low density and small resistivity, high energy γ-ray physics applications of silicon are limited. Their relatively small thickness is also a disadvantage. There are different types of detectors:

- **Diffused junction detectors**

  These type of diodes are constructed by treating one surface of p-type material with n-type impurity. A junction is formed at a distance from the surface where n-type and p-type reverse their relative concentration.

- **Surface barrier detectors**

  These type of detectors are formed by creating a junction between a semiconductor and a metal, such as n-type silicon with gold. This type of junction is similar to n-p junction diodes.

- **Ion implanted layers**

  In this type the semiconductor material is bombarded by doping impurities to construct n^+ or p^+ layers. The impurity concentration can be controlled by changing the energy of the beam used to implant the impurities.

- **Lithium drifted silicon (Si(Li)) detectors**

  The previous methods do not provide a sufficient depletion region width. Therefore, a different method is introduced to achieve a thicker silicon detector. The technique of lithium drifting can produce an intrinsic silicon detector up to $5 - 10$ mm.

2.4.2 Germanium (Ge) Detectors

Germanium (Table 2.1) detectors are preferred for γ-ray photon detection applications over silicon detectors due to the its higher atomic number which makes it more effective for γ-ray detection than silicon. However, the main drawback of germanium is the low band gap, requiring that detectors must be operated at low temperatures (77 K). This complicates the electronics and adds cost to detector systems.

Like silicon detectors, germanium detectors made from lithium compensated germanium can provide sufficient gamma-ray detection efficiency. Due to the high mobility of lithium ions in germanium at room temperature, Ge(Li) detectors still must be operated at low temperature.

In the mid 1970s, high purity germanium (HPGe) with very low impurity levels were developed. These detectors do not need cooling to survive, unless high voltage is applied.

2.4.3 Mercuric Iodide (HgI_2) Detectors

A search for room temperature semiconductor detectors began in the 1970s. Mercuric iodide was an attractive material due to the its high atomic number, density and band gap (Table 2.1). The first results with these detectors were published by Malm (1972).

The main problems with these detectors are the poor hole mobility, short lifetime of charge carriers, space charge polarization and surface degradation. These problems degrade the energy resolution of HgI_2 detectors. However, due to its large band gap, the leakage current is low. Therefore, a depletion region is no longer necessary as in Si or Ge detectors.

2.4.4 Cadmium Telluride (CdTe) Detectors

Cadmium telluride is one of the first semiconductor material to has been developed as a room temperature semiconductor detector in the 1970s. Like mercuric iodide, low hole mobility, polarization and a short lifetime of charge carriers is also a problem. Therefore, the energy resolution achieved with Si and Ge cannot be reproduced by CdTe.

Commercially available CdTe detectors range from 1 mm to over 1 cm in diameter and thicknesses up to few millimeters. They are rugged and stable and can be operated at temperatures up to 30^oC.

2.4.5 Cadmium Zinc Telluride (CdZnTe) Detectors

Cadmium zinc telluride has become attractive in recent years. The crystal quality of CdTe is improved by alloying it with ZnTe to form CdZnTe (Butler et al., 1992). The zinc concentration in CdZnTe (CZT) is usually between 0.06 to 0.2, so that its band gap has a range of 1.53 to 1.64 eV. The increased band gap relative to CdTe reduces the intrinsic carrier concentration and the leakage current. However, low hole mobility is still a problem. The differences between the CZT mobility-lifetime ($\mu\tau$) product with those of Si and Ge

can be seen in Table 2.1. These differences leads to incomplete charge collection in CZT detectors which is more severe for holes than electrons. Therefore, the energy spectra of typical planar CZT detectors show a low energy tail (Figure 3-1(a)).

The available crystal size and quality of CZT detectors are still poor compared to HPGe detectors (Bolotnikov et al., 2005). Therefore, crystal quality of CZT must be improved. But, it is better than of CdTe.

CZT detectors are usually operated as electron-only devices (see Chapter 3) to eliminate the effect of holes in charge collection. In these devices, electrons contribute to the output signal. The energy of the incident radiation is directly proportional to this signal.

Table 2.1: Properties of intrinsic semiconductor detector materials. (References: (1) Semiconductor detector materials, eV Products. (2) Knoll (2000) and references therein. (3) (Dabrowski and Huth, 1978). (4) (Takahashi and Watanabe, 2001). (5) (Redus et al., 1997).)

	Si	Ge	HgI_2	CdTe	CdZnTe
Atomic number	14	32	80, 53	48, 52	48, 30, 52
Density (at 300 K), ρ (g/cm^3)	2.33	5.33	6.4	5.85	5.78
Dielectric constant	12	16	8.8	11	10.9
Band gap (at 300 K), E_g (eV)	1.12	0.67	2.13	1.52	1.57
Electron-hole pair creation energy, w (eV)	3.6	2.96 (at 77 K)	4.2	4.43	4.64
Resistivity (at 300 K), ρ (Ω.cm)	2.3×10^5	47	10^{13}	10^9	3×10^{10}
Electron mobility (at 300 K), μ_e (cm^2/V.s)	2.1×10^4 (at 77 K)	3.6×10^4 (at 77 K)	100	1100	1000
Hole mobility (at 300 K), μ_h (cm^2/V.s)	1.1×10^4 (at 77 K)	4.2×10^4 (at 77 K)	4	100	$50 - 80$
Electron lifetime, τ_e (s)	$> 10^{-3}$	$> 10^{-3}$	10^{-6}	3×10^{-6}	3×10^{-6}
Hole lifetime, τ_h (s)	2×10^{-3}	10^{-3}	10^{-5}	2×10^{-6}	10^{-6}
Electron mobility-lifetime, $(\mu\tau)_e$ (cm^2/V)	> 1	> 1	10^{-4}	3.3×10^{-3}	$(3 - 5) \times 10^{-3}$
Hole mobility-lifetime, $(\mu\tau)_h$ (cm^2/V)	≈ 1	> 1	4×10^{-5}	2×10^{-4}	5×10^{-5}
Fano factor (F)	0.16	0.058	$0.46^{(3)}$	$0.15^{(4)}$	$0.082^{(5)}$

Chapter 3

General Review of CZT Detectors

3.1 Introduction

This chapter briefly discusses the evolution of CZT detectors. We shortly talk about the importance of the Shockley-Ramo theorem and weighting potentials. The idea of single polarity charge sensing to eliminate the problem associated with the poor hole collection is discussed. The different anode designs such as coplanar grid, pixellated anode and double-sided strip detectors suggested by the research groups is also given.

3.2 Brief History of CZT Detectors

3.2.1 Background

Various semiconductor materials have been used for gamma-ray spectroscopy. Two materials with good charge transport properties are silicon (Si) ($Z = 14$) and germanium (Ge) ($Z = 32$), and both have been used as detectors since the early 1960s. Because of its small band gap, Ge must be operated at cryogenic temperatures, adding complexity and expense. Therefore, recent research has concentrated on materials with high atomic number and a larger band gap, such as mercuric iodide (HgI_2), cadmium telluride (CdTe), and cadmium zinc telluride ($Cd_{1-x}Zn_xTe$). These materials operate at room temperature and

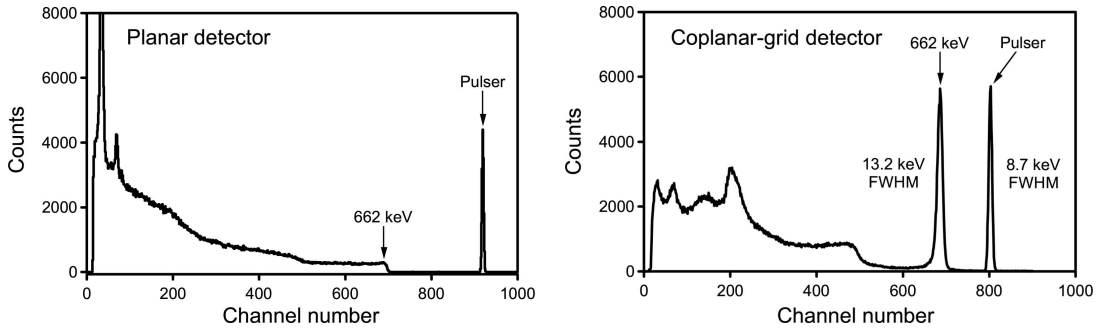

(a) (b)

Figure 3-1: Spectrum of ^{137}Cs obtained with a 1 cm^3 CdZnTe detector in its standard planar configuration and using the coplanar grid detection technique, see section (3.2.3) (Luke et al., 2003). The effect of electrode design on spectroscopic performance can be clearly seen here.

are usable for gamma-ray energies up to several hundred keV that is limited by the thickness of the detector. However, they do not have the desirable charge transport characteristics of Si and Ge. The carrier mobilities are smaller, and the carriers can be trapped at impurities or defects. These effects tend to be more serious for holes than for electrons due to the low hole mobility and high concentrations of hole-trapping defects. Due to the trapping of charges, the output signal of a conventional detector with planar electrodes depends not only on deposited energy but also on the location of that interaction with respect to the anode and cathode planes (depth of interaction). Therefore, the pulse height spectra typically show a low pulse height tail (Figure 3-1(a)), with a large fraction of the events occurring in this tail instead of in the full energy photopeak.

The principle of operation of a gamma-ray spectrometer using semiconductor detectors can be explained as follows. The incident gamma-ray interacts with the semiconductor detector and creates a number of electron-hole pairs proportional to the deposited energy. The movement of these electrons and holes due to the applied electric field within the device causes variations of induced charge on the electrodes. This induced charge is converted to a voltage pulse using a charge sensitive preamplifier. In an ideal case the amplitude of the

voltage pulse is proportional to the deposited energy.

The induced currents due to charge motion in vacuum were found independently by Shockley (1938) and Ramo (1939) who introduced the concept of a *weighting potential*. The Shockley-Ramo theorem can be applied not only to vacuum tubes, where no space charge exists within the apparatus, but also in the presence of stationary space charge (Jen, 1941; Cavalleri et al., 1971).

The Shockley-Ramo theorem states that the charge Q and current i on the electrode induced by a moving point charge q are given by

$$Q = -q\varphi_0(\boldsymbol{x}) \tag{3.1}$$

$$i = q\boldsymbol{v}.\boldsymbol{E}_0(\boldsymbol{x}) \tag{3.2}$$

where $\boldsymbol{v}$ is the instantaneous velocity of moving charge q. $\varphi_0(\boldsymbol{x})$ and $\boldsymbol{E}_0(\boldsymbol{x})$ are called the weighting potential and the weighting field, respectively and both are dimensionless quantities.

The Shockley-Ramo theorem can be proved by using the conservation of energy (He, 2001; Eskin et al., 1999; Hamel and Paquet, 1996). It can be seen that charge induced by moving charge q is independent of voltage applied to the electrodes. This induced charge redistributes on each electrode while the charge q moves, and the change of induced charge on each electrode can be measured using a charge sensitive preamplifier. The charge induced on a given electrode can be found by calculating the weighting potential $\varphi_0(\boldsymbol{x})$. We assume that the 0^{th} electrode is at unit potential, the others are grounded and all the space charge is removed, i.e. the detector material is being replaced by vacuum. Then, the induced charge Q is simply given by equation (3.1). Note that the weighting potential is not a dimensionally correct potential. Instead, it is a normalized quantity representing the charge induced on an electrode resulting from the introduction of a point charge into the detector volume. This

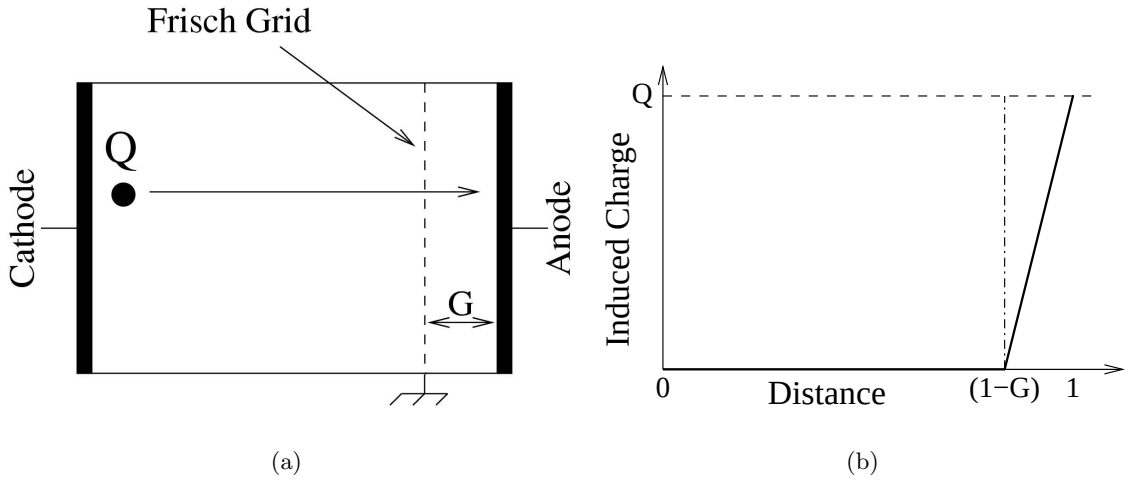

(a) (b)

Figure 3-2: (a) Basic structure of Frisch grid applied to gas and liquid detectors. Grid placed at a distance G measured from anode ($G \ll 1$). (b) Induced charge at the anode as a function of distance traveled by the charge Q. The cathode is at 0 and the anode is at 1.

is convenient for calculating the induced charge on any electrode of interest. Because, with a given configuration of a device and the specified electrode, only one weighting potential needs to be calculated from the Poisson equation. The importance of weighting potential will be clear later.

3.2.2 Single Polarity Charge Sensing

As stated earlier, hole trapping is the main reason for the charge collection problem for conventional planar detectors composed of high Z semiconductor materials. Similar problems exist in gas and liquid detectors due to the much larger mass and therefore low mobility of the positive ions compared to the electrons. The ions are often not fully collected like holes in the semiconductor detectors. For these detectors, the problem is solved by introducing a Frisch grid (Frisch, 1944). The Frisch grid placed at a distance G measured from the anode ($G \ll 1$) as shown in Figure 3-2(a) for a unit length detector. The grid shields the anode electrostatically so that the movement of carriers in the region between the cathode and the grid does not induce any signal at the anode. The entire signal is

generated after the electrons pass through the grid (Figure 3-2(b)). As a result, the carriers generated between the cathode and the grid will produce full amplitude signal as long as the electrons are fully collected at the anode, regardless of whether or not the positive ions are collected at the cathode. When we look to the weighting potential the following scenario can be seen. The weighting potential of the anode is obtained by applying a unit potential on the anode, and zero potential on both the cathode and the grid. The weighting potential is zero between the cathode and the grid, and rises linearly from zero to 1 from the grid to the anode. This means that the charge moving between the cathode and the grid induce no charge on the anode, and only electrons passing through the grid contribute to the anode signal. Therefore, the amplitude of the pulse is only proportional to the number of electrons collected, and any induced signal from the movement of charges between the cathode and the grid, including that from the movement of ions, is eliminated.

3.2.3 Coplanar Grid Electrodes

Single polarity charge sensing to improve spectroscopic performance similar to the Frisch grid method is applied to semiconductor detectors using coplanar electrodes (coplanar grids) (Luke, 1994; Luke, 1995). In this method, a single electrode on the anode is replaced by series of parallel strip electrodes formed on the surface of the detector as shown in Figure 3-3. The strip electrodes are connected interdigitally to give two independent sets of grid signals named as collecting and noncollecting grids. The cathode is biased negatively (V_b) so that electrons drift to the anode electrodes. A slightly positive bias V_g is applied to the collecting grid to ensure that electrons are collected only by this electrode. This bias is small compared to the applied cathode bias so that the electric field inside the detector remains uniform. The noncollecting grid is kept at zero bias.

Figure 3-4(a) shows calculated induced charge signals on the grid electrodes as a function

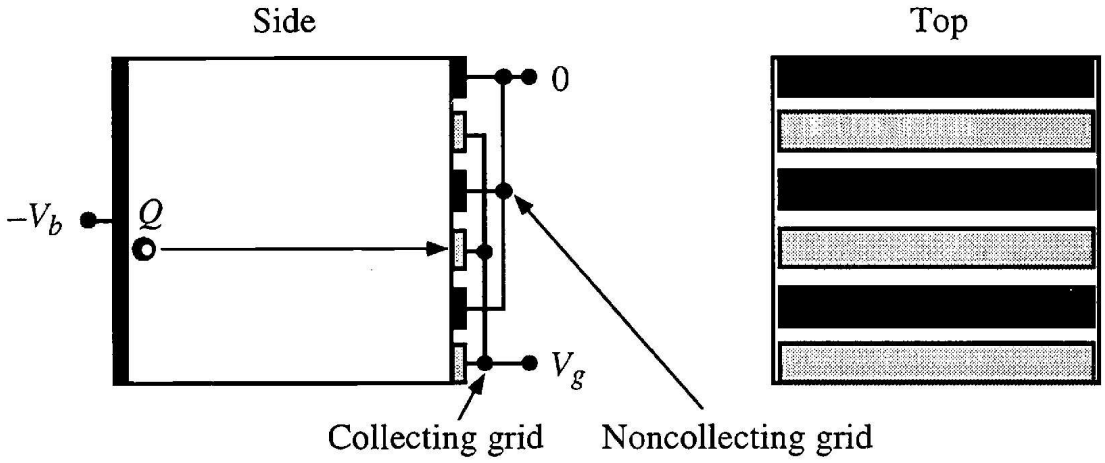

Figure 3-3: Schematic drawing of a coplanar-grid detector (Amman and Luke, 1997).

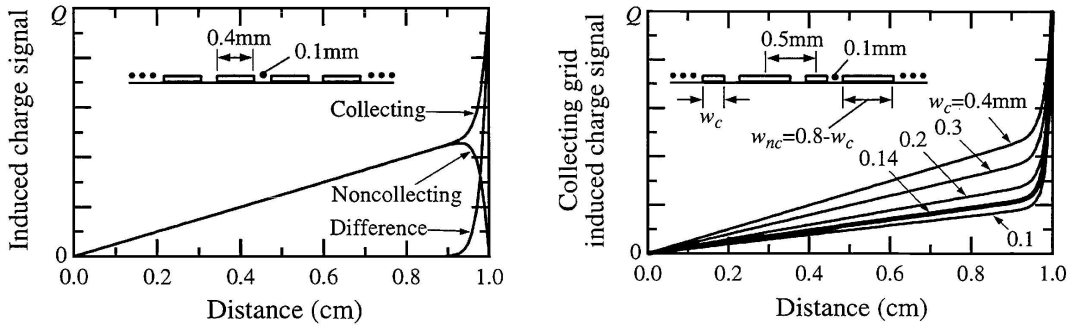

(a) (b)

Figure 3-4: (a) Calculated induced charge signals on the grid electrodes of a coplanar-grid detector as a function of the distance traveled by a charge Q originated near the cathode. The detector thickness is 1 cm. The difference between the collecting and noncollecting grid signals are also plotted. The difference signal is independent of the charge motion through the most of the detector volume. (b) Calculated induced charge signals on the collecting grid electrode by same charge Q. The induced charge signal is shown for different collecting grid line widths, w_c. w_{nc} is the width of the noncollecting grid (Amman and Luke, 1997).

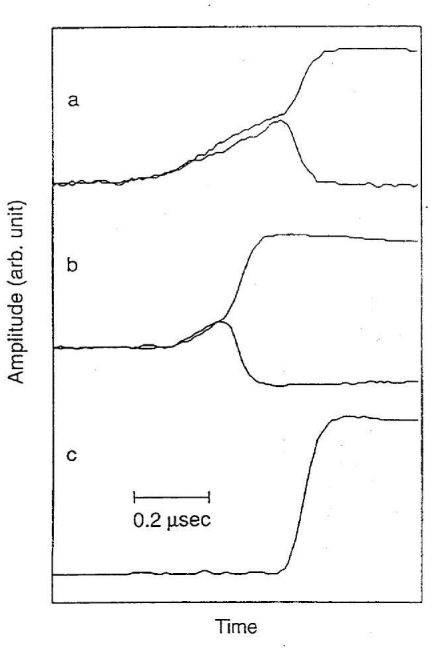

Figure 3-5: (a,b) Charge signals captured simultaneously from the two grid electrodes at two different depth. The signal on collecting grid increases as electrons move towards it. (c) A difference signal obtained from the output of the signal subtraction circuit (Luke, 1994).

of the distance traveled by a charge Q originating near the cathode (Amman and Luke, 1997). Charge trapping is not included in this calculation. The collecting and noncollecting signals are almost identical until the charge drifts near the grids (near-grid region). When the charge Q drifts near the anode, the collecting grid signal increases rapidly to Q and the noncollecting grid signal vanishes. In other words, the weighting potential on the collecting grid increases rapidly to 1, whereas it decreases to zero on the noncollecting electrode. Taking the difference of these two signal one can obtain a resultant signal as shown in Figure 3-4(a). By this method, the signal is derived almost entirely from the movement of electrons, and holes have little effect on signal. Figure 3-5 shows the signals from the collecting and noncollecting grid signal in the detector and a difference signal captured from the output of the signal subtraction circuit. The signal on the collecting electrode increases as electrons move to it. The middle figure (Figure 3-5(b)) shows set of signals where the interaction occurred near the middle of the detector. Since there is negligible contribution

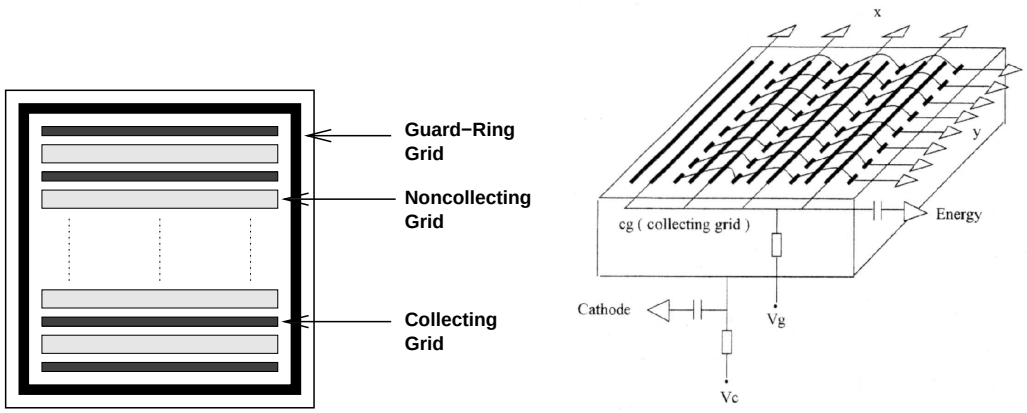

(a) (b)

Figure 3-6: (a) View of the modified grid electrode surface including guard ring. Collecting and noncollecting grid widths are not scaled (Amman and Luke, 1999). (b) Schematic drawing of a 3-D position-sensitive coplanar-grid detector (Luke et al., 2000).

from holes, the signal from the collecting grid is reduced in amplitude while the signal from the noncollecting grid becomes negative with respect to the baseline (Luke, 1994). To simplify the electronics (i.e. not to use signal subtraction), the width of the grid signals are modified to obtain charge collection similar to Figure 3-4(a). Figure 3-4(b) shows induced charge signal on collecting grid for different grid widths. In this method, edge effects play an important role and depending on the lateral position of the induced charge on the collecting grid due to the nonuniformity of the weighting potential distribution. Introducing a guard ring (Figure 3-6(a)) around the collecting grid and the noncollecting grid solves this problem. Because, by adding the guard ring, some of the electrostatic field flux lines that would have terminated on the grid electrodes now terminate on the guard ring. This means that the weighting potential within the device including the edges are more uniform. These detectors are effective, high performance spectrometers, however they do not have imaging capability. Figure 3-1(b) shows a spectrum of CZT detector with coplanar grid electrodes.

Figure 3-6(b) is a schematic drawing of a 3-D position sensitive coplanar-grid detector. Similar to the previous design in Figure 3-6(a), energy readout is accomplished by measuring

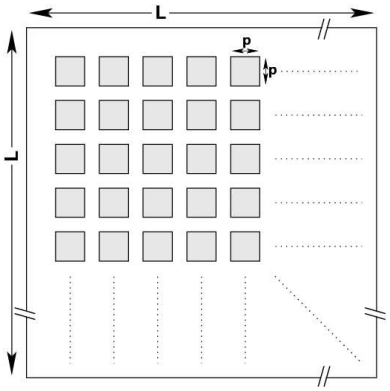

Figure 3-7: Anode pattern of an array of individual square pixels of size $p \times p$. The thickness of the detector is t, where $t \gg p$ and $L \gg t$ (Barrett et al., 1995).

the induced signal on a single set of interconnected anode strips which are biased to collect charge (Luke et al., 2000). Position sensing in the lateral dimensions (x and y) is performed by segmenting the noncollecting grid into a number of elements and measuring the induced signals on these elements as electrons are collected at the collecting grid.

3.2.4 Pixellated Anode Electrodes

A similar method was introduced by Barrett et al. (1995) to eliminate the contribution of holes to the output by creating an array of small elements (pixels) at the anode (Figure 3-7). There is a small gap between the pixel electrodes. Each pixel is connected to a charge sensitive preamplifier for readout. These pixel detectors perform as imagers as well as spectrometers. The induced charge on any small pixel anode from the moving charge q is very small when q is far away from the pixel. The induced charge increases rapidly, when the moving charge is in the vicinity of the anode pixel, i.e. $z \simeq p$, where z is the depth of interaction and p is the pixel size. This is called the *small pixel effect*. The signals generated in pixel detectors depend strongly on electrode geometry (Eskin et al., 1999). The aspect ratio of the pixel volume (pixel width/detector thickness) determines the relative contribution of electron and holes to the total signal. If the aspect ratio is small, (e.g. small

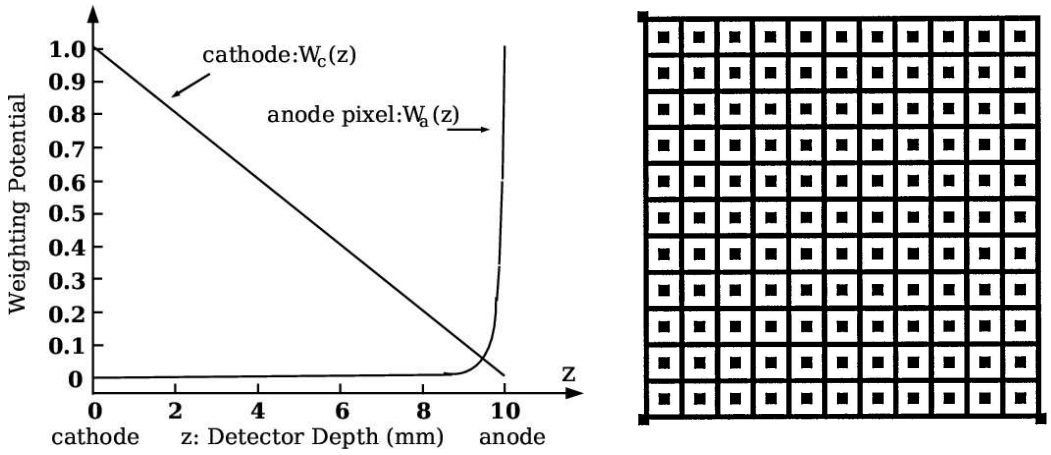

(a) (b)

Figure 3-8: (a) Weighting potentials of the cathode and the anode pixel in a 3-D position sensitive CZT detector (Li et al., 2000). (b) 3-D position sensitive pixellated anode array design by He et al. (1999).

pixels, thick detector) electron-only signals are obtained, and the problem of hole trapping becomes insignificant. Figure 3-8(a) shows the weighting potentials of the cathode and anode pixel in a 3-D position sensitive CZT detector (Li et al., 2000).

Figure 3-8(b) shows a three-dimensional position sensitive semiconductor spectrometer (He et al., 1999). Each collecting pixel anode is surrounded by a noncollecting grid. The noncollecting grid is biased lower than the collecting anodes, so that electrons are guided towards the collecting anodes.

3.2.5 Double-Sided Orthogonal Strip Detectors

Double-sided orthogonal strip detectors have also been proposed for imaging applications (Ryan et al., 1995; Matteson et al., 1996; Stahle et al., 1996). In this method, the anodes collect the charge for spectroscopy and x position, the cathode signal provides the y position (Figure 3-9(a)). Matteson et al. (1996) introduced the idea of steering electrodes between each anode strip as shown in Figure 3-9(b). The steering electrodes are biased

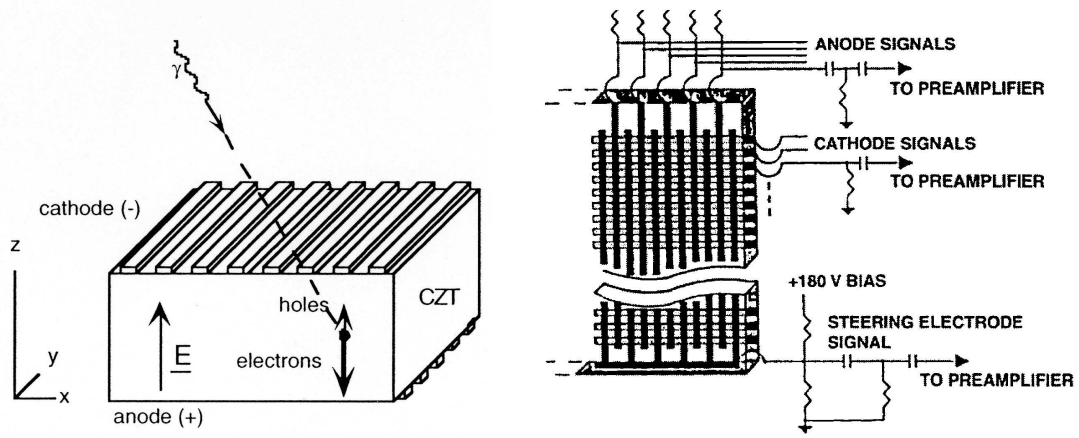

(a) (b)

Figure 3-9: Double sided CZT strip detector designs. (a) UNH (Ryan et al., 1995). (b) UCSD (Matteson et al., 1996).

between the cathode and the anode electrodes to help shape the uniform electric field to improve charge collection on the anode electrodes. This minimizes charge losses in the gaps between the anode electrodes. For this design, good position sensitivity depends on the good collection of electrons on the anode surface and also on the efficient collection of the holes on the cathode surface. Since the drift length of holes is very short ($\sim$ 1 mm) in CdZnTe, the strip readout techniques have only been applied on thin ($\sim$ 2 mm) CdZnTe detectors.

3.3 Importance of Single-Sided CZT Strip Detectors

3.3.1 Pixel vs. Strip Detectors

Both pixel and strip detectors can be designed to take advantage of the "small pixel effect." This effect helps eliminate the contribution of holes to the electronic signal which otherwise degrades the energy resolution.

The main advantage of strip detectors over pixel detectors is the number of channels

used. An $n \times n$ pixel detector (Barrett et al., 1995; He et al., 1999; Barthelmy, 2000) requires n^2 channels whereas a CZT strip detector with n rows and n columns require only $2n$ channels. This feature is most important for large detector arrays because fewer channels reduce the complexity of instrument electronics and thus require less power.

3.3.2 Double-Sided vs. Single-Sided Strip Detectors

The main advantages of single-sided CZT strip detector designs over double-sided strip detectors are as follows.

1. Since all signals are on the one side of the detector, design and fabrication of closely packed arrays is simpler than for double-sided strip detectors where the electrical contacts must be instrumented on both surfaces. These contacts add to dead area in closely packed arrays of imaging modules.

2. Because electron transport is efficient, single-sided strip detectors can be thick up to 10 mm, so they can be used effectively up to 1 MeV. On the other hand, double-sided strip detectors can be fabricated only up to 2 mm thick which limits their use up to 0.2-0.3 MeV (Ryan et al., 1995; Rothschild et al., 2003).

Chapter 4

Single-Sided CZT Strip Detectors

4.1 Introduction

This chapter is about the CZT detector characterization efforts carried out with novel single-sided CZT strip detectors that are orthogonal coplanar and single-sided charge-sharing strip detector designed at UNH. Characterization experiments include measurements of spectroscopic performance at room temperature, imaging capabilities in 3-D, depth measurement, uniformity measurements and photopeak detection efficiency.

4.2 Single-Sided CZT Strip Detector Concepts

The UNH team has developed two single-sided CZT strip detector concepts, orthogonal coplanar CZT strip detector and single-sided charge-sharing CZT strip detector. Prototype detector devices have been designed, built and tested.

4.2.1 Orthogonal Coplanar CZT Strip Detectors

Figure 4-1 illustrates the anode contact pattern of an 8×8 orthogonal coplanar anode strip detector (Jordanov et al., 1999; McConnell et al., 2000). This pattern forms 64 1.0 mm^2 unit cells. A single unit cell, expanded, is shown on the right. There is a 200 μm

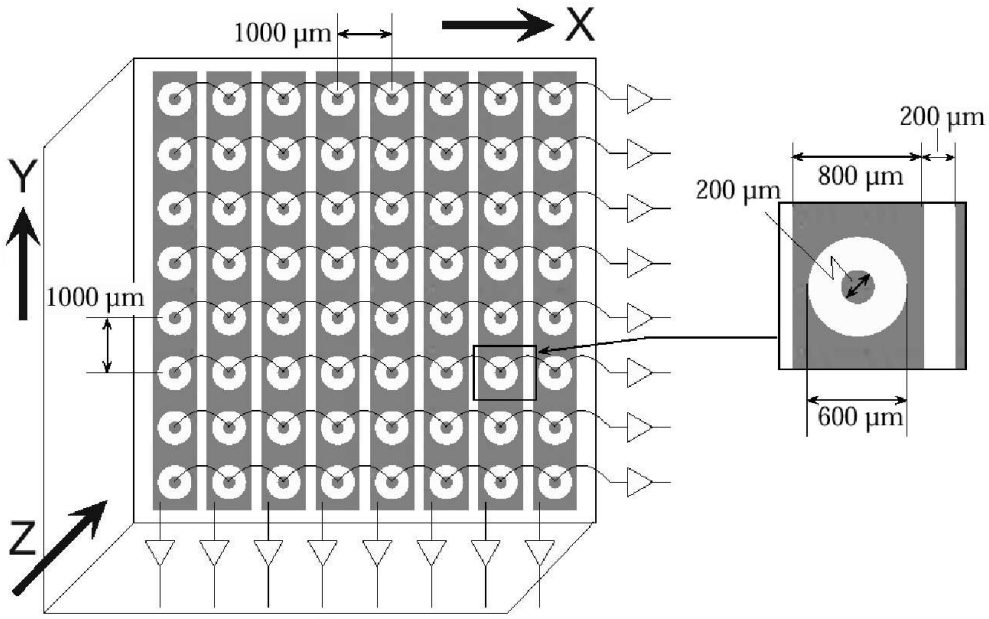

Figure 4-1: Contact geometry and read out of the orthogonal coplanar anode design. Detector dimension is $10 \times 10 \times 5$ mm^3.

diameter pixel contact pad at the center of each unit cell. The gold metallic contacts are shown in gray. Gaps between contact electrodes are 200 μm. The opposite side has a single uniform cathode electrode which is not shown. Detector dimension is $10 \times 10 \times 5\times$ mm^3. In this design, each row takes the form of 8 discrete interconnected anode pixels while each column is a single anode strip. The anode pixel contacts are interconnected in rows and biased (0V) to collect the electron charge carriers. Pixel signals provide the event trigger as well as the energy and the y coordinate. The non-collecting strips, surrounding the anode pixel contacts, are biased (-30V) between the cathode (-800V) and anode pixel potentials. The strips register signals from the motion of electrons as they move towards the pixels and provide the x and z coordinates. For optimum performance, the strip signals should collect no charge because this will degrade the energy resolution. The strip signal is generally bipolar and its amplitude is between 25% and 40% of the pixel signal. Figure 4-2(a) shows the basic features of both the anode pixel and strip signals. Figure 4-2(b) shows

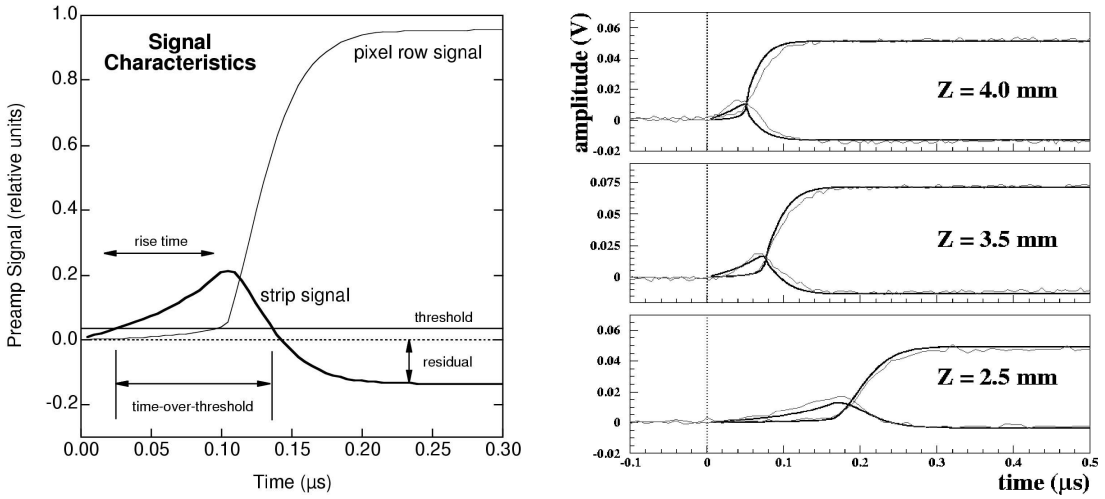

(a) (b)

Figure 4-2: (a) Simulated charge sensitive preamplifier outputs of strip and pixel row signal generated by a single interaction in the CZT. (b) GEANT simulation of events showing pixel and strip signals at three different depths in z, with three measured events showing a strong match (Larson et al., 2000).

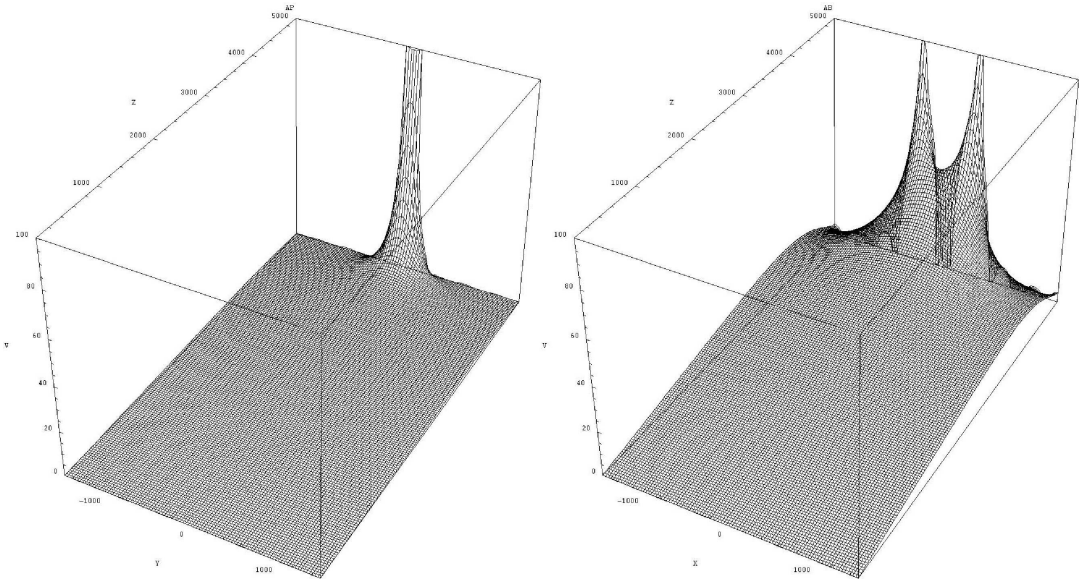

Figure 4-3: Weighting potential of pixels and strips in orthogonal coplanar CZT strip detector design (Julien and Hamel, 2001).

simulated signals for three different depths of interaction, with matching signals taken from the detector (Larson et al., 2000). Similar signals have been observed by Luke (1994) (see Figure 3-5). The pixel signals, rising in only positive direction, are typical of small pixel anodes in CZT detectors. The initial slope of the pixel signals is small but increases rapidly when electrons reach the anode surface (small pixel effect). The strip signals have faster initial rises than the pixel signals due to the larger strip areas and consequently larger weighting potential away from the anode. They reach a maximum shortly before the end of the electron transit time and decrease as the electrons approach the pixel. Since electrons are much more mobile than holes in CZT, signals from photon interactions at all depths in the detector are detected. The third coordinate of the interaction location, depth, can also be measured using the strip signal. There are three features of the strip signal that are functions of the interaction depth, z, these are risetime, time-over-threshold and residual. With this design more compact packaging is possible than with the double-sided strip detectors. Since all imaging contacts and signal processing electronics connections are only on one side of the detector, except for the cathode bias. Calculated weighting potentials for pixel and strip electrodes can be seen in Figure 4-3.

The prototype module assemblies involve the applications of two key technologies: Low Temperature Cofired Ceramics (LTCC) and Polymer Flip-Chip (PFC) bonding (Jordanov et al., 1999). Figure 4-4(a) shows the photograph of a patterned CZT substrate and its mating LTCC carrier. PFC bonding is used for the electrical and mechanical connection of the CZT and LTCC substrates. This technique uses a silver filled conductive epoxy to electrically connect the contacts on the CZT and LTCC surfaces. Conductive polymer bumps are printed onto the gold anode pads of CZT substrate and LTCC carrier. The conductive polymer bumps are approximately 120 μm in diameter and 20 μm in height (Figure 4-5). The surfaces of the detector and carrier are aligned and mated while the

conductive bumps are wet. A non-conducting epoxy is then used to fill all the empty space between CZT and LTCC carrier. The result is a rugged detector module (Figure 4-4(b)) with no wire bonding to the anode plane. The disadvantage is that rows and columns require different signal processing electronics.

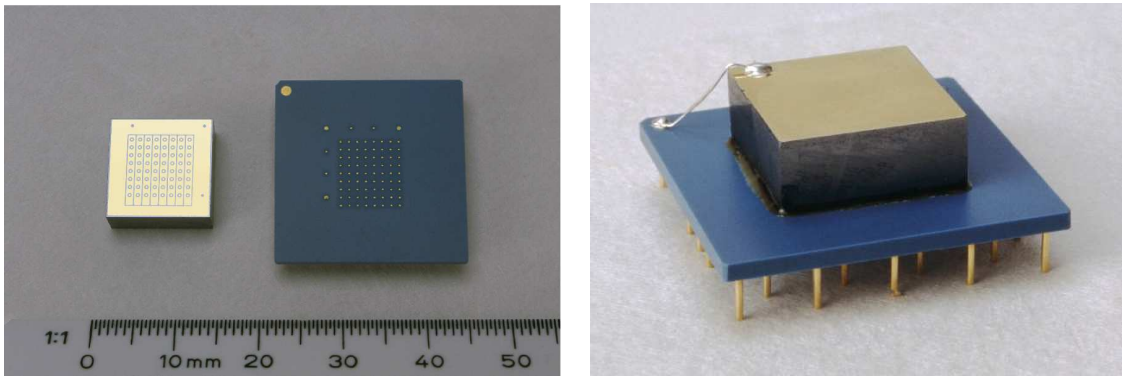

(a) (b)

Figure 4-4: Detector prototype components; a patterned CZT substrate (left) and its mating ceramic (LTCC) carrier (right) (a). 5 mm thick prototype detector module (b).

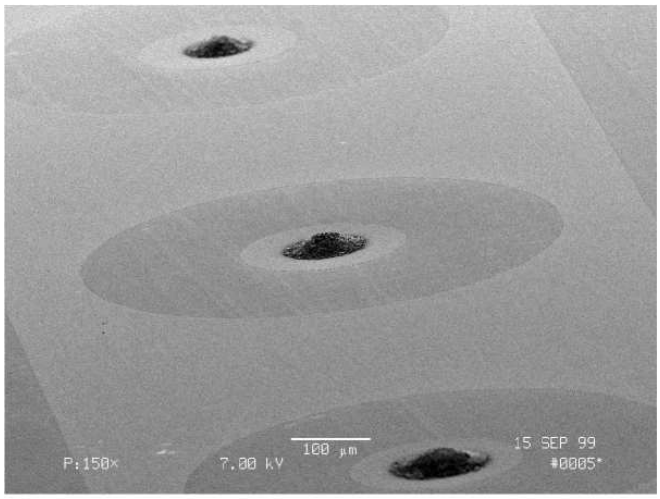

Figure 4-5: Conductive epoxy bumps on the anode surface of the CZT detector (Ryan et al., 2003).

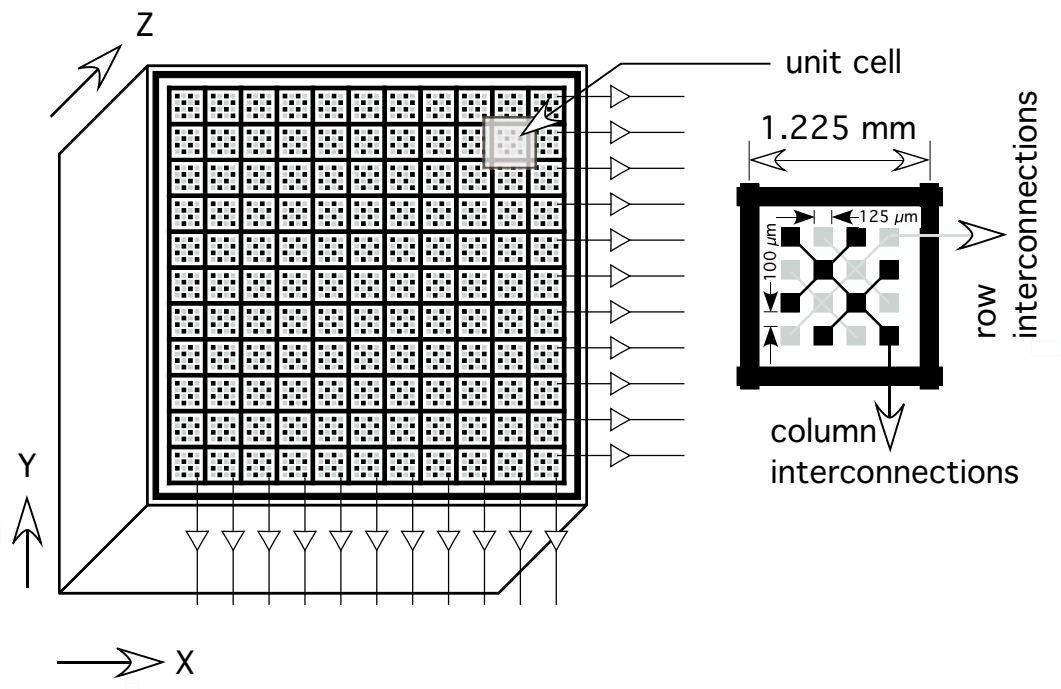

Figure 4-6: Single-sided charge-sharing strip detector (left). Unit cell (right) shows interconnections. Detector dimension is $15 \times 15 \times 7.5$ mm^3.

4.2.2 Single-Sided Charge-Sharing CZT Strip Detectors

Figure 4-6 shows the second UNH single-sided strip detector concept, a single-sided charge-sharing CZT strip detector (Macri et al., 2004). This device has eleven row and eleven column channels (121 "pixels" or "unit cells"). The anode pattern and a readout is shown in Figure 4-6 and a 1.225 mm square unit cell (expanded right) illustrates the pad interconnections. Detector dimension is $15 \times 15 \times 7.5$ mm^3. Each unit cell contains an array of closely packed anode contact pads in two groups (gray and black in this figure). The two groups are identically biased for electron charge collection but are interconnected in columns and rows in the layers of the carrier substrate. Unlike the earlier UNH design (Figure 4-1) rows and columns have identical signal types. A non-collecting grid (z-grid) electrode surrounding each pixel, biased between pixel pad and cathode, provides a signal that can be used for measuring the depth of interaction (the z-coordinate). A single cathode

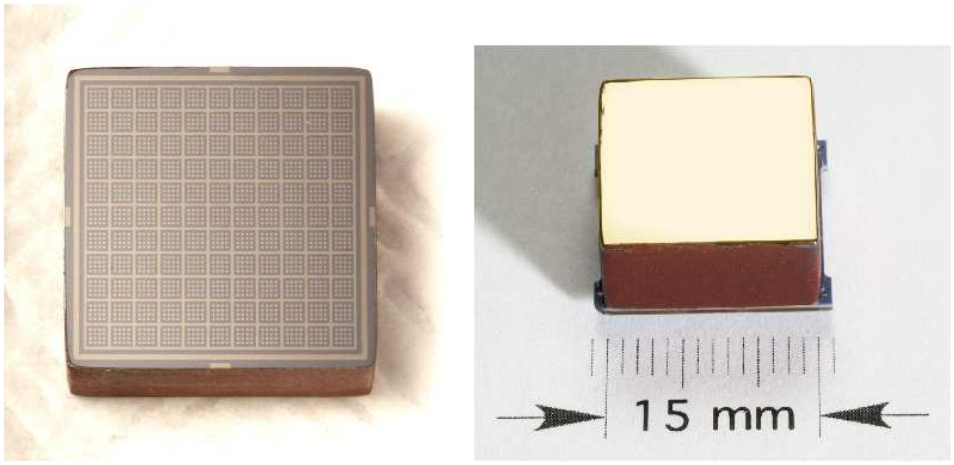

Figure 4-7: Patterned CZT anode surface (left) and prototype detector module assembly showing cathode surface (right). The CZT thickness is 7.5 mm.

contact on the opposite side is not shown. The principle of operation requires a sharing of charge between row and column anode contacts for each event. This is feasible when the pitch size of the anode pads is smaller than the lateral extent of the electron charge cloud reaching the anode surface. This approach takes advantage of the increasing capability of manufacturers to pattern and interconnect fine features. Note that the smallest feature size here, the 100 μm gaps between pads is half that of our earlier orthogonal coplanar strip detector design.

Photographs of the patterned CZT anode surface and a prototype detector module assembly viewed from cathode surface can be seen in Figure 4-7.

4.3 Experimental Setup

4.3.1 Orthogonal Coplanar CZT Strip Detector

Figure 4-8 shows the signal processing arrangement for the study of the orthogonal coplanar CZT strip detectors. The signal processing and data acquisition uses commercially available NIM and VME electronics. Data acquisition (DAQ) software is written in C

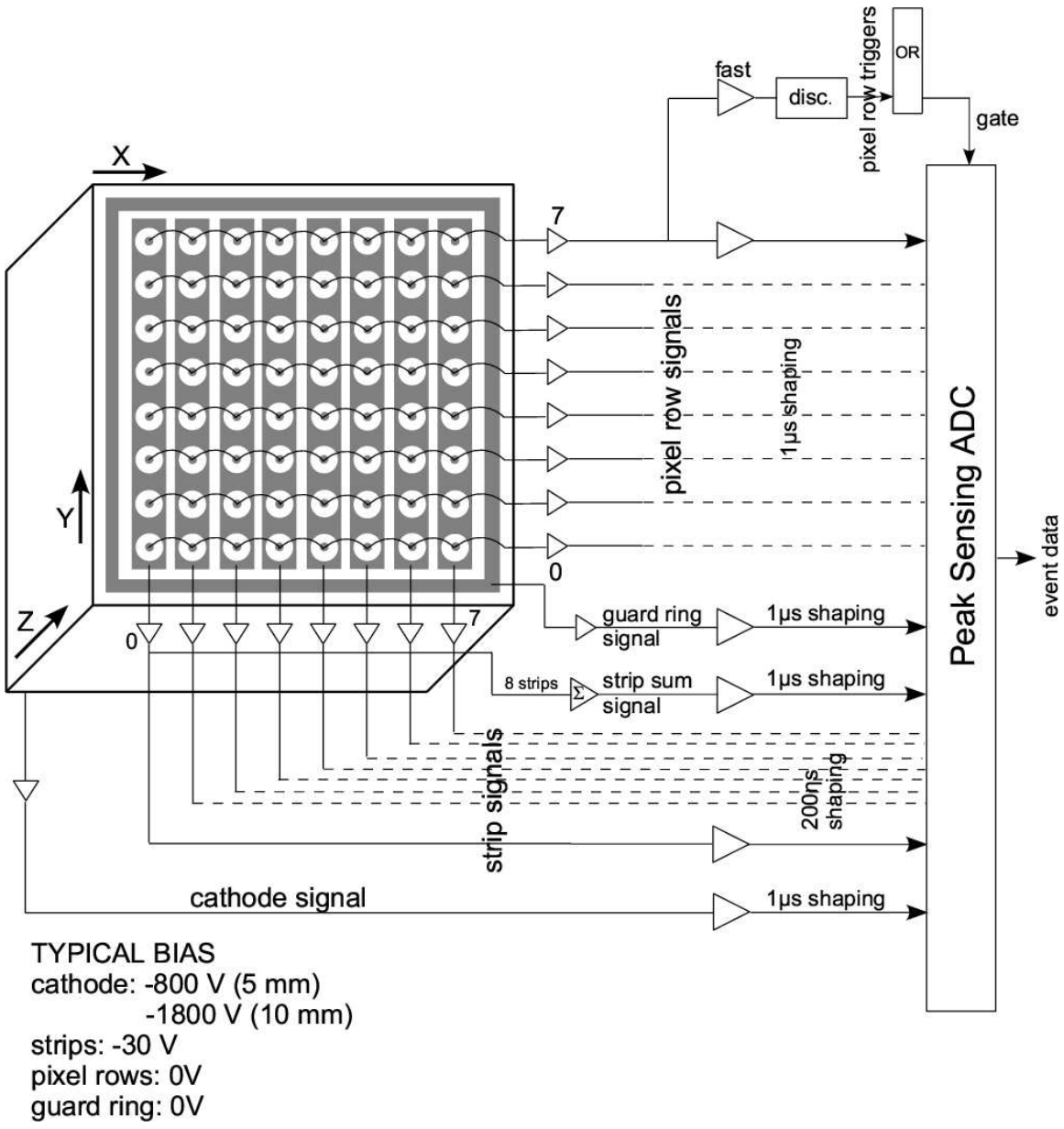

Figure 4-8: Experimental setup for orthogonal coplanar CZT strip detector design.

and Tcl-Tk. Data analysis software also uses a C program. Typical bias levels are also shown in this figure. The detectors were inserted into a custom test board for bias and readout of the charge signals with discrete preamplifiers (eV-5093). A strip sum signal is formed from the eight strip preamplifier outputs using a custom summing amplifier on the circuit board. The eight pixel row, eight strip column, cathode, guard ring and strip sum signals were taken off the socket and AC coupled to their respective charge sensitive preamplifier. The preamplifier output signals from each pixel and strip were routed to their own NIM spectroscopy amplifier. This amplifier produces shaped output for each pixel and strip. It also produces a fast signal for timing. The shaped signals were sent to their respective ADC for conversion. The cathode, guard ring and strip sum had a separate spectroscopy amplifier. When any one of the pixel row fast output signal was greater than its discriminator threshold, ADCs were triggered and all the signal outputs were recorded.

Pixel row signals are used for event triggering because of their better signal to noise ratio and relatively small dependence on the depth of interaction, z. These signals are also used to determine the y coordinate of the photon interaction location and the energy of the photon. The guard ring is also biased and its signals processed like pixels to maintain uniform electric field and to identify events occurring outside the imaging region of the detector.

4.3.2 Single-Sided Charge-Sharing CZT Strip Detector

Figure 4-9 shows the signal processing for single-sided charge sharing CZT strip detectors. This arrangement uses electronics similar to the other design. Although the row and column signals are shown here as the event trigger, in much of the study the cathode signal was used to trigger the data acquisition system. Typical bias levels are -1100 V for the cathode, -30 V for z-grid and 0V for guard, row and column contacts.

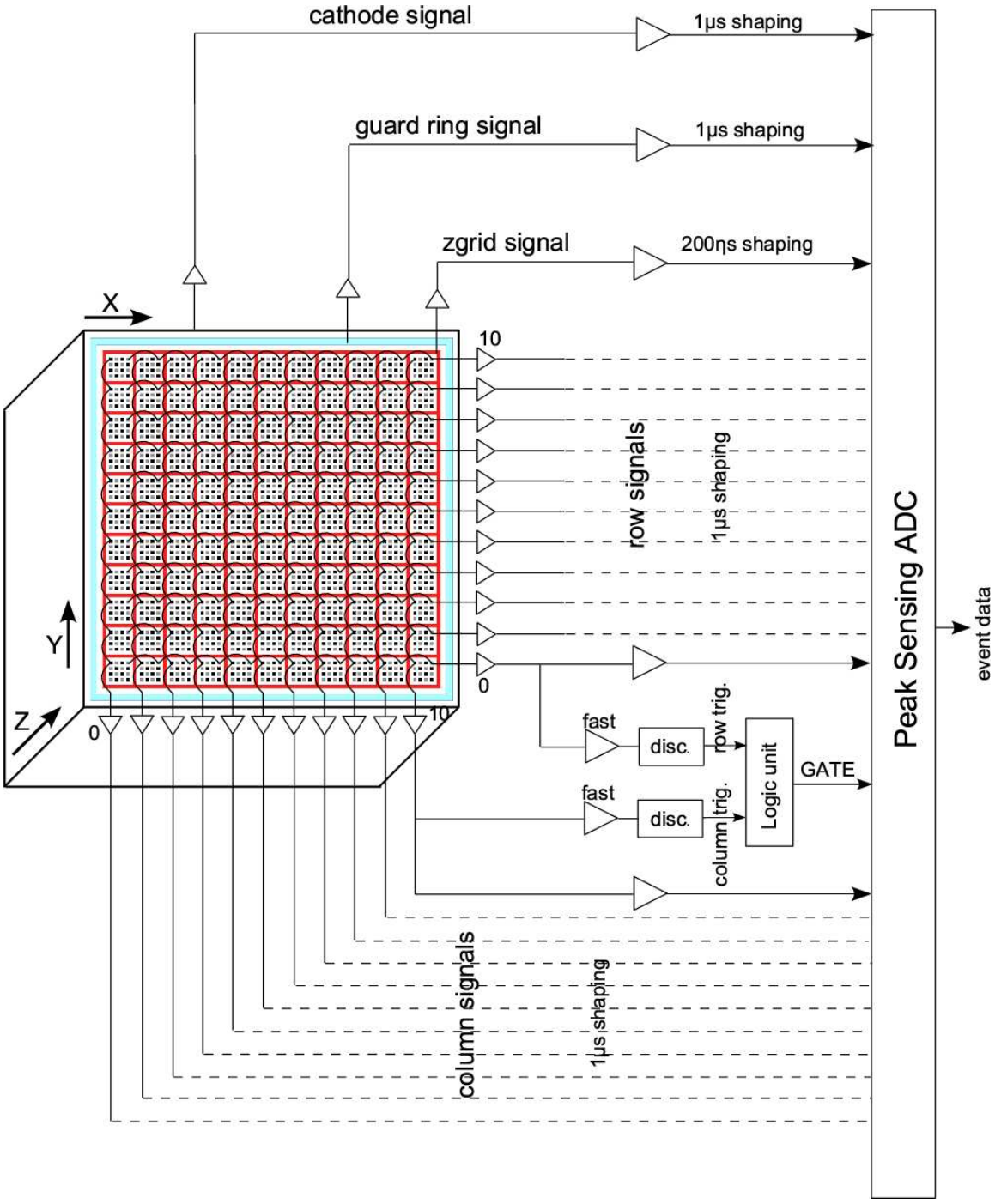

Figure 4-9: Experimental setup for single-sided charge-sharing CZT strip detector design.

Similar to the previous design, the detectors were inserted into a custom test board for bias and readout of the charge signals with discrete preamplifiers (eV-5093). The eleven row, eleven column, cathode, guard and z-grid signals were taken off the socket and AC coupled to their respective charge sensitive preamplifier. The preamplifier output signals from each row and column were connected to their own NIM spectroscopy amplifier. This amplifier produces shaped output for each row and column and it also produces a fast signal for timing. The shaped signals were sent to their respective ADC for conversion. The cathode, guard and z-grid had a separate spectroscopy amplifier. When any one of the row or column fast output signal was greater than its discriminator threshold, ADCs were triggered and all the signal outputs were recorded.

4.4 Experimental Results

In the following sections, the characterization results including energy resolution, spatial resolution, uniformity and efficiency for 5 mm thick detectors will be discussed. The detectors used for these sections are UNH-EV-3, UNH-EV-4, UNH-Y-2, UNH-Y-5, UNH-EV-14, UNH-EV-SUB02 and UNH-EV-SUB04. Properties of detector prototypes can be seen in Table 4.1.

4.4.1 Spectroscopy: Orthogonal Coplanar CZT Strip Detectors

To perform the spectroscopy measurements, the detectors were flood illuminated from the cathode side with photons from various radioactive $\gamma-$ray sources spanning energy range from 60 to 662 keV. Figure 4-10 shows the spectroscopic performance of a pixel row of the 5 mm thick orthogonal coplanar CZT strip detector design. The measured energy resolutions (Full Width at Half Maximum) at room temperature are shown in Table 4.2. The electronic noise measured with the test pulse is 4.9 keV. The depth dependence of energy

Table 4.1: Properties of detector prototypes.

Detector Type	**Detector ID**	**Size (mm^3)**	**Manufacturer**	**Assembly Date**
Orthogonal-Coplanar CZT Strip Detector	UNH-EV-3	$10 \times 10 \times 5$	eV Products	Jun. 99
	UNH-EV-4	$10 \times 10 \times 5$	eV Products	Jun. 99
	UNH-Y-2	$10 \times 10 \times 10$	Yinnel Tech.	Dec. 01
	UNH-Y-5	$10 \times 10 \times 5$	Yinnel Tech.	Dec. 01
	UNH-EV-14	$10 \times 10 \times 5$	eV Products	Jun. 04
Single-Sided Charge-Sharing CZT Strip Detector	UNH-EV-SUB02	$15 \times 15 \times 7.5$	eV Products	Sep. 04
	UNH-EV-SUB04	$15 \times 15 \times 7.5$	eV Products	Sep. 04

Table 4.2: Energy resolution of single pixel row spectra of 5 mm thick orthogonal-coplanar CZT strip detector (UNH-EV-14) energy range from 60 to 662 keV.

Source	**Energy (keV)**	**FWHM (keV)**
^{241}Am	60	5.2
^{133}Ba	81	5.9
^{57}Co	122	6.3
^{133}Ba	356	6.6
^{137}Cs	662	8.7

for several radioactive sources can be seen in Figure 4-11 which indicates that energy is almost independent of the depth of interaction. Therefore, we did not apply any correction to the spectra. Measured energy resolution (FWHM) by He et al. (1999) for 10 mm thick pixellated CZT detectors is 6.7 and 11.3 keV at 60 and 662 keV respectively. Similarly, Quadrini et al. (2005) measured 11.5 keV (FWHM) energy resolution at 122 keV with 5 mm thick pixel detectors. Moss et al. (2001) reported 18.5 and 32.0 keV energy resolution at 662 and 1333 keV, respectively for a 7.5 mm thick pixel detectors. Most of our results are better than these studies, even though we are using strip detectors and we do not have any correction applied to the spectra.

A problem encountered with the orthogonal coplanar design (see sec. 4.4.6) is charge

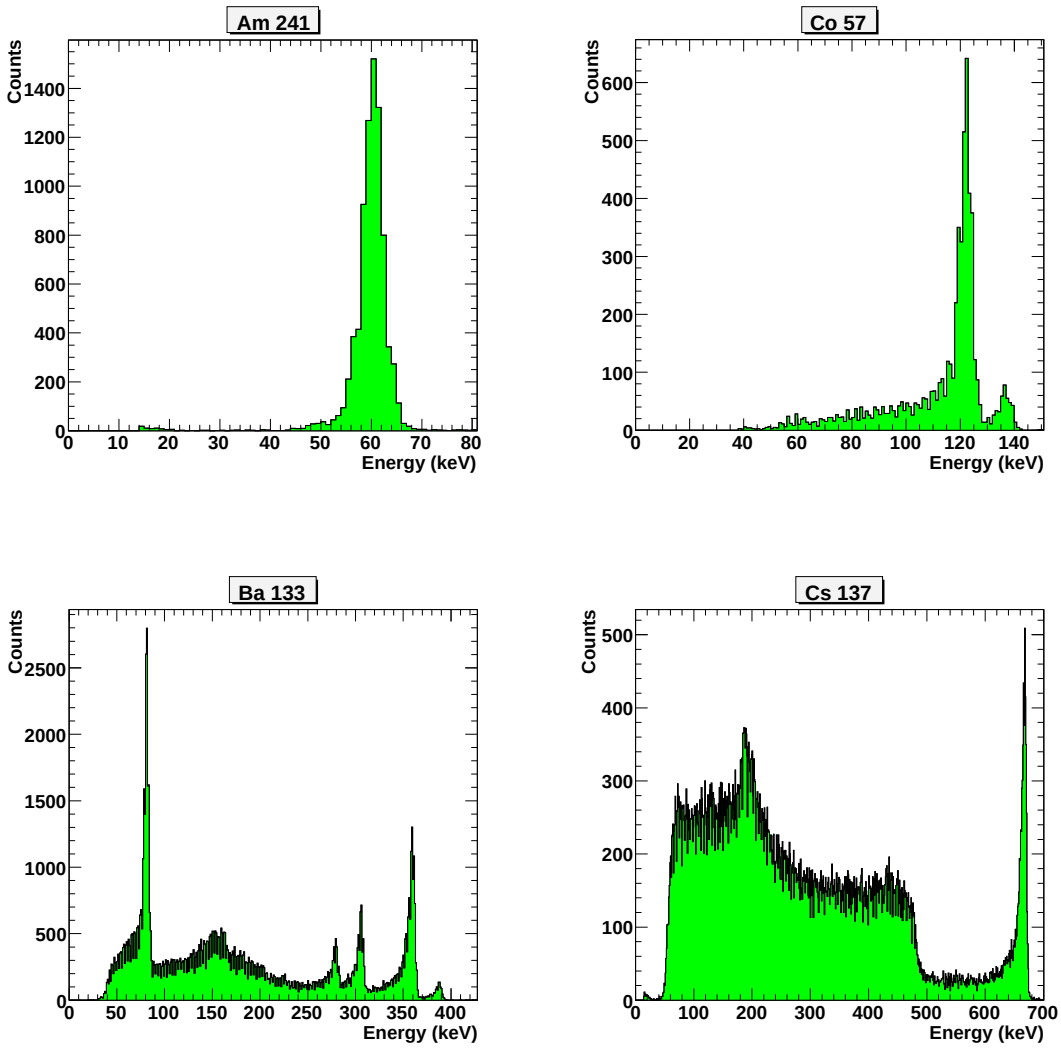

Figure 4-10: Spectroscopic performance of a pixel row spectra (8 pixel) of orthogonal coplanar CZT strip detector (UNH-EV-14). No event selections.

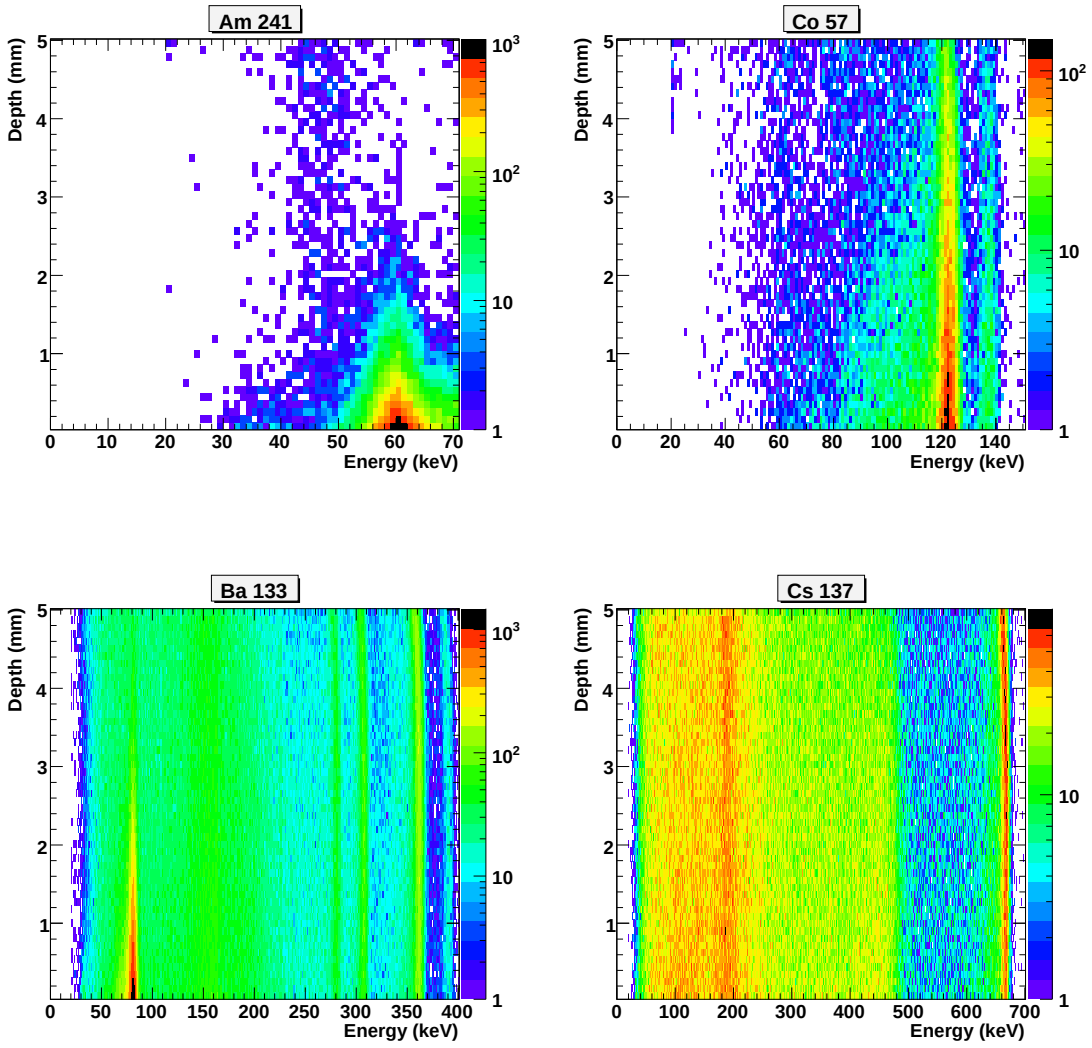

Figure 4-11: Depth dependence vs. energy of orthogonal coplanar CZT strip detector (UNH-EV-14) for all pixels. Cathode is at $z = 0$ and anode is at $z = 5$.

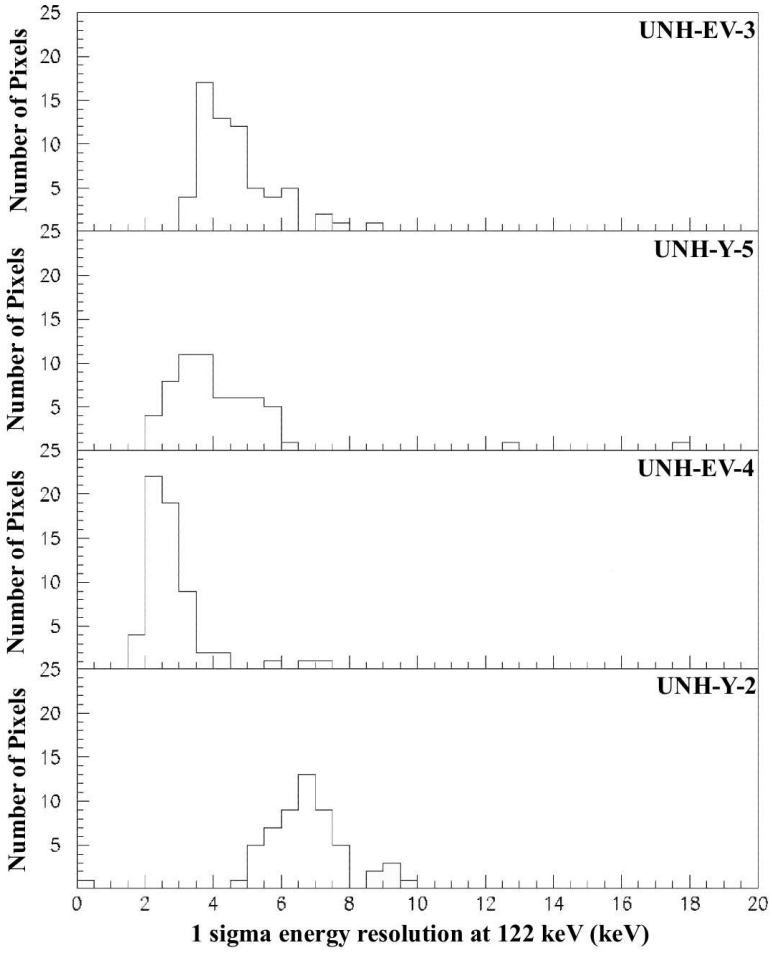

Figure 4-12: Energy resolution distribution at 122 keV for 64 pixels of four different orthogonal coplanar CZT strip detectors.

collection by the strip columns. This reduces the level of the pixel row trigger signal and causes errors in energy measurement for these events. Non-uniformity of the detector material or surface contacts further complicates the problem. This problem is illustrated with one of the prototype detectors (UNH-EV-3). The sample spectrum comparing a problematic region with a good region can be seen in Figure 4-26.

The $1-\sigma$ energy resolution distribution of each pixel for UNH-EV-3 is shown in Figure 4-12. Other plots in this figure show the energy distribution from other 5 mm thick detectors and one 10 mm thick detector (UNH-Y-2). Only 56 pixels are shown for UNH-Y-2 detector

Table 4.3: Energy resolution of a unit cell of 7.5 mm thick single-sided charge-sharing CZT strip detector (UNH-EV-SUB04) energy range from 60 to 1333 keV.

Source	**Energy (keV)**	**FWHM (keV)**
^{241}Am	60	10.1
^{133}Ba	81	7.7
^{57}Co	122	9.5
^{133}Ba	356	12.9
^{137}Cs	662	20.1
^{60}Co	1173	33.8
^{60}Co	1333	30.4

due to the noise in the one of the pixel row channel. There was no energy correction applied in preparing these histograms.

Figure 4-13 shows the response to photons from a ^{57}Co source measured with the 5 mm thick detector (UNH-EV-3). Event location is determined for each event by identifying the maximum pixel and maximum strip signal registered. 122 and 136 keV photopeaks are clearly seen at most pixels.

4.4.2 Spectroscopy: Single-Sided Charge-Sharing CZT Strip Detectors

Figure 4-14 shows the spectroscopic performance of a unit cell of a 7.5 mm thick single-sided charge-sharing CZT strip detector (UNH-EV-SUB04). These single pixel spectra were constructed from the addition of the maximum row and maximum column pulse heights (here we selected the central "pixel", row 5 column 5, i.e. X5 and Y5). The cathode signal was used to trigger the data acquisition system. The photopeaks are symmetric with no significant low energy tailing that would indicate a loss of signal to the non-collecting areas of the anode surface. Table 4.3 shows the energy resolution measured with this detector. The electronic noise is 5.7 keV (FWHM) per channel, or 8.0 keV (FWHM) for the combined row and column signals. We note that the summed spectra have broader peaks

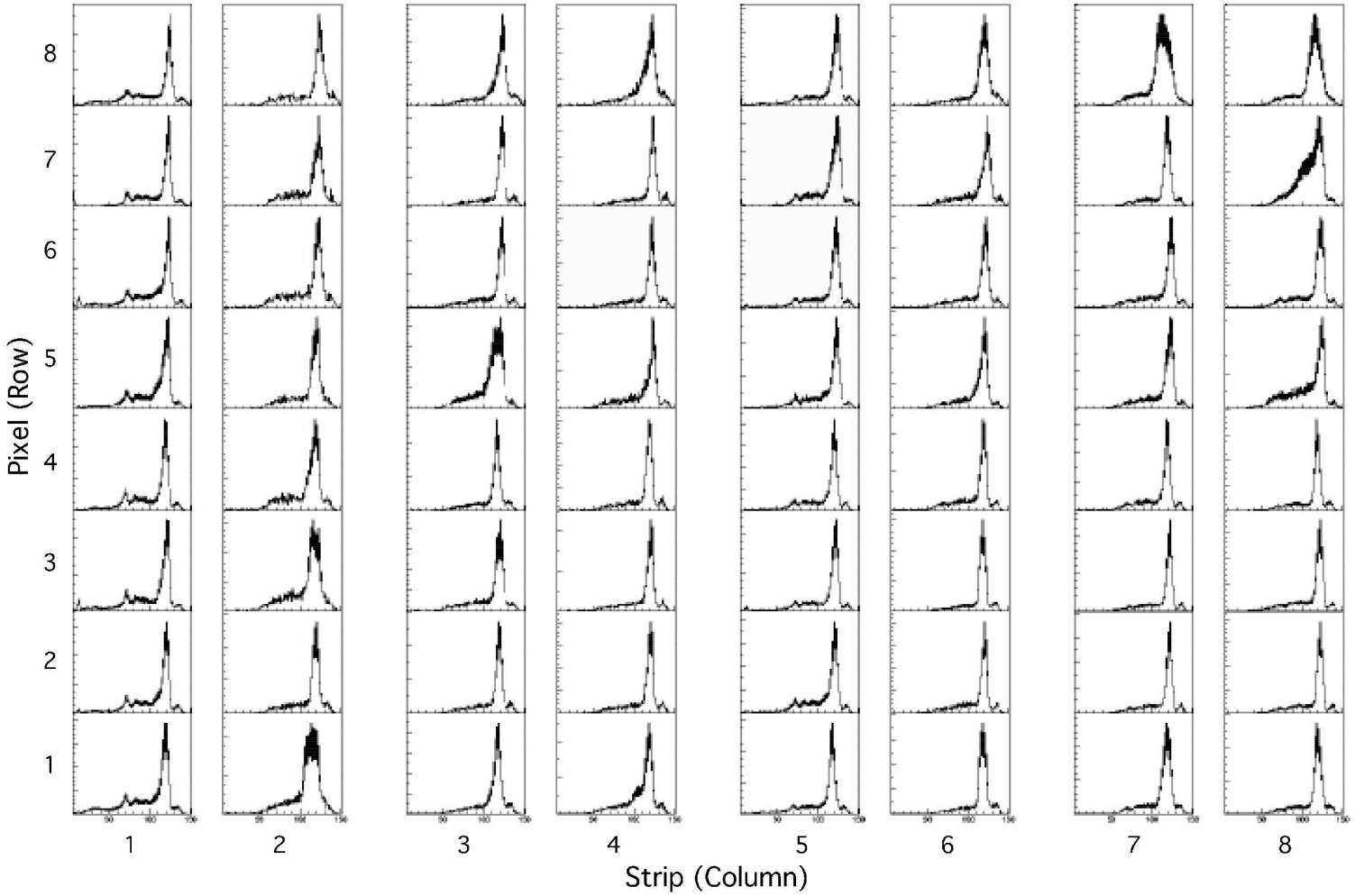

Figure 4-13: Spectral uniformity of 5mm thick orthogonal coplanar CZT strip detector (UNH-EV-3). Energy range is from 0 to 150 keV. ^{57}Co photopeaks, 122 and 136 keV, can be clearly seen at most pixels.

than measured with the orthogonal coplanar CZT strip detector. This is partly due to the addition in quadrature of the noise component of the row and column signals. Spectroscopic performance, however, is similar to that reported for pixel detectors.

An important advantage of this design is the simplicity of the front-end electronics. Polarities and shaping times are the same for both row and column channels. Since row and column electrodes are identically biased, surface leakage between them vanishes. Also, simulations of this design indicated that the large area covered by the grid electrode would result in better depth determination capability than was available from the individual strip column electrodes in our earlier orthogonal coplanar strip detector design.

There are some disadvantages with this design. To measure energy, column and row signals must be added. This degrades the achievable energy resolution by a factor related to the electronic noise. Capacitance effects due to the contact pad and interconnect structure also increase the noise. However, selecting the proper ASIC may minimize this effect.

Figure 4-15(a) and 4-15(b) shows the depth dependence of energy and a unit cell spectrum with ^{137}Cs. It can be seen that for photopeak events closer to the anode surface, the signal is decreases. This is due to the trapped holes near the anode surface (Shor et al., 1999). We applied the following empirical formula that is also used by Shor et al. (1999) to correct the events closer to the anode surface.

$$E_{corr} = \frac{E}{1 - C_1 \times \exp(-C_2/z)} \tag{4.1}$$

where E is the energy of the photon before the correction, z is the depth of interaction that is calculated from cathode to maximum anode signal ratio (see 4.4.3), C_1 and C_2 are two constants found by fitting the photopeak in Figure 4-15(a). The result of depth correction can be seen in Figure 4-15(c) and 4-15(d). The energy resolution is also improved by $\sim$1%.

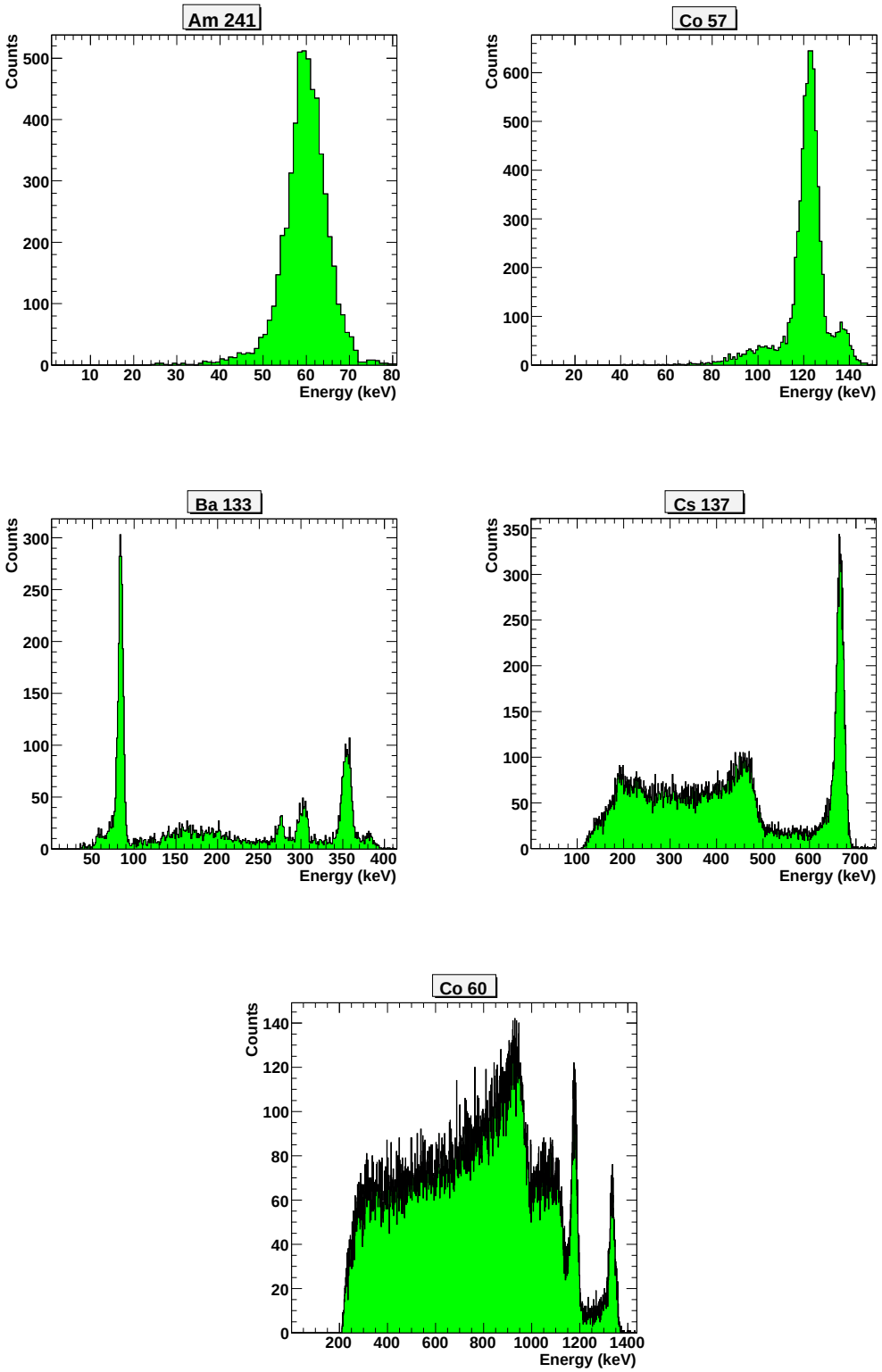

Figure 4-14: Spectroscopic performance of a unit cell of a 7.5 mm thick single-sided charge-sharing CZT strip detector (UNH-EV-SUB04).

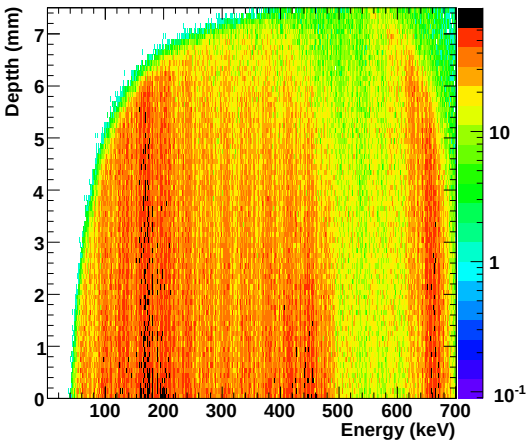

(a) Depth dependence of energy before correction.

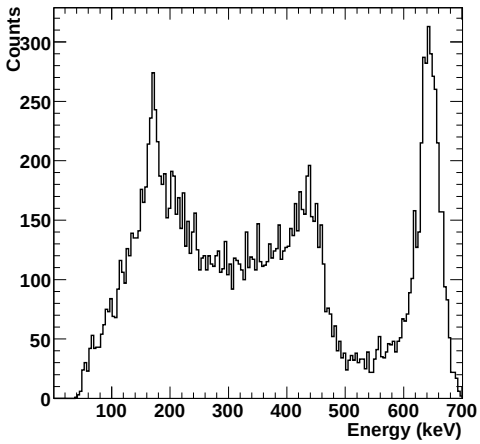

(b) Spectroscopic performance of a unit cell before depth correction.

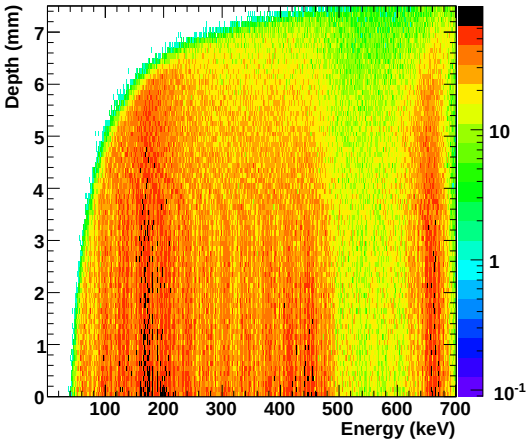

(c) Depth dependence of energy after correction.

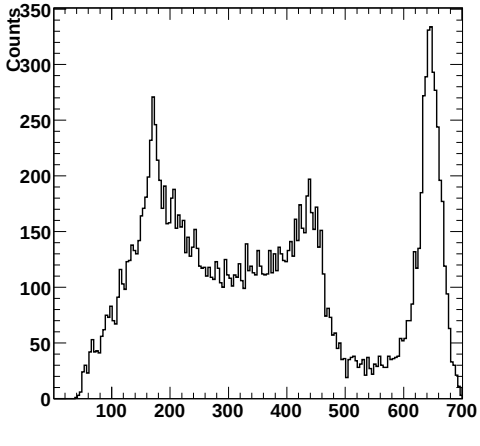

(d) Spectroscopic performance of a unit cell after depth correction.

Figure 4-15: Depth correction for single-sided charge-sharing CZT strip detector(UNH-EV-SUB04).

4.4.3 Imaging: Orthogonal Coplanar CZT Strip Detectors

The imaging capability of one of the detectors was studied using a ^{57}Co source and a tungsten collimator with a 0.2 mm diameter beam spot. Figure 4-16 shows the locations of photon interactions along a collimated beam of 122 keV photons incident at $\sim 25^{\circ}$ from the z-axis. The beam enters near strip 3, pixel 1 and crosses several strip columns and pixel rows as it passes through the 5 mm thick detector. The discontinuity in the y dimension indicates that there is little charge sharing between pixel rows.

Depth calibration was obtained by illuminating the detector from the side using 122 keV photons from a ^{57}Co source. A 0.4 mm wide slit in a tungsten block was used as a collimator. This collimator was used at seven known depths. Two different methods were used to find the depth of interaction. The first method involves the use of the cathode to maximum pixel row signal ratio. The following formula is used for the depth calculation

$$z = T \times \left[1 - B\left(\frac{C}{A}\right)\right] \tag{4.2}$$

where T is the detector thickness, B is a constant to match the gain of cathode and the maximum pixel signal, C is the cathode and A is the maximum pixel row signal. The measured $1-\sigma$ average spatial resolution at 122 keV across the full range of depth is 0.37 mm. The strip sum signal is also used to determine the depth of interaction. In this method, the measured $1-\sigma$ average spatial resolution is 0.86 mm. The poorer result obtained using the strip sum method is the result of adding the noise of strip signals.

To check the consistency of depth calibration, the attenuation length for 122 keV photons is measured. The entire cathode surface is illuminated at normal incidence using a ^{57}Co source. The measured distribution of interaction depths is shown in Figure 4-17. The measured value is 2.00 ± 0.16 mm agrees with the theoretical value of 2.01 mm.

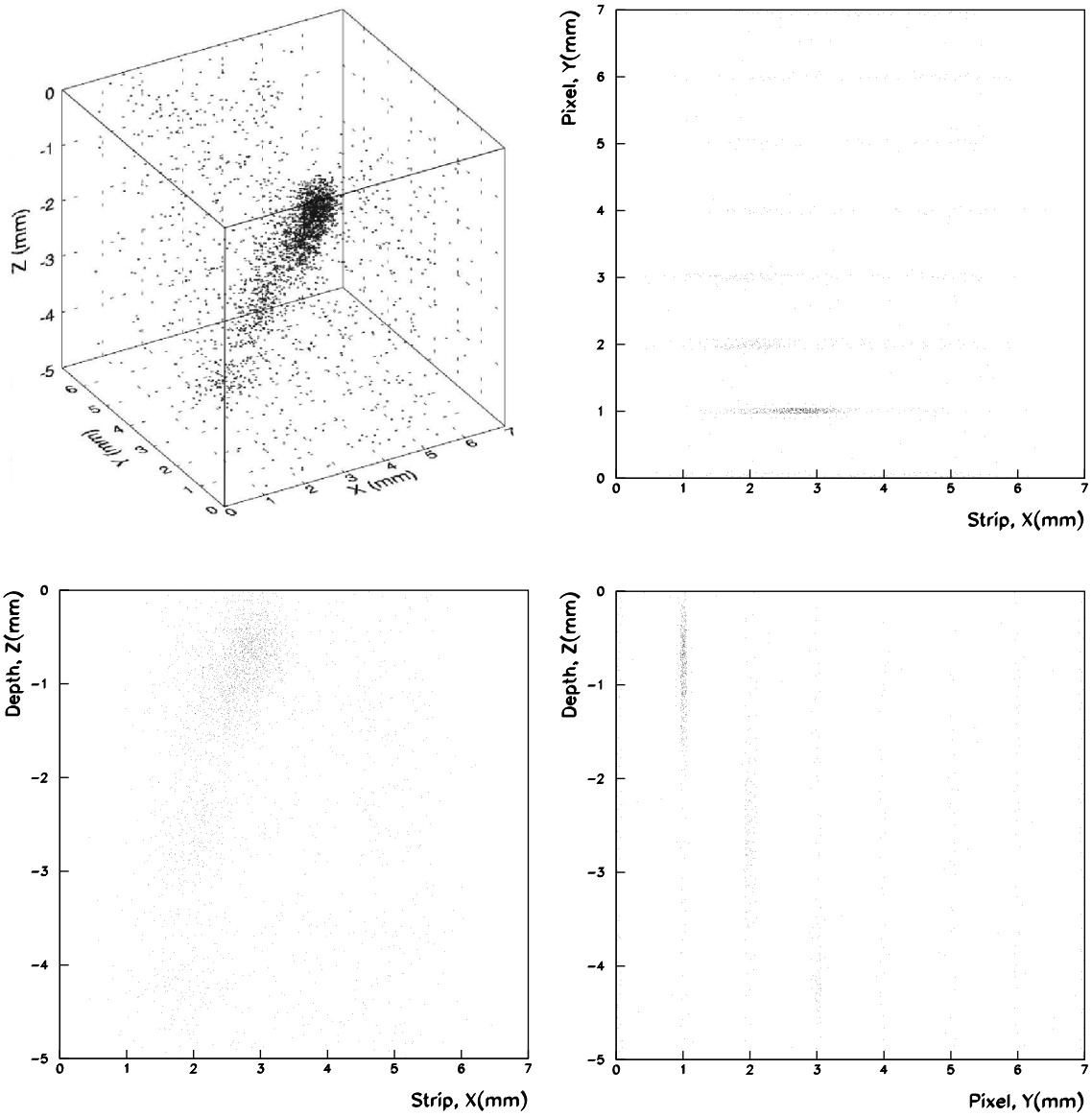

Figure 4-16: 3-D event locations and projections on x-y, x-z and y-z plane using UNH-EV-3. Cathode signal is used for depth measurement. Cathode is at z=0, sign of z was inverted to facilitate the illustration.

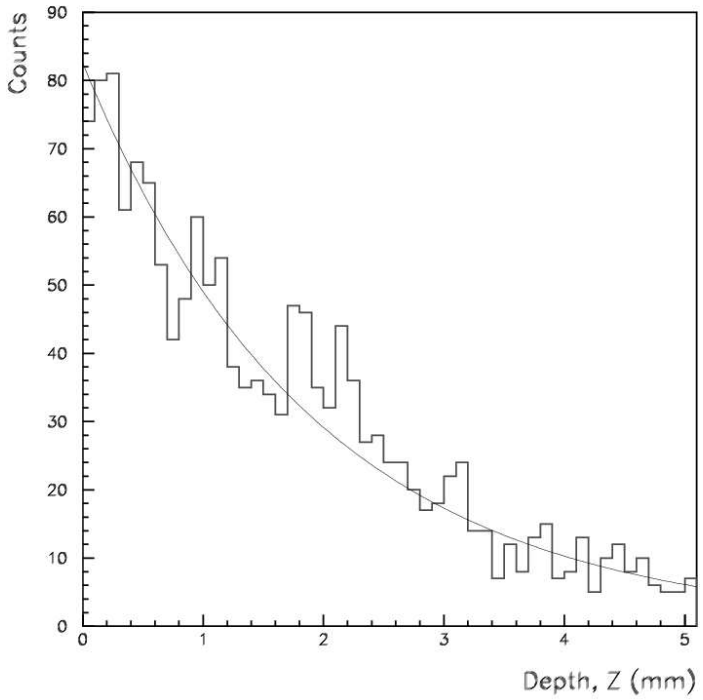

Figure 4-17: Measurement of the attenuation length for 122 keV photons in orthogonal coplanar CZT strip detector (UNH-EV-3).

4.4.4 Imaging: Single-Sided Charge-Sharing CZT Strip Detectors

Similar 3-D imaging and attenuation length calculation for 122 keV photons is done for single-sided charge-sharing CZT strip detectors. In this case, we used a 500μm beam spot incident on the cathode surface at $\sim 20^{\circ}$ from the z-axis (Figure 4-18). Rows and columns on the anode surface are used to trigger the data acquisition system. Photons in this beam cross several rows and columns as they pass through the detector. Spatial resolution is better than the unit cell pitch, 1.225 mm, in the x and y dimensions. Spatial resolution (1σ) in the z dimension, using the cathode signal, is 0.98 mm (Figure 4-19(a)). We can also see depth of interaction in Figure 4-19(b). Measured attenuation length is 2.00 ± 0.01 mm, agrees with the theoretical value.

Like the strip signals on orthogonal coplanar strip detector design, the noncollecting

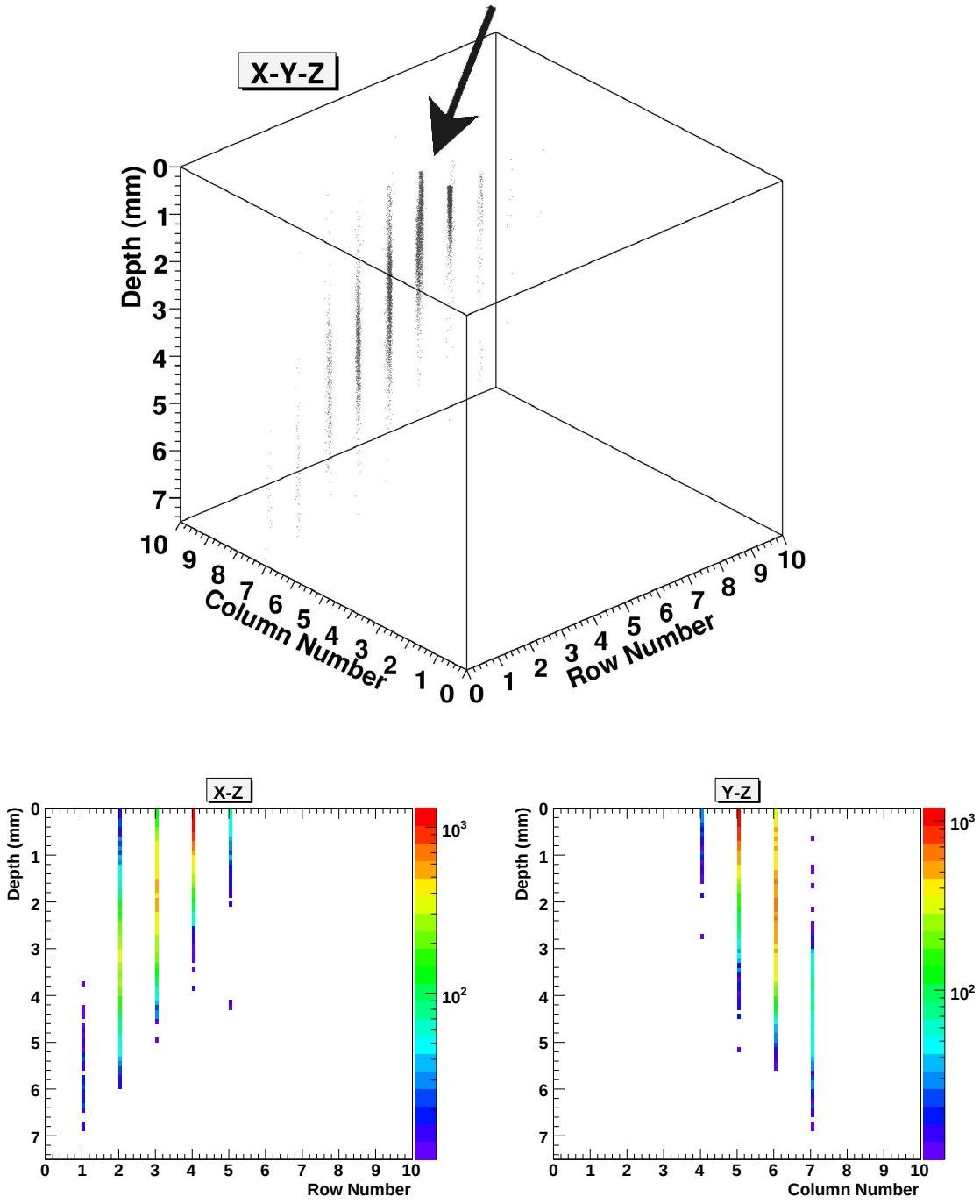

Figure 4-18: 3-D event locations and projections on x-z and y-z plane using UNH-EV-SUB04. Cathode signal is used for depth measurement. Cathode is at z=0. Rows and column on the anode surface are used to trigger the data acquisition system.

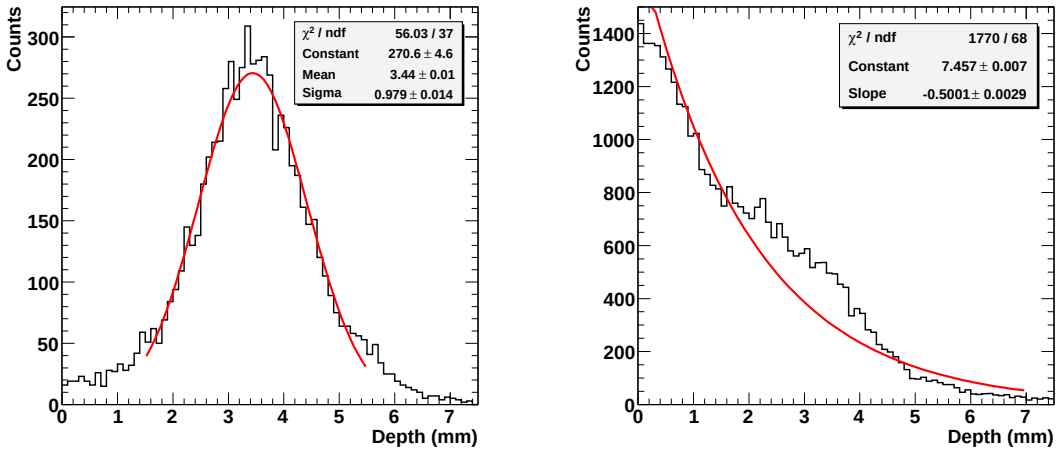

Figure 4-19: (a) Depth resolution of single-sided charge-sharing CZT strip detector for 3-D imaging data. (b) Depth of interaction for the same data.

grid signal on single-sided charge-sharing strip detector can be used to determine the depth of interaction. Using the grid electrode signal to determine the depth of interaction instead of the cathode signal, the spatial resolution (1σ) measured is about a factor of three poorer. This is due to the large surface leakage associated with zgrid electrode.

The depth measurement for the single-sided charge-sharing CZT strip detector is also done by using the ratio of the cathode-to-maximum anode signal ratio. The maximum anode signal is the addition of maximum row and maximum column signals event by event. A similar equation, equation (4.2), is used for depth measurement. In this case, A is the addition of maximum row and maximum column signals. Figure 4-20(a) shows the measured distribution of interaction depths (z) for 122 keV photons from a ^{57}Co source illuminating the entire cathode surface at normal incidence. The calculated attenuation length in this measurement is 2.03 ± 0.01 mm. The simulated depth of interaction using 122 keV photons can be seen in Figure 4-20(b). The calculated attenuation length is 2.02 ± 0.03 mm agrees with the theoretical and measured value. This result also validates the physics of our simulation tools.

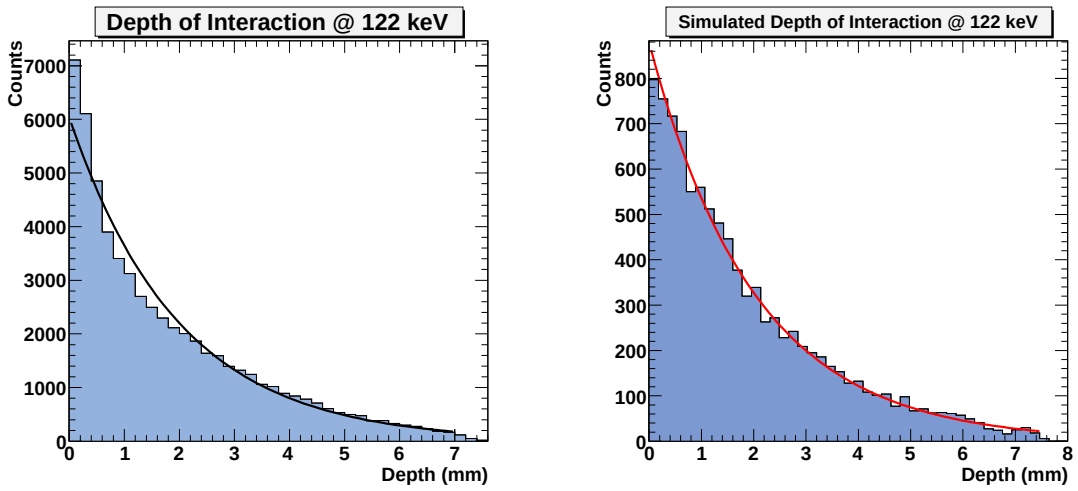

(a) (b)

Figure 4-20: Measurement of the attenuation length for 122 keV photons in single-sided charge-sharing CZT strip detector (UNH-EV-SUB04) (left). Simulation of the attenuation length for 122 keV photons using GEANT4 (right).

4.4.5 Imaging Efficiency for Single-Sided Charge-Sharing CZT Strip Detectors

The limited charge sharing due to the small size of the electron cloud results for some events a measurement of only the x or y coordinate, not both, and, at least for the first prototype detectors, reduce the detection efficiency for imaging measurements. This means that, charge sharing between rows and columns is important in determining the imaging efficiency for this design (Dönmez et al., 2005). Both row and column signals must exceed the noise threshold to achieve measures of both the x and y locations. To measure the fraction of events registering a sufficient signal in both row and column channels, we made a run with a collimated ^{57}Co source. Figure 4-21 shows the computed event location for a 1 mm diameter beam of ^{57}Co photons. The computed image of all photopeak events (122 keV) is shown on the left (Figure 4-21(a)). The image on the right (Figure 4-21(b)) is formed from events whose row and column pulse heights both exceeded the 8 keV threshold.

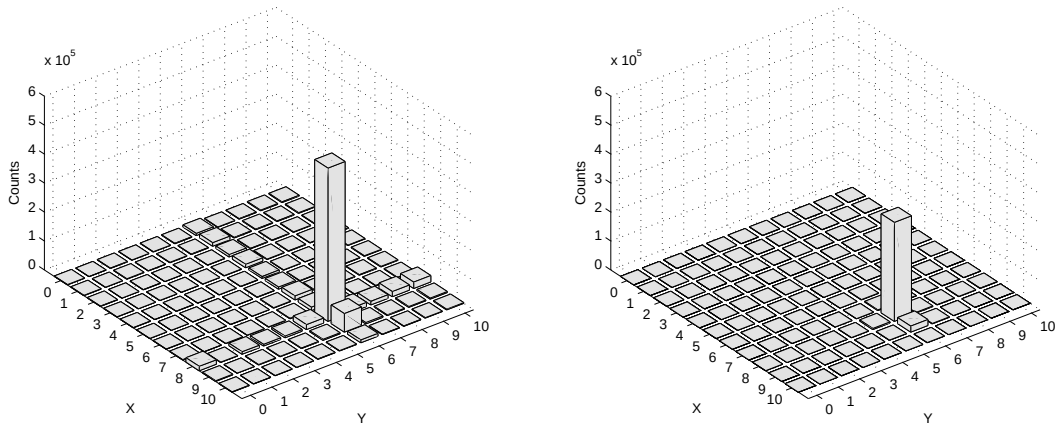

(a) (b)

Figure 4-21: Computed event locations for collimated ^{57}Co beam spot. For all events (a); for events above sharing threshold (b).

Most (64%) of the events are above this threshold for both row and column. This fraction represents the efficiency for the imaging at this energy. Figure 4-22 shows scatter plots for each calibration source. For all energies, there is a significant number of events for which most or all of the charge is collected on one channel only (row or column). In an ideal charge-sharing detector, however, events on the scatter plot should accumulate near the center of the main diagonal with comparable signals in both x and y as indicated by the circle in Figure 4-23.

4.4.6 Uniformity: Orthogonal Coplanar CZT Strip Detectors

The uniformity of UNH-EV-3 was studied by scanning the entire cathode surface in 0.5 mm steps with collimated photons from a ^{57}Co source. Both a 1.0 mm diameter beam spot and a 1.0 mm wide slit collimator were used.

Figure 4-24 shows the event locations computed using the recorded pulse heights at four different 1.0 mm wide slit collimator locations. The y position is more quantized than the x position since there is little charge sharing between pixel rows. A relatively uniform image

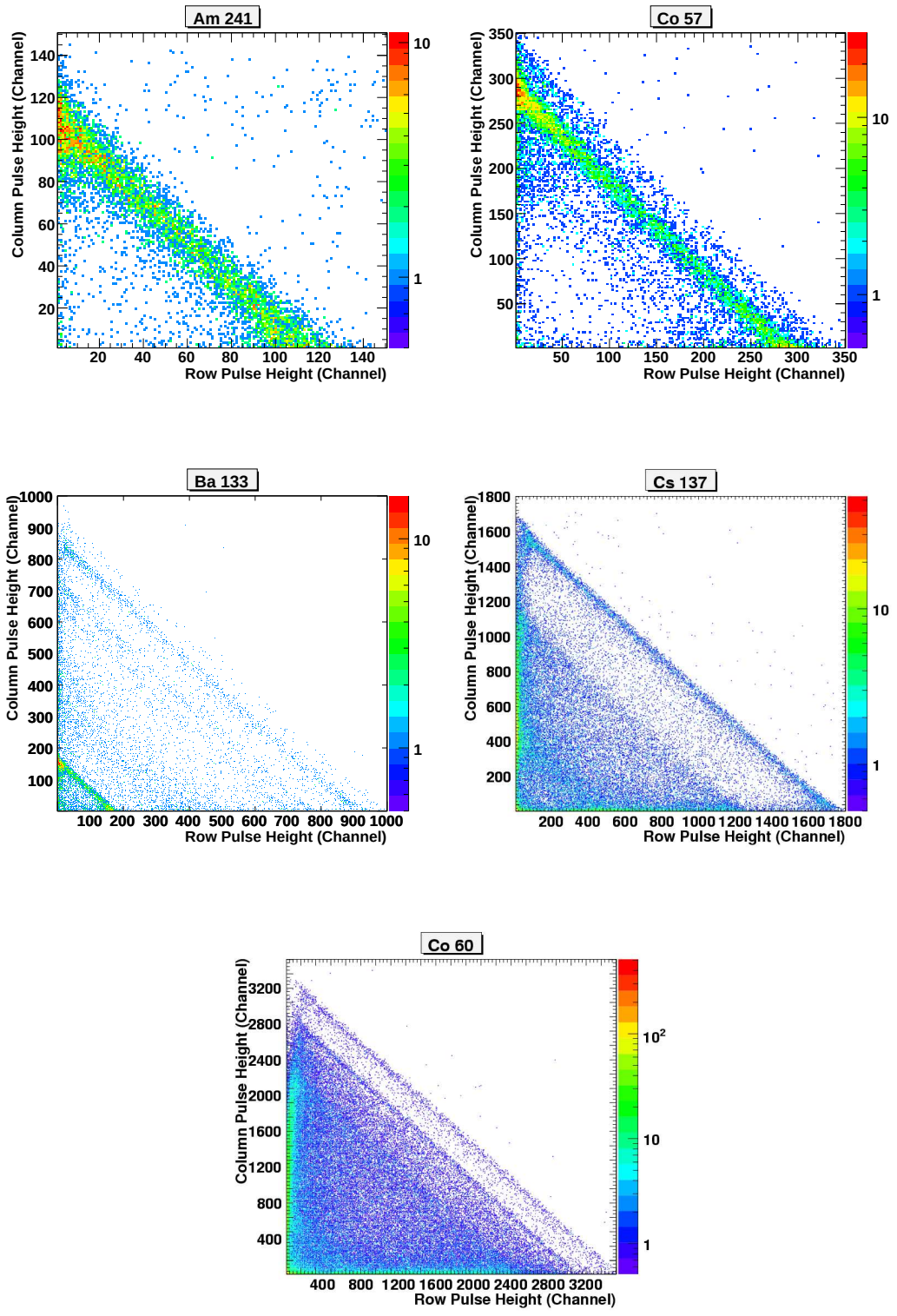

Figure 4-22: Scatter plots of a unit cell of single-sided charge-sharing CZT strip detector (UNH-EV-SUB04).

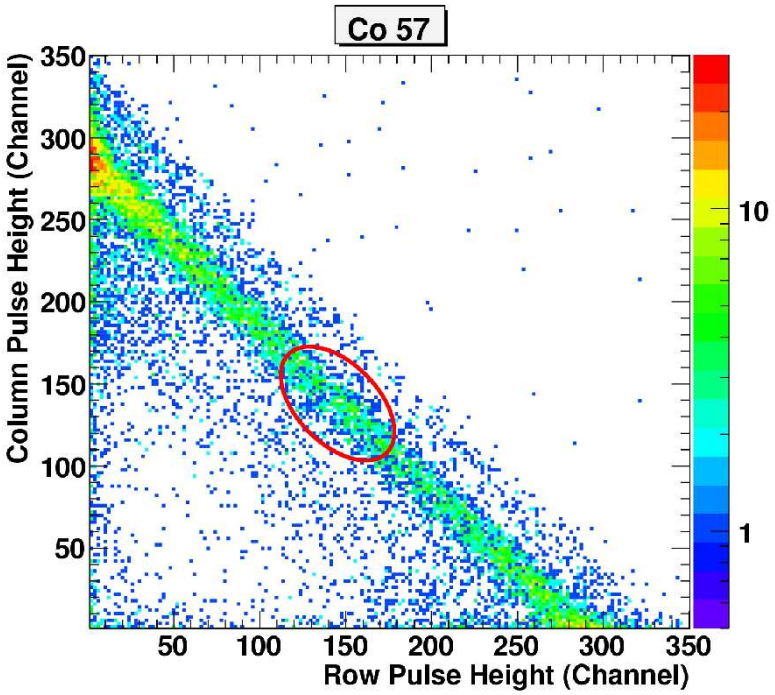

Figure 4-23: Expected charge sharing is indicated by a red circle for single-sided charge-sharing CZT strip detector.

response was obtained for most of the collimator locations (Figure 4-24(a) and 4-24(b)). The lower panels show a region of nonuniform image response. Figure 4-24(c) and 4-24(d) show one region, at pixel row 5, strip column 6, for which the event locations are in error by more than 1.0 mm.

We used the spot collimator to scan the imaging region for trigger uniformity of orthogonal coplanar CZT strip detector. A map of trigger rate for each unit cell is shown in left of Figure 4-25. The average trigger rate from the source is 65 s^{-1}. A dip in the trigger rate along the strip column 1 in this figure. The maximum trigger rate is 99 s^{-1} at strip column 3 and pixel row 4. To help identify the cause of this trigger nonuniformity, we made similar scan using the cathode signal to provide the trigger. In this case, we saw a much more uniform response (Figure 4-25, right). The average trigger rate was 81 s^{-1}. This trigger rate indicates that anode contact nonuniformity of the pixel row trigger channels are more likely sources of this nonuniformity than is the detector material.

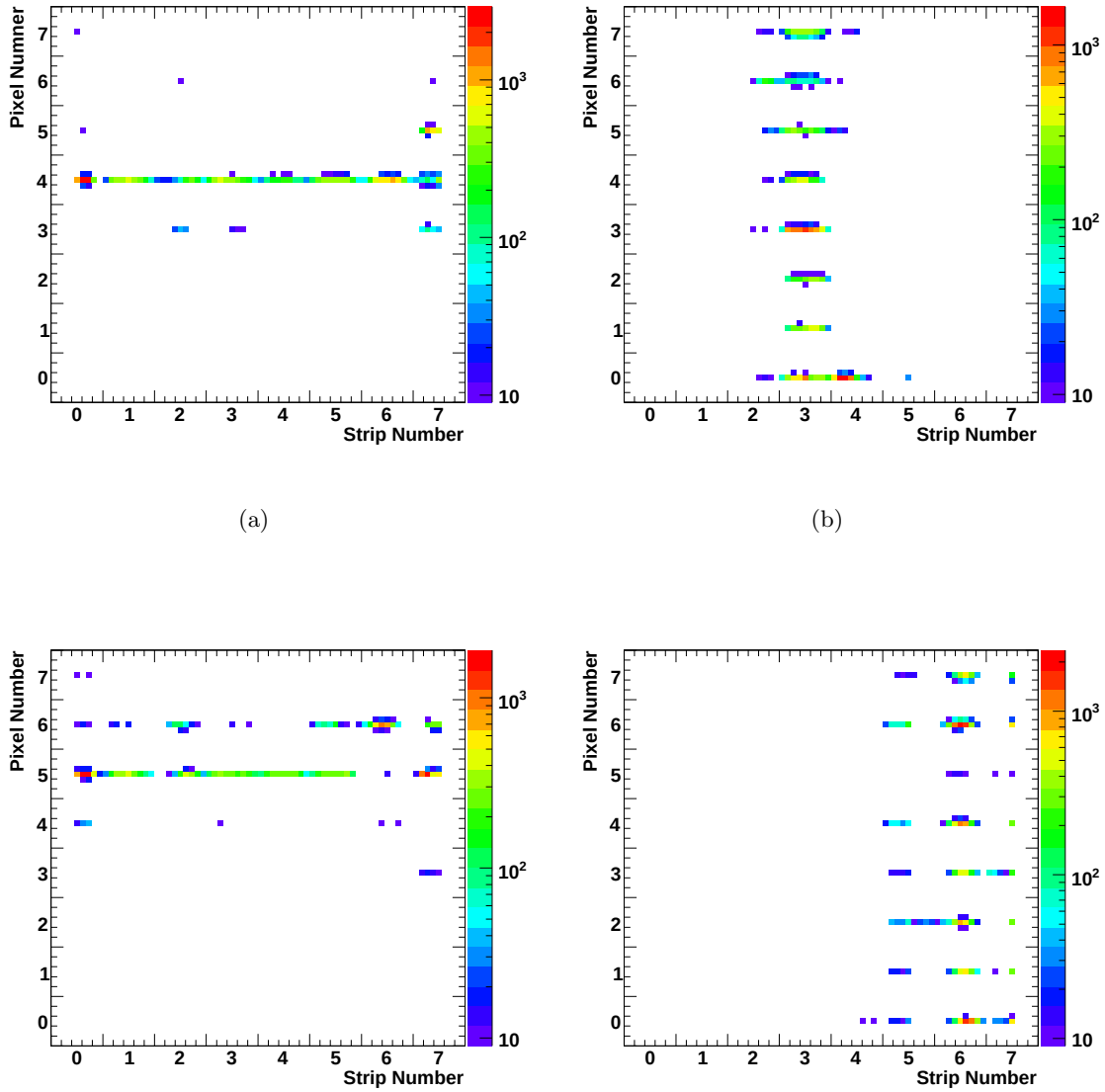

(a) (b)

(c) (d)

Figure 4-24: Reconstructed images at four different slit collimator locations. Figures on the upper panel shows relatively uniform image response. Figures on the lower panel shows relatively nonuniform image response. Rows and columns of prototype detectors are numbered 0 through 7.

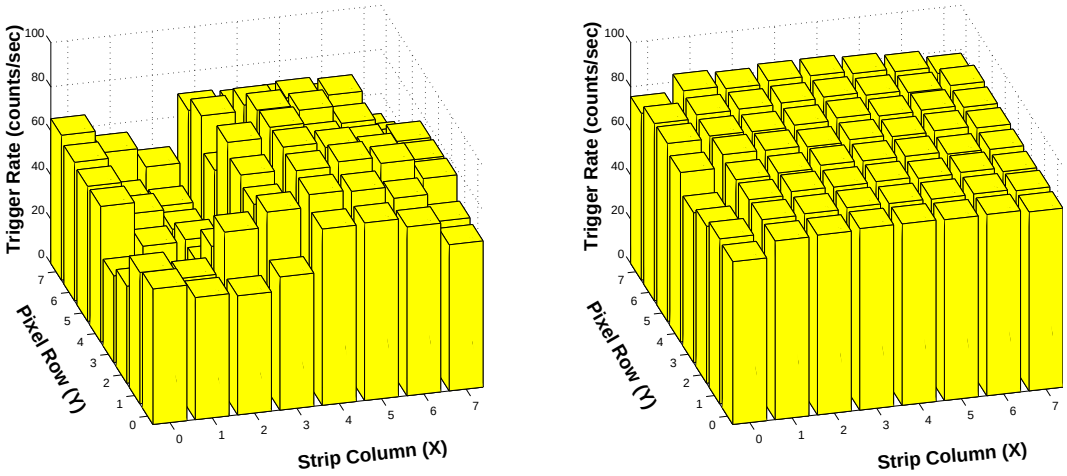

Figure 4-25: Trigger rate maps of 5 mm thick orthogonal coplanar CZT strip detector (UNH-EV-3) with a 1.0 mm diameter beam spot from collimated ^{57}Co source. Pixel row signal triggering the data acquisition system is shown in the left figure. Figure on the right shows the cathode signal triggering the data acquisition system.

We also performed spectroscopic analysis of the beam spot data to identify the source of the trigger nonuniformity with pixel row trigger. We looked at the spectroscopy of all unit cells to the find best and worst. The best spectral performance is seen on pixel row 4, strip column 3 (Figure 4-26(a)). This is also the location where the maximum trigger rate is observed. Figure 4-26(b) shows the worst spectrum which is at pixel row 6, strip column 1. To see the effect of strip column charge collection in these cases the strip column signals were processed using the same polarity and shaping times as the pixel rows. The scatter plots (Figure 4-26(c) and 4-26(d)) show that the low measurement in energy resolution is the result of charge collection on the "noncollecting" strip column electrode in this region. The interpretation of the charge collection is as follows. When we look at the scatter plot of a well behaving pixel (Figure 4-26(c)), we see that most of the events are at channel 300 (i.e. 122 keV) and there is an insignificant signal on the strip. This differs in Figure 4-26(d). In this case, it can be seen that the pixel pulse height decreases as the strip signal pulse height increases, which means some of the charge is collected by the strip reducing

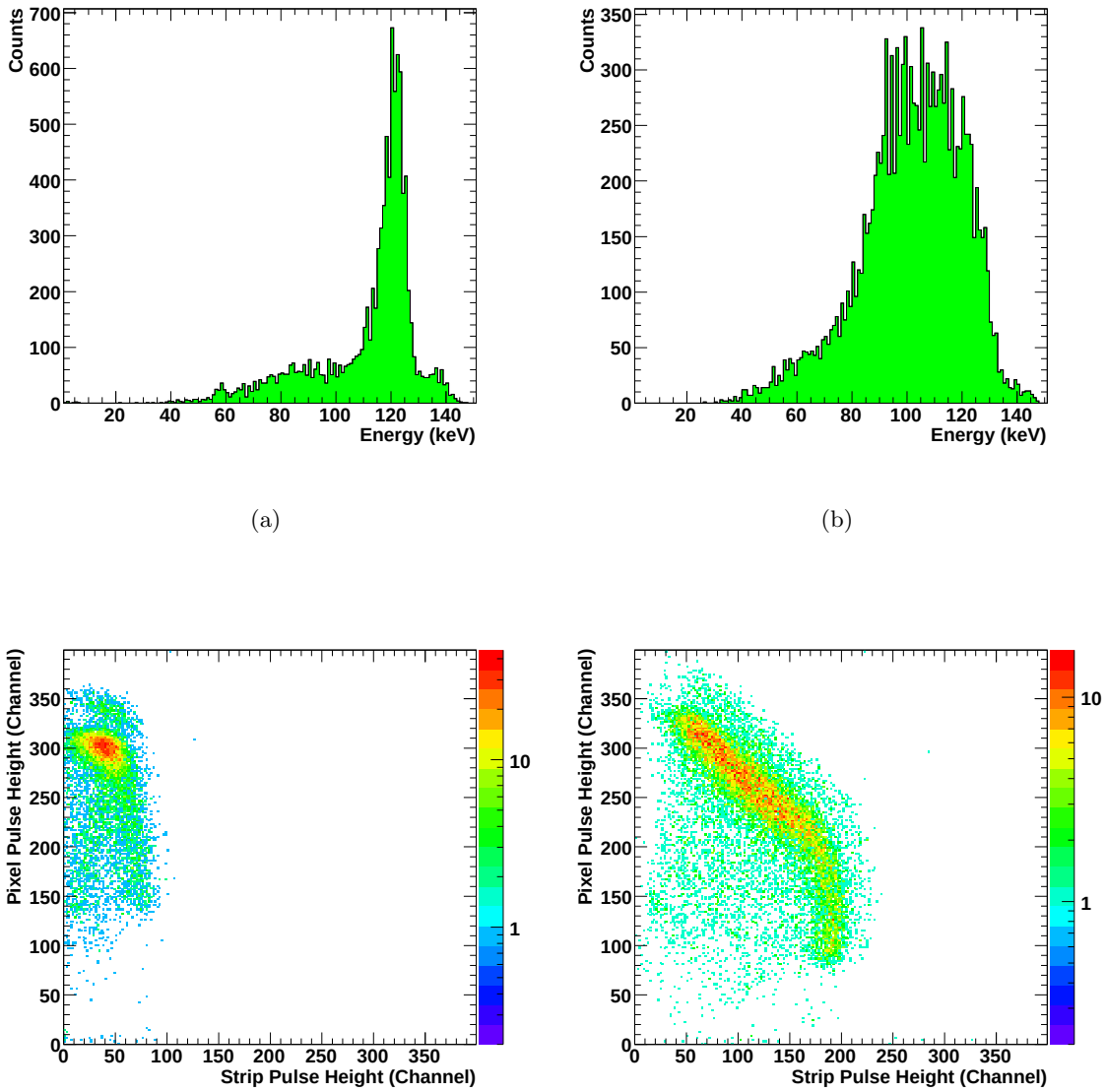

(a) (b)

(c) (d)

Figure 4-26: Spectra and scatter plots of strip vs. pixel pulse height for two collimator locations. Pixel row 4, strip column 3 (left) and pixel row 6, strip column 1 (right). Data taken with 5 mm thick orthogonal coplanar CZT strip detector (UNH-EV-3).

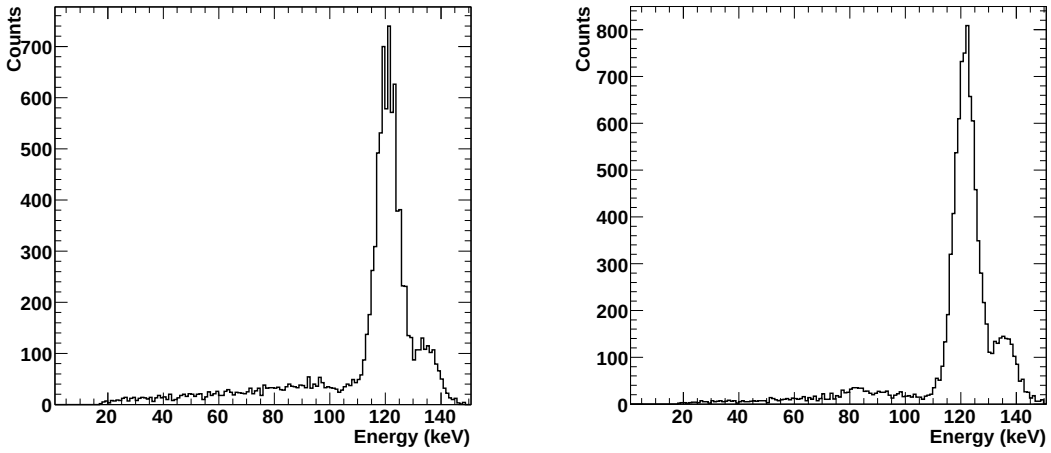

Figure 4-27: Different unit cell spectra from single-sided charge-sharing CZT strip detector (UNH-EV-SUB04). 500μm beam spot located at row 6 column 5 (left) and row 7 column 5 (right). The number of photopeak events is 7250 ± 350.

the signal collected by the pixel.

4.4.7 Uniformity: Single-Sided Charge-Sharing CZT Strip Detectors

Due to the noise on two row and one column, we couldn't repeat same uniformity measurements with single-sided charge-sharing CZT strip detector (UNH-EV-SUB04). Instead, we scanned some unit cells with 500μm beam spot collimator. Figure 4-27 shows spectra from two different unit cell, row 6 column 5 and row 7 column 5. The number of photopeak events is 7250 ± 350. Figure 4-28 shows spectra where collimator located between row 6 column 5 and row 7 column 5. Energy spectra of these unit cell can be seen in Figure 4-28(a) and 4-28(b). We can also see added spectrum of these unit cell in this figure (Figure 4-28(c). It can be seen that spectroscopic performance is greatly increased. But the number of photopeak events is not preserved which is only $\sim 40\%$ of the previous result.

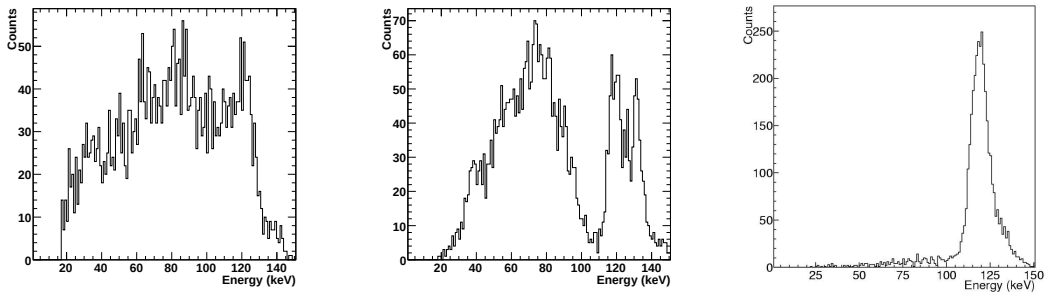

Figure 4-28: Spectra from single-sided charge-sharing CZT strip detector (UNH-EV-SUB04). 500μm beam spot located between row 6 column 5 and row 7 column 5. (a) Spectrum of unit cell at row 6 column 5. (b) Spectrum of unit cell at row 7 column 5. (c) Spectrum of added unit cells, i.e row 6 column 5 and row 7 column 5.

4.4.8 Photopeak Detection Efficiency

For a given detector, detection efficiency values depend on the type and the energy of the incident radiation. For charged particles, many detectors have a counting efficiency close to 100% since these particles interact whenever they enter the detector volume. This is different for incident gamma-rays or other uncharged radiation.

The intrinsic efficiency is calculated using the following formula (Knoll, 2000)

$$\epsilon_{int} = \frac{\text{number of pulses recorded}}{\text{number of photons incident on detector}}. \tag{4.3}$$

The detection efficiency of a 7.5 mm single-sided charge-sharing CZT strip detector is calculated for 122, 356 and 662 keV photons. For this purpose, we used ^{57}Co, ^{133}Ba and ^{137}Cs sources to illuminate the entire CZT surface 12 cm away from the crystal surface. To eliminate edge effects, we chose a unit cell at the middle of the detector, i.e., row 5 column 5. We found the number of pulses recorded in this cell. The number of photons incident on the detector is calculated by the following formula

$$N_{in} = \frac{3.7 \times 10^4}{4\pi} \frac{N_0 \times t \times A}{d^2} \tag{4.4}$$

Table 4.4: Photopeak detection efficiency of single-sided charge-sharing CZT strip detector (UNH-EV-SUB04).

Energy (keV)	**Experimental**	**Simulated**
122	55.6 ± 7.5%	92.6%
356	24.2 ± 4.9%	33.1%
662	11.0 ± 3.3%	23.4%

where N_0 is the activity of the radioactive source in micro Curie (μCi), t is the duration in seconds of the experiment, A is the detector area (here it is unit cell area, 1.225 mm^2) and d is the distance between source and the detector, 12 cm. The source activity, calibrated by the manufacturer, has an error of 3%.

We used GEANT4 for simulations, which are set up so that only the unit cell is illuminated 12 cm away from the detector using a point source at different energies.

Results can be seen in Table 4.4 and Figure 4-29. The experimental efficiency values are on average 20% lower than the calculated theoretical values. The discrepancy is largely due to imaging efficiency. As reported previously, limited charge sharing among the row and column contact pads results in the identification of either the row and column but not both for $\sim$ 36% of the events (Dönmez et al., 2005). Dead time measured with the test pulse is about 2μs. Verger et al. (2001) calculated 74% detection efficiency at 122 keV for $4 \times 4 \times 6$mm^3 CZT detector. The calculated detection efficiency from Kargar et al. (2006) is 52% and 11% are 122 and 662 keV for $3.4 \times 3.4 \times 5.7$mm^3 CZT detector, respectively.

4.5 Discussion

In this chapter, we discussed the characterization experiments with UNH's strip detector designs. These are the orthogonal coplanar CZT strip detector and the single-sided charge-sharing CZT strip detector. These designs use the advantage of the "small pixel effect"

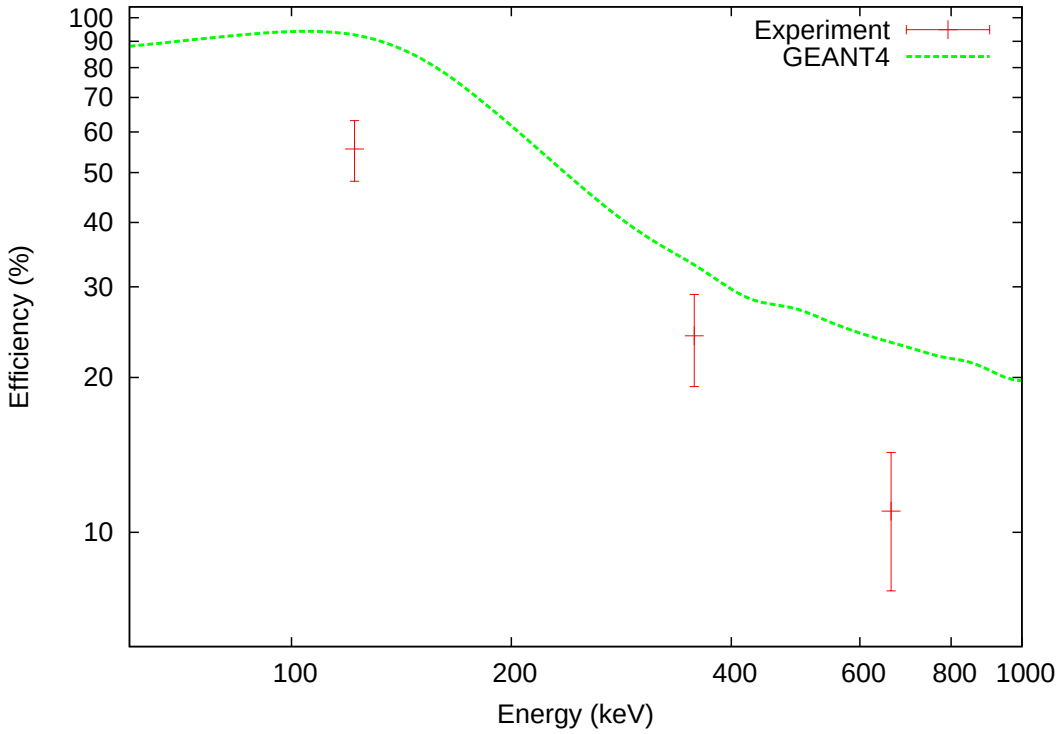

Figure 4-29: Detection efficiency calculations for single-sided charge-sharing CZT strip detector. GEANT4: Simulated detection efficiency. Points are the experimental detection efficiency.

to eliminate the hole contribution since trapping of holes degrades the spectroscopy and imaging efficiency of CZT detectors. We performed spectroscopy, imaging, uniformity and efficiency calculations. We summarize the following points:

1. We performed spectroscopy measurements with both detector designs and obtained results comparable to those of pixellated detectors. The charge collection on the strip columns was the main problem encountered with orthogonal coplanar detectors. The non-uniform behavior is also evident (as with other CZT detectors) and the charge sharing problem is again identified as the root problem.

2. The new design which operates on the principle of charge sharing between row and column signals was proposed by Macri et al. (2003). This design simplifies the front-end electronics, because the same shaping and polarity is used for both rows and

columns. The disadvantage is that the energy resolution is degraded by a factor related to electronic noise, since row and column signals must to be summed to measure energy.

3. Charge sharing plays an important role in the imaging process of single-sided charge-sharing CZT strip detector design. The limited charge sharing due to the small size of the electron cloud for some events results in a measurement of only x or y. This will reduces the imaging efficiency.

4. The 3-D imaging capabilities of detectors were studied using a ^{57}Co source and a tungsten collimator with different beam spot sizes. Both designs show millimeter or better imaging resolution in spatial dimension (x and y) and a sub-millimeter imaging resolution in z dimension. We also confirmed our depth calculation by calculating the attenuation length of 122 keV photons. The results are in good agreement with theoretical and simulated values.

5. The detection efficiency of single-sided charge-sharing CZT strip detector design was calculated and compared to the theoretical values. The difference between these values can be due to threshold issued or the electron trapping in the detector material. The imaging efficiency also defines a threshold value for detection efficiency. Non-uniformity of the material could result in high efficiency cell adjacent to low efficiency cells. Only one cell was tested here and could be a chance low efficiency cell.

Chapter 5

Multi-Hit Simulations

5.1 Introduction

In this chapter, we discuss the simulations of multi-hits in CZT detectors. Determination and understanding of multi-hits is important because it directly affects the imaging capabilities of our strip detectors. It also effects spectroscopic performance. A short review of GEANT4 (GEometry ANd Tracking V.4) and simulation setup is also given.

5.2 GEANT4

GEANT4 is an object oriented simulation toolkit based on C++ for the passage of particles through matter (Allison et al., 2006). It has following components for a complete simulation:

- Geometry of the system.
- Materials included in the system.
- Fundamental particles (generation, tracking).
- Interaction of particles with matter.
- Response of the detector to the particles.
- Event generation.

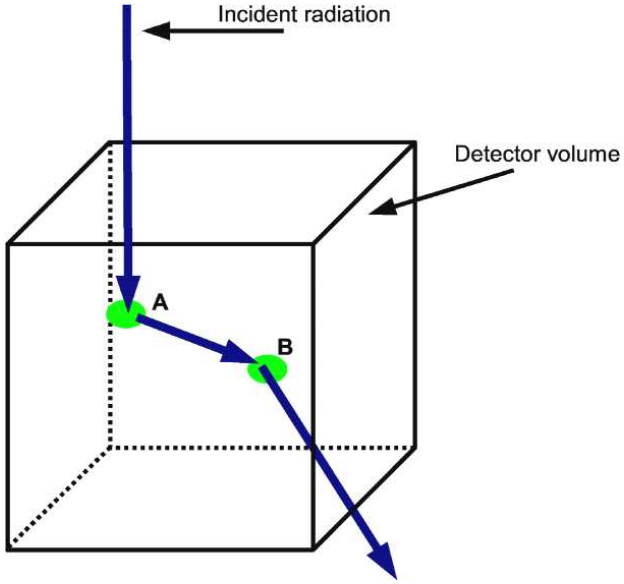

Figure 5-1: Example of double-hit event in CZT.

- Visualisation and analysis tools.

The geometry and material properties of the detector and the physical processes important in the detector are defined by the user.

5.3 Multi-hit Definition

Photoelectric absorption and Compton scattering are the most important photon interaction processes to consider when studying multi-hits in CZT detectors at energies below 1 MeV. Incident photons interact with the detector by either of these processes. When the interaction is Compton scattering, the photon transfers some of its energy to the electron. The scattered photon may interact again with the detector through another Compton scattering or photoelectric absorption. Figure 5-1 shows an example double-hit event. The incident photon interacts through a Compton scattering at point A and creates a charge cloud (green). The scattered photon then interacts through another Compton scattering at point B. Due to the applied electric field, the charge clouds will be collected in the anode. We define a double-hit event as one where charge clouds are collected in two different unit

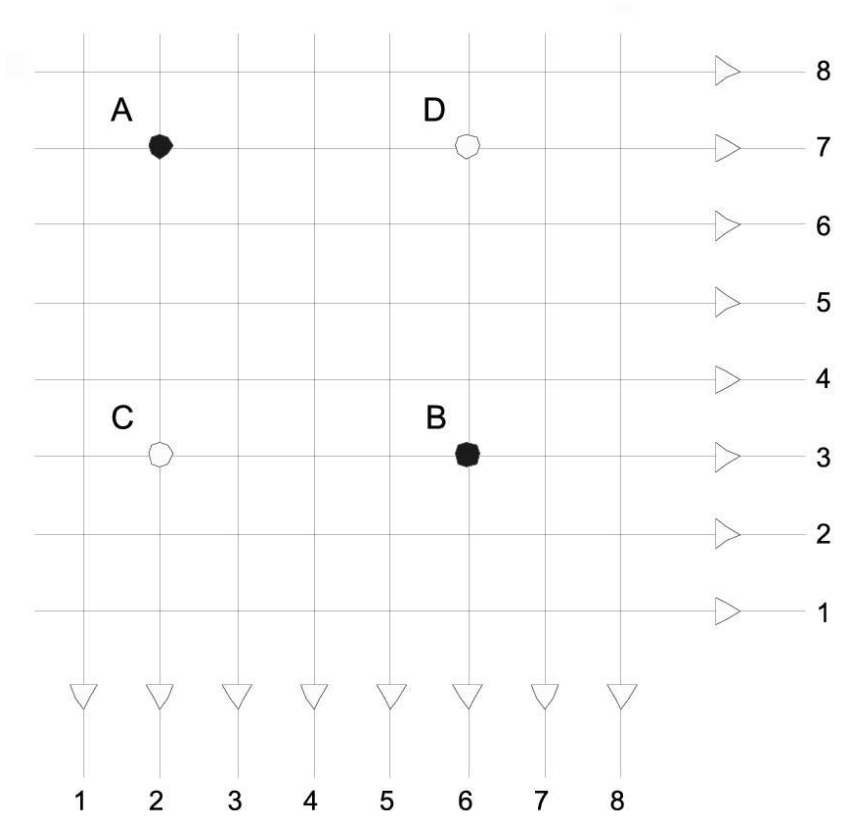

Figure 5-2: Illustration of double-hit ambiguity in strip detectors (Macri et al., 2004).

cells in the detector. Therefore, the incident photon energy cannot be measured correctly unless there is a mechanism to identify and correct the double-hit events. We see incomplete charge collection in the spectrum.

Double-hits present a measurement ambiguity for imaging with strip detectors as illustrated in Figure 5-2. In this figure, interactions at points A and B could be interpreted as having occurred at points C and D. Unless there is some mechanism to associate the row with the column for each hit, there will be an ambiguity in the identification of the interaction sites. Independent measurements of the relative arrival time of both column and row signals can be effective unless the interactions occur at the same depth. This would come with the cost of introducing another data field for each electronics channel. If, however, the row and column pulse heights are correlated, pulse height information can be used to

almost entirely eliminate this ambiguity. A and B would be identified as the true locations in this example as column, row (2, 7) and (6, 3) record the same pulse height.

5.4 Simulation Setup

For these multi-hit simulations, we used following procedures:

- CdZnTe detector with size $15 \times 15 \times 7.5\text{mm}^3$ placed in vacuum.
- Unit cell (1.225mm^2) in the center is randomly illuminated with gamma-ray photons from 60 to 1000 keV with 60 keV increments.
- GLECS (Kippen, 2004) package for low energy Compton scattering is used in the simulations. Physical processes included are photoelectric effect, Compton scattering, gamma conversion (pair production) and Rayleigh scattering.
- All events data are written to a text file for further analysis to search for mulhi-hits. For this purpose a C++ program was written to analyse the data file generated from GEANT4.

The following method was used to determine the multi-hits. For every event, we checked whether we had a Compton scattering. If we had a Compton scattering, we examined the next interaction. The event was considered a multi-hit if it satisfied the following two conditions. First, the second interaction must be observed outside the unit cell of the first Compton scattering interaction. Second, the deposited energy at the second interaction site must be larger than the 15 keV minimum energy detectable with our detectors.

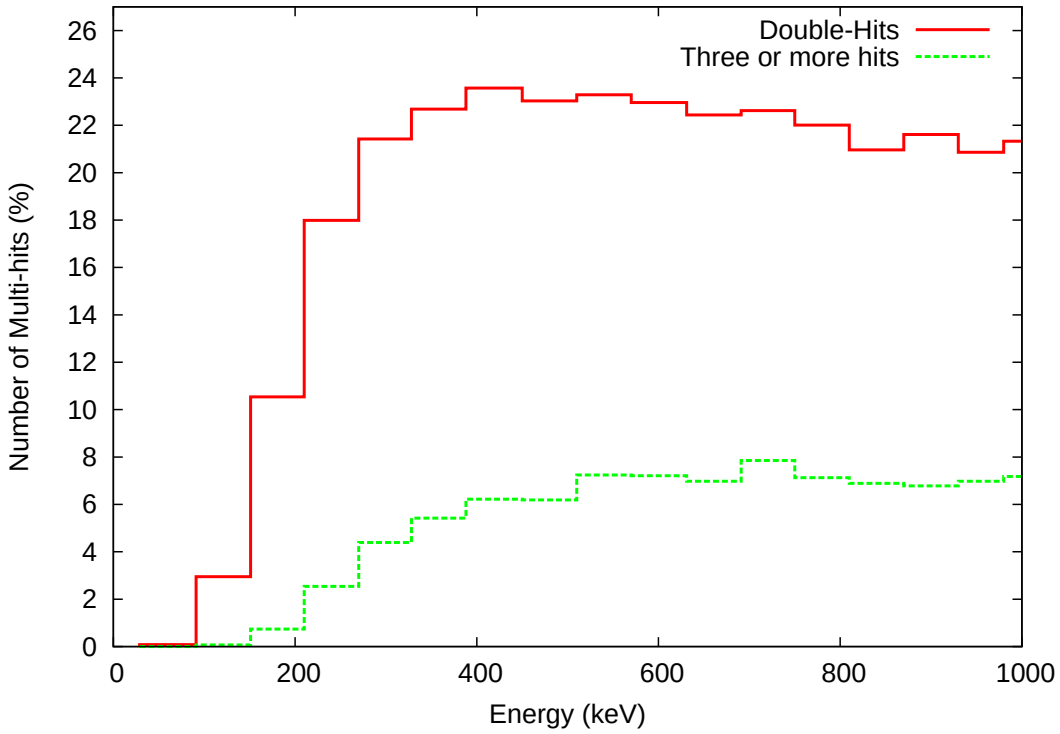

Figure 5-3: Multi-hit percentage vs. incident photon energy. Detector size is $15 \times 15 \times 7.5\text{mm}^3$.

5.5 Simulation Results

We performed a series of simulations as described above. Calculated multi-hit percentage can be seen in Figure 5-3. The number of double-hits dramatically increases at $\sim$ 300 keV where Compton scattering becomes important in CZT. Figure 5-4 shows the relative positions of the double-hit events in the lateral (x-y) dimension. Double-hits are seen across the full detector area for incident photon energies greater than 300 keV. Figures 5-5 and 5-6 show the distance between the first interaction site and the double-hit position for fully absorbed events in x-y and z, respectively. From Figure 5-5, it can also be seen that for lower energies (122, 300 and 356 keV) at least half of the double-hit events occur adjacent to the unit cell in which the first interaction takes place, but for higher energies (e.g. 662 and 1000 keV) double-hit locations become more uniformly distributed. The mean distances of double-hit events for all events can be seen in Figure 5-7.

To check the consistency of the simulation results, we used the flood run data from a single-sided charge-sharing CZT strip detector (UNH-EV-SUB04) at 122, 356 and 662 keV photons from radioactive sources. To compare, we only look for the double-hit events with fully absorbed energies. The number of double-hits in experimental data is found as follows. We selected events above 15 keV threshold at row 5 column 5, i.e. unit cell at the center, equivalent to the simulations. Then, we looked at all unit cells having a signal larger than the threshold value. We summed the unit cell signal with these signals. If the summed signal resides in the photopeak, we counted that event as a double-hit. The comparison results are shown in Figure 5-8. This agreement of simulated and measured results provides confidence in the validity of the simulation tools. The differences between these values can be due to the low efficiency at higher energies.

The effect of double-hits on the spectrum for 662 keV photons can be seen in Figure 5-9. We can see that number of events under the photopeak for double-hit events is comparable to the number of events having only a single hit, reflecting the fact that Compton scatters are important at 662 keV. However, suppress in of the Compton tail is effective for multi-hits. Figure 5-10 shows spectra from 122 keV photons. The effect of double-hits on the spectrum is almost negligible since only $\sim 3\%$ of total events has a double-hit. We can see that all events having a double-hit, deposited all their energy to the detector.

5.6 Discussion

In this chapter, we discussed the simulation efforts on the multi-hit interactions in CZT. In general, multi-hits create an ambiguity for imaging with strip detectors. It will be difficult to locate true event location unless some specific techniques are applied to the detection system, such as making timing measurement or using specific spectroscopy algorithms (Lehner et al., 2003). The photopeak efficiency of the detector will also be

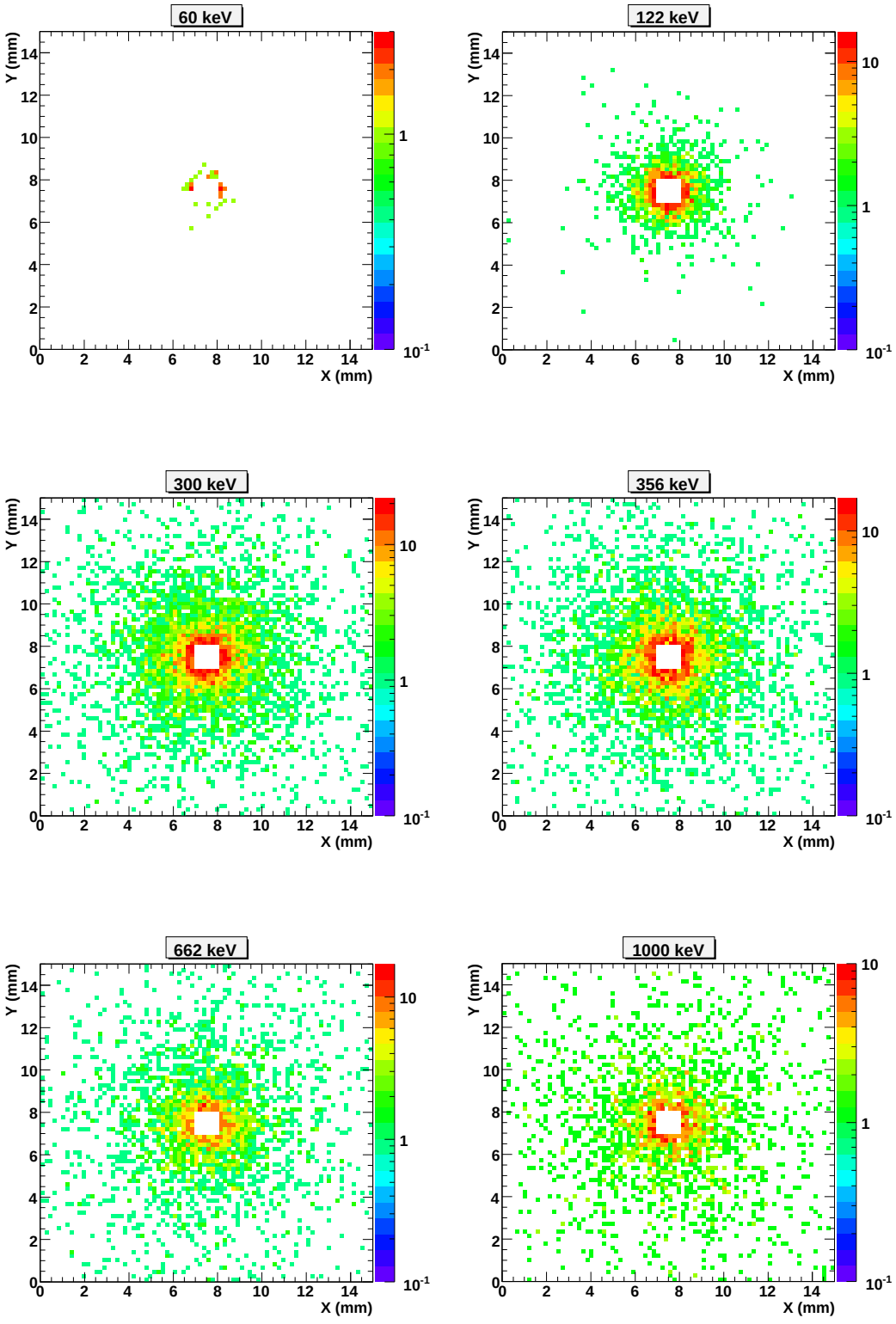

Figure 5-4: Selected simulated double-hit positions in x-y.

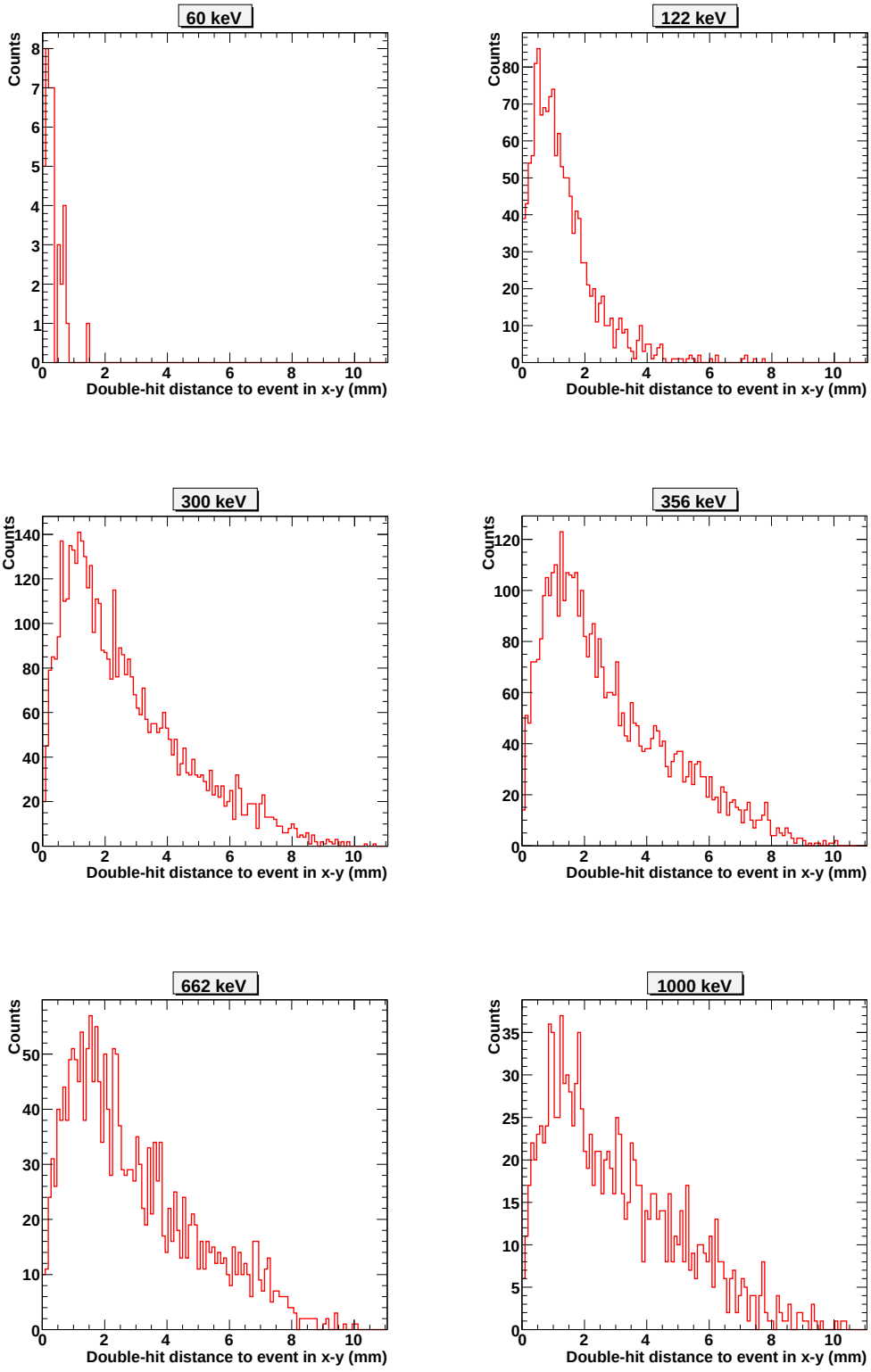

Figure 5-5: Selected simulated double-hit distances to the first hit in x-y for fully absorbed events.

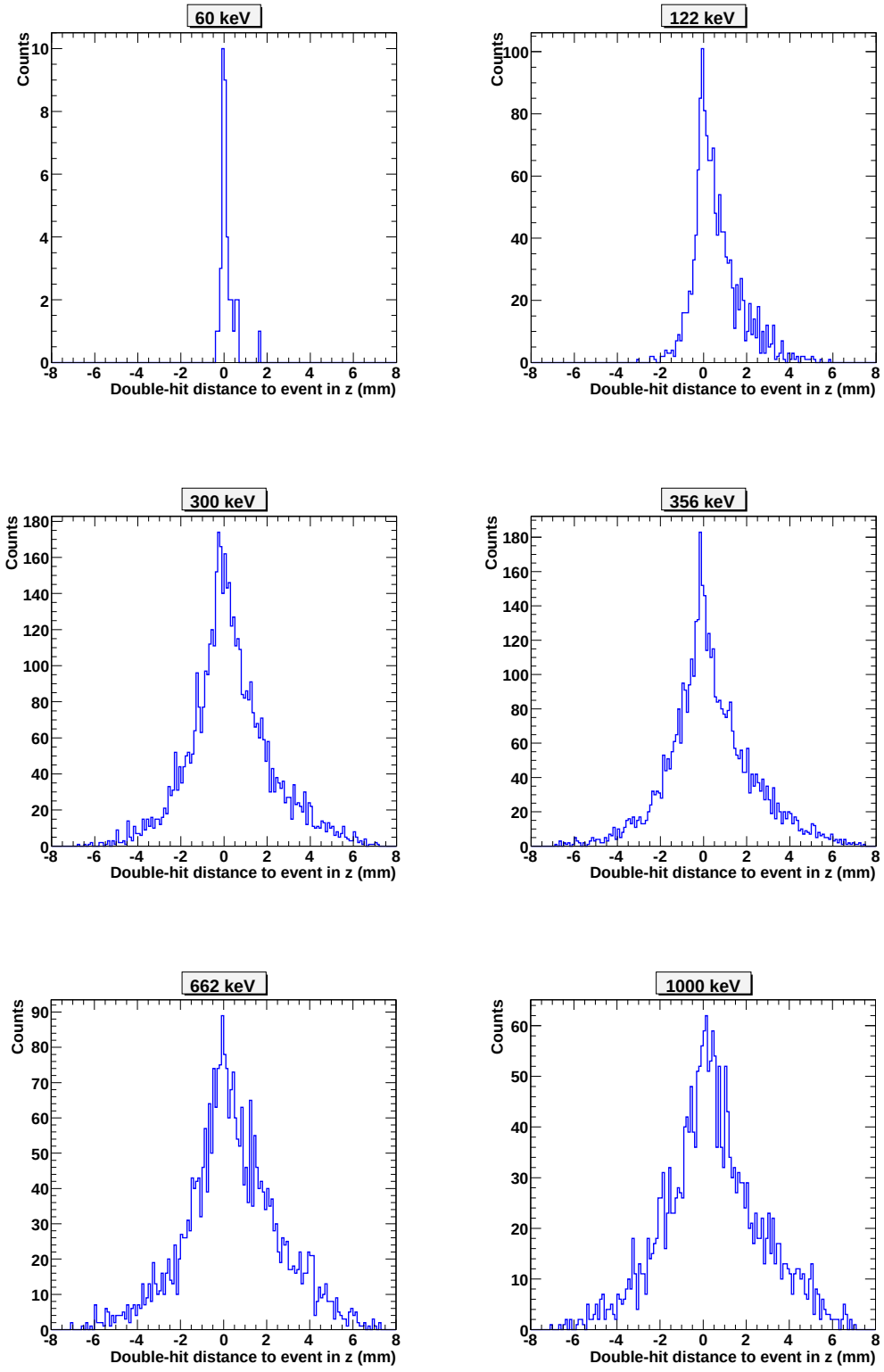

Figure 5-6: Selected simulated double-hit distances to the first hit in z for fully absorbed events.

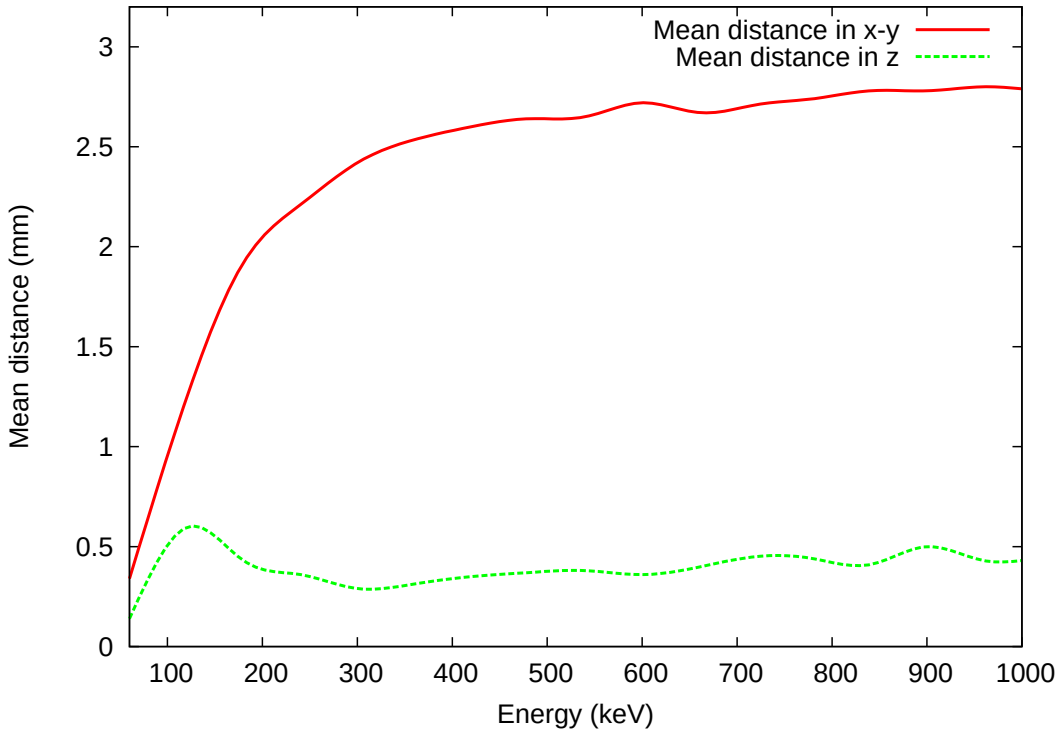

Figure 5-7: Mean distances of double-hit locations to the first interaction site for all events.

reduced since, the unit cell will measure wrong energy of the incident photon.

We illuminate the centered unit cell to investigate the double-hit events in our detectors. It is observed that the multi-hit percentage increases $\sim$ 300 keV when Compton scattering becomes important in CZT and stays up to 1000 keV. Another important property is that the position of double-hits are close to the unit cell is in question. This can also be seen in the mean distance measurement in three dimensions. The mean distance in spatial dimension suggests that unit cell size should be $\sim$ 2.8 mm to eliminate most double-hit events in the energy range between 60 keV to 1 MeV.

We calculated number of double-hits for fully absorbed energies, i.e., photopeak events only, to check the validity of multi-hits. The simulation data are confirmed with the experimental data. The fluctuations might be due to the efficiency differences between these measurements. The spectrum of 662 keV photons reveals that a sum of all energy deposits of double-hit events will increase the photopeak efficiency of the detector.

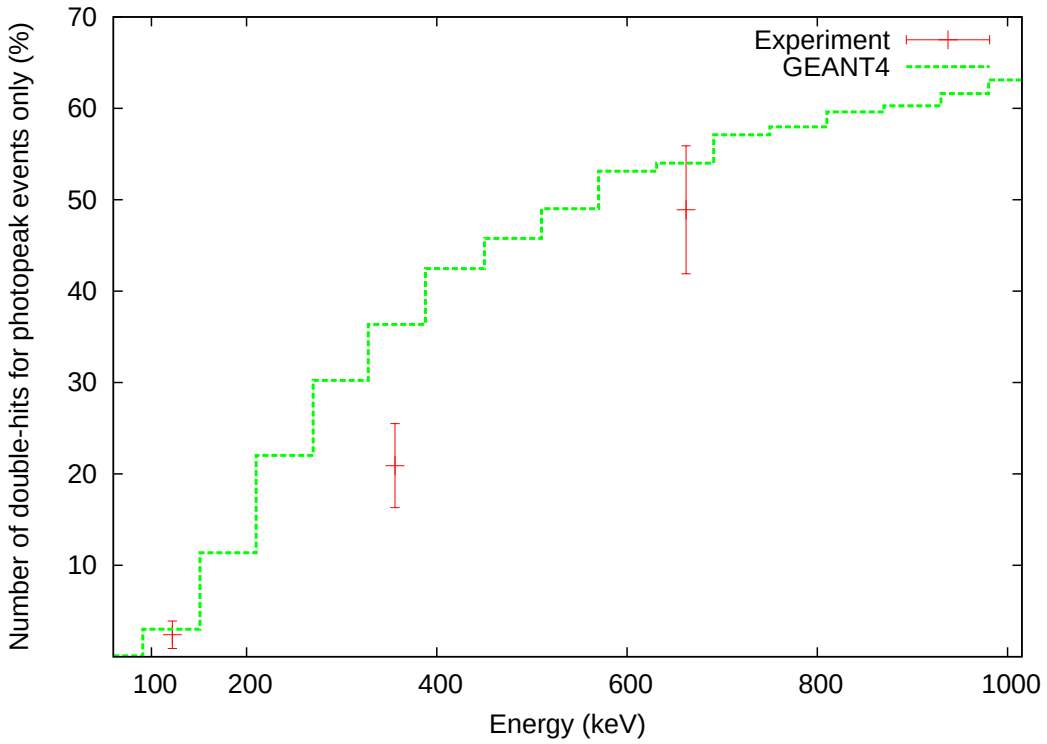

Figure 5-8: Comparison of double-hit events for photopeak events with experiment and simulation.

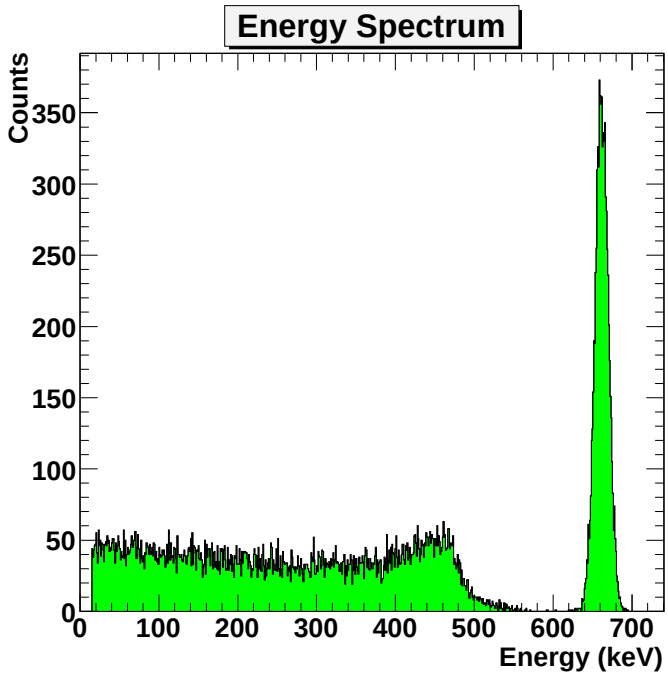

(a)

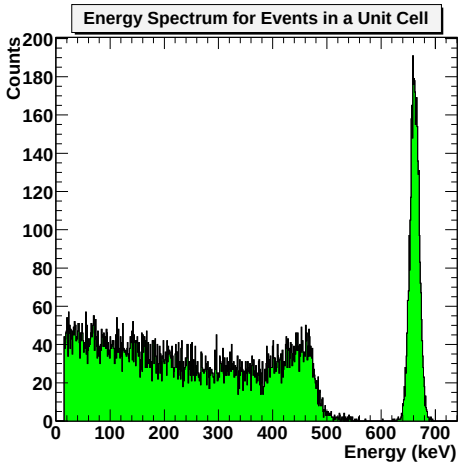

(b)

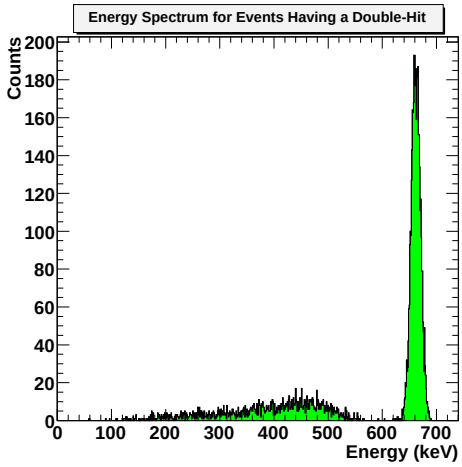

(c)

Figure 5-9: Simulated energy spectrum including electronic noise component for all (a), for single hit (b) and for double-hit (c) events at 662 keV.

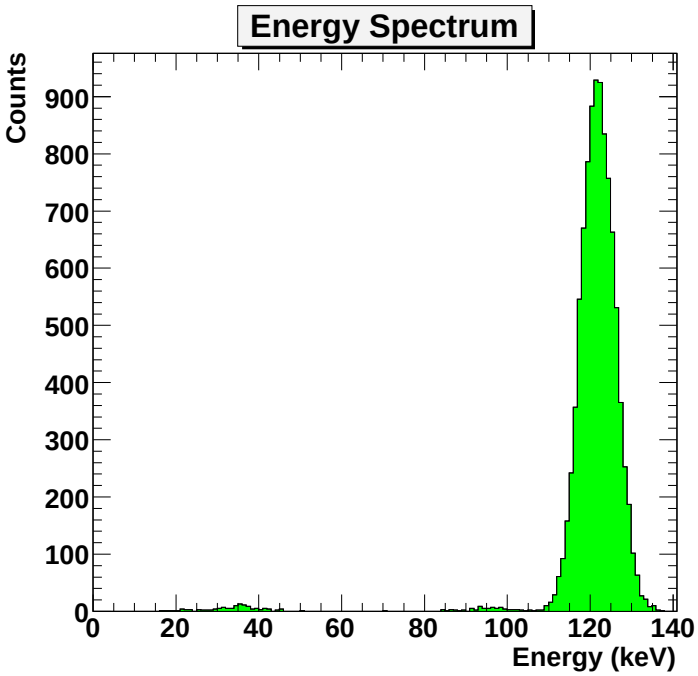

(a)

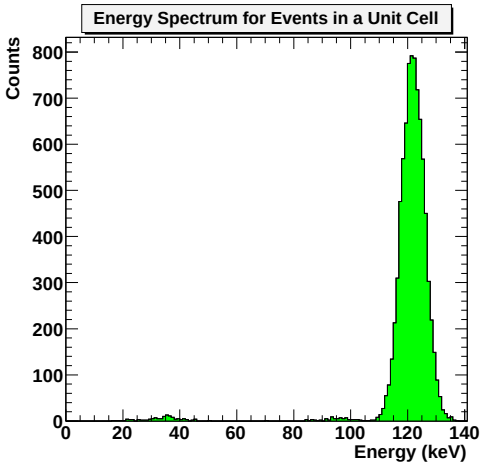

(b)

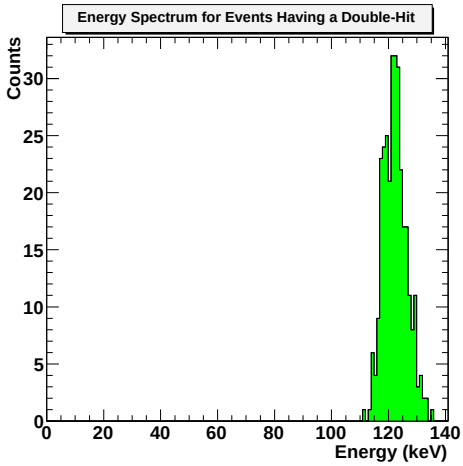

(c)

Figure 5-10: Simulated energy spectrum including electronic noise component for all (a), for single hit (b) and for double-hit (c) events at 122 keV.

Chapter 6

Discussions and Conclusions

In this thesis, the characterization experiments for two different CZT strip detector design, i.e. non-charge-sharing orthogonal coplanar and charge-sharing were presented. Results of studies of multi-hit simulations were also presented.

The orthogonal coplanar CZT strip detector (non charge-sharing design) consists of 64 1.0 mm^2 unit cells. Each unit cell consists of a 200μm diameter pixel contact surrounded by a strip contact as shown in Figure 4-1.

The single-sided charge-sharing CZT strip detector has 121 $\sim$ 1.5 mm^2 unit cells. Each unit cell contains an array of closely packed contact pads in two intermingled groups as shown in Figure 4-6.

Experiments with orthogonal coplanar CZT strip detector investigated spectroscopy, uniformity and 3-D imaging. The measured energy resolutions (FWHM) are 5.2% and 1.3% at 122 and 662 keV, respectively. These results compare well with pixellated detectors. These results do not include any depth correction to the spectra that should further improve the energy resolution. In the ideal case, the non-collecting strip columns do not collect charge but they sense the movement of electrons when they move towards the pixel rows. The main problem encountered with this design is the unintended charge collection on strip columns as confirmed with beam spot and slit collimator studies. This effect reduces the level of the pixel row trigger signal and produces a systematically lower energy measurement. Charge collection on the strip columns also affects the uniformity of the detector to the

incident radiation. The problem becomes more complicated due to non-uniformity of the detector material or surface contacts.

Using a 1.0 mm beam spot and a 1.0 mm wide slit collimator, the uniformity of the non-charge sharing orthogonal coplanar CZT strip detector was studied. The spot collimator scan showed a dip at strip column 1 in the detector which implies that the charge collection on this strip is more important than the other strips. the same effect was also identified and studied with the slit collimator. We scanned the detector in x and y dimension to identify possible regions for charge collection on strips. The scan results showed non-uniform response in some of the pixel rows and strip columns. After that, we used same conditions to the strip signals and pixel signals, i.e. same shaping and applied voltage. In this way, strip columns are also set to collect charge. Our results showed that charge collection on strip column reduced the level of the pixel signal degrading the energy resolution (see Figure 4-26(c) and 4-26(d)). Charge collection on strips is due to their large area compared to the pixels.

The spectroscopy performance of the single-sided charge-sharing strip detector was not as good as the orthogonal coplanar strip detector. This is mainly due to the addition of row and column signals to obtain energy information. The measured energy resolutions with this detector are 7.8% and 3.0% at 122 and 662 keV, respectively. This design has advantages over the non-charge sharing strip detector. Most significantly, rows and columns are using the same shaping and also the same applied voltage. This will simplify the custom electronics. Also unwanted charge collection will be minimized since there is no large area strip columns. Imaging efficiency is a significant issue with this design. The limited charge sharing due to the small size of the electron cloud results for some events in a measurement of only the x or y coordinate, not both, and, at least for the first prototype detectors, reduce the detection efficiency for imaging measurements. The measured imaging efficiency

is 64% at 122 keV. This behavior can also be explained by looking the scatter plots of row and column signals. In ideal charge-sharing detector, events on the scatter plots should accumulate near the center of the main diagonal with comparable signals in both row and column. However, our studies showed that a significant number of events for which most or all of the charge is collected on the row or column only. One way to increase the imaging efficiency is to reduce the pitch sizes of the contact pads within the unit cell.

3-D imaging capability of both detector design using 122 keV photons with a beam spot were studied. In this study, the beam spot is incident on the cathode surface at an angle from the normal or z- axis. We observed that the beam spot passes through several unit cells. Spatial resolution is better than the unit cell pitch in the x and y dimension, and less than 1 mm in the z dimension for both designs. We also calculated the depth of interaction, i.e. attenuation length at 122 keV. For depth measurements, we used the ratio of the cathode to maximum anode signal. The measured attenuation length values are 2.00 ± 0.16 mm and 2.03 ± 0.01 mm for orthogonal coplanar strip detector and single-sided charge-sharing strip detector, respectively. These results are in agreement with the theoretical value, 2.01 mm.

Detection efficiency for photopeak events was also calculated for single-sided charge-sharing CZT strip detector. For this purpose the detector was illuminated with a radioactive source 12 cm away. We only calculated efficiency for the centered unit cell to avoid the edge effects. This unit cell also has a good response to the incident radiation. The discrepancy between measured and simulated efficiencies are largely due to imaging efficiency. As reported previously, limited charge sharing among the row and column contact pads results in the identification of either the row and column but not both for $\sim 36\%$ of the events. Reducing the pitch sizes of the contact pads within the unit cell will help to increase the detection efficiency.

Multi-hits present a measurement ambiguity for imaging with strip detectors. Unless there is some mechanism to associate the row with the column for each hit, there will be an ambiguity in the identification of the interaction sites. To understand the effect of multi-hits, we performed series of simulations of the energy range between 60 keV to 1 MeV. The number of double-hits dramatically increases about 300 keV where Compton scattering becomes important. When we look at the double-hit events with fully absorbed energies wee see the following. Most of the double-hits are concentrated on the neighboring unit cells. The calculated mean distance between interaction sites for double-hit events increases monotonically up to 400 keV, then stay almost constant. Multi-hits also lead to the erroneous energy calculation unless they are corrected. We saw that the number of events under the photopeak for double-hit events at 662 keV is comparable to the number of events having only a single hit, reflecting the fact that Compton scatters are important at this energy. From this, we can also say that the photopeak efficiency is degraded due to the multi-hit interactions. This implies that determining the multi-hits and correcting them is crucial for improving the performance of the detector.

In conclusion, the performance of our detectors are comparable with that of the pixellated detectors. We believed that our spectroscopy and imaging results meet the current requirements for instrumentation. The major goal in developing high energy astrophysics X- and γ-ray instruments is to combine good detector spectral resolution for spectroscopy and good position sensitivity for imaging. The quality of the detector material is very important to improve the performance. The bonding processes used for electrical and mechanical connection for the detector also affects the performance. Therefore, our results are limited by the quality of crystal and bonding processes of the manufacturers.

In the future, we can extend our simulations to a more realistic detector, i.e. including anode geometry, electronic noise. We can optimize the size of the detector by changing

the detector size, thickness and anode geometry. This will help us to design new prototype detectors. Since, resolving the multi-hit interactions will increase the performance of the detector in spectroscopy, imaging and efficiency, we will need an addition to our current data analysis tools to correct them.

The results from single-sided charge-sharing detectors are promising for the usability of these detectors. The main problem encountered with these detector is the uniformity since not all the unit cells show good spectroscopic performance. We observed that two row signals (X0 and X1) showing strong correlation with applied voltage on the z-grid. When there is a voltage on the z-grid, these rows show an additional photopeak in the spectrum, approximately two times the photopeak of the radioactive source. This additional photopeak (ghost peak) moves towards the lower energy when we lower the applied voltage on z-grid. We suspect that surface leakage current or non uniformity of the crystal can be the source of the problem.

As we stated earlier, the current size of the pads limits the imaging efficiency and also photopeak detection efficiency of single-sided charge-sharing CZT strip detector. The first simulation results by Hamel and Benoit (2006) with smaller pad sizes (150μm) have shown improvement for charge sharing between row and column signals in favor to ideal charge sharing case. This preliminary result implies that the fabrication of new detectors with smaller pad sizes for unit cells will increase the imaging efficiency of the single-sided charge-sharing CZT strip detectors. Therefore, next step should be the fabrication of new prototype detector with smaller pad sizes.

Bibliography

Allison, J., Amako, K., Apostolakis, J. and et al. (2006), 'Geant4 developments and applications', *IEEE Trans. Nucl. Sci.* **53**, 270.

Amman, M. and Luke, P. N. (1997), 'Coplanar-grid detector with single-electrode readout', *Proc. SPIE* **3115**, 205.

Amman, M. and Luke, P. N. (1999), 'Optimization criteria for coplanar-grid detectors', *IEEE Trans. Nucl. Sci.* **46**, 205.

Anger, H. O. (1958), 'Scintillation camera', *The Review of Scientific Instruments* **29**, 27.

Band, D. L. (1995), 'BATSE observations of gamma ray bursts', *AIP Conv. Proc.* **384**, 123.

Barrett, H. H., Eskin, J. D. and Barber, H. B. (1995), 'Charge transport in arrays of semiconductor gamma-ray detectors', *Phys. Rev. Lett.* **75**, 156.

Barthelmy, S. D. (2000), 'The burst alert telescope (BAT) on the swift MIDEX mission', *Proc. SPIE* **4140**, 50.

Bolotnikov, A. E., Camarda, G. C., Wright, G. W. and James, R. B. (2005), 'Factors limiting the poerformance of CdZnTe detectors', *IEEE Trans. Nucl. Sci.* **52**, 589.

Butler, J. F., Lingren, C. L. and Doty, F. P. (1992), '$Cd_{1-x}Zn_xTe$ gamma ray detectors', *IEEE Trans. Nucl. Sci.* **39**, 605.

Caroli, E., Stephen, J. B., Cocco, G. D., Natalucci, L. and Spizzichino, A. (1987), 'Coded aperture imaging in x- and gamma-ray astronomy', *Space Science Reviews* **45**, 349.

Cavalleri, G., Gatti, E., Fabri, G. and Svelto, V. (1971), 'Extension of Ramo's theorem as applied to induced charge in semiconductor detectors', *Nucl. Instr. & Meth.* **92**, 137.

Dabrowski, A. J. and Huth, G. C. (1978), 'Toward the energy resolution limit of mercuric iodide in room temperature low energy x-ray spectrometry', *IEEE Trans. Nucl. Sci.* **NS-25**, 205.

Dönmez, B., Macri, J. R., McConnell, M. L., Ryan, J. M., Widholm, M., Narita, T. and Hamel, L.-A. (2005), 'Further studies of single-sided sharge-sharing CZT strip detectors', *Proc. SPIE* **5922**, 62.

Eichler, D., Livio, M., Piran, T. and Schramm, D. N. (1989), 'Nucleosynthesis, neutrino bursts and gamma-rays from coalescing neutron stars', *Nature* **340**, 126.

El-Hanany, U., Shahar, A. and Tsigelman, A. (1999), 'CZT pixel detector modules for medical imaging and nuclear spectroscopy', *Presented at 11^{th} International Workshop on Room Temperature Semiconductor X- and Gamma-Ray Detectors and Associated Electronics, Vienna, Austria* .

Eskin, J. D., Barrett, H. H. and Barber, H. B. (1999), 'Signals induced in semiconductor gamma-ray imaging detectors', *J. Appl. Phys.* **85**, 647.

Evans, R. D. (1955), *The Atomic Nucleus*, McGraw-Hill, New York.

Fano, U. (1946), 'On the theory of ionization yield of radiations in different substances', *Phys. Rev.* **70**, 44.

Fano, U. (1947), 'Ionization yield of radiations. II. Fluctuations of the number of ions', *Phys. Rev.* **72**, 26.

Fernando, P., Arnaud, M., Briel, U. and et al. (2006), 'Simbol-X: mission overview', *Proc. SPIE* **6266**, 62660F–1.

Fraser, G. W. (1989), *X-Ray Detectors in Astronomy*, Cambridge Astrophysics Series, Cambridge.

Frisch, O. (1944), *British Atomic Energy Report* **BR-49**.

Gehrels, N., Chincarini, G., Giommi, P. and et al. (2004), 'The SWIFT gamma-ray burst mission', *Astrophys. J.* **611**, 1005.

Grindlay, J. E. (2005), 'EXIST:All-sky hard X-ray imaging and spectral-temporal survey for black holes', *New Astronomy Reviews* **49**, 436.

Hamel, L.-A. and Benoit, M. (2006), *in private communications* .

Hamel, L.-A. and Paquet, S. (1996), 'Charge transport and signal generation in CdTe pixel detectors', *Nucl. Instr. & Meth. A* **380**, 238.

He, Z. (2001), 'Review of the Shockley-Ramo theorem and its application in semiconductor gamma-ray detectors', *Nucl. Instr. & Meth. A* **463**, 250.

He, Z., Li, W., Knoll, G. F. and Wehe, D. K. (1999), '3-D position sensitive CdZnTe gamma-ray spectrometers', *Nucl. Instr. & Meth. A* **422**, 173.

Iyudin, A., Diehl, R., Bloemen, H., Hermsen, W., Lichti, G., Morris, D., Ryan, J., Schönfelder, V., Steinle, H., Varendorff, M., de Vries, C. and Winkler, C. (1994), 'COMPTEL observations of ^{44}Ti gamma-ray line emission from Cas A', *Astron.Astrophys.* **284**, L1–L4.

Jen, C. K. (1941), 'On the induced current and energy balance in electronics', *Proc. of the I.R.E.* **29**, 345.

Jordanov, V. T., Macri, J. R., Clayton, J. E. and Larson, K. A. (1999), 'Multi-electrode CZT detector packaging using polymer flip chip bonding', *Presented at 11th International Workshop on Room Temperature Semiconductor X- and Gamma-Ray Detectors and Associated Electronics, Vienna, Austria* .

Julien, M. and Hamel, L.-A. (2001), *in private communications* .

Kargar, A., Jones, A. M., McNeil, W. J., Harrison, M. J. and McGregor, D. S. (2006), 'CdZnTe Frisch collar detectors for gamma-ray spectroscopy', *Nucl. Instr. & Meth. A* **558**, 497.

Kippen, R. M. (2004), 'The GEANT low energy Compton scattering (GLECS) package for use in simulating advanced Compton telescopes', *New Astronomy Reviews* **48**, 221.

Knödlseder, J. and Vedrenne, G. (2000), 'Science prospects for SPI', *Proceedings of the 4^{th} INTEGRAL Workshop 'Exploring the Gamma-Ray Universe', Alicante, Spain, 4-8 September 2000 Associated Electronics, Vienna, Austria* p. 23.

Knoll, G. F. (2000), *Radiation Detection and Measurement*, third edn, John Wiley & Sons.

Koglin, J. E., Christensen, F. E., Craig, W. W., Decker, T. R., Hailey, C. J., Harrison, F. A., Hawthorn, C., Jensen, C. P., Madsen, K. K., Stern, M., Tajiri, G. and Taylor, M. D. (2005), 'NuSTAR hard X-ray optics', *Proc. SPIE* **5900**, 590000X–1.

Kouveliotou, C., Meegan, C. A., Fishman, G. J., Bhat, N. P., Briggs, M. S., Koshut, T. M., Paciesas, W. S. and Pendleton, G. N. (1993), 'Identification of two classes of gamma ray bursts', *Astrophys. J.* **413**, L101.

Larson, K., Jordanov, V., McConnell, M. L., Macri, J. R., Ryan, J. M., Drake, A., Hamel, L.-A. and Tousignant, O. (2000), 'Analog processing of signals from a CZT strip detector with orthogonal coplanar anodes', *Proc. SPIE* **4141**, 336.

Lehner, C. E., He, Z. and Knoll, G. F. (2003), 'Intelligent gamma-ray spectroscopy using 3-D position-sensitive detectors', *IEEE Trans. Nucl. Sci.* **50**, 1090.

Léna, P., Lebrun, F. and Mignard, F. (1998), *Observational Astrophysics*, second revised edn, Springer.

Leo, W. R. (1994), *Techniques for Nuclear and Particle Physics Experiments : A How-to Approach*, second edn, Springer-Verlag.

Li, W., He, Z., Knoll, G. F., Wehe, D. K. and Du, Y. F. (2000), 'A modeling method to calibrate the interaction depth in 3-D position sensitive CdZnTe gamma-ray spectrometers', *IEEE Trans. Nucl. Sci.* **47**, 890.

Longair, M. S. (1992), *High Energy Astrophysics. Volume 1. Particles, photons and their detection*, second edn, Cambridge University Press, Cambridge.

Luke, P. N. (1994), 'Single-polarity charge sensing in ionization detectors using coplanar electrodes', *Appl. Phys. Lett.* **65**, 2884.

Luke, P. N. (1995), 'Unipolar charge sensing with coplanar electrodes – Application to semiconductor detectors', *IEEE Trans. Nucl. Sci.* **42**, 207.

Luke, P. N., Amman, M. and Lee, J. S. (2000), 'Coplanar grid CdZnTe detectors with three-dimensional position sensitivity', *Nucl. Instr. & Meth. A* **439**, 611.

Luke, P. N., Amman, M., Tindall, C. and Lee, J. S. (2003), 'Recent developments in semiconductor gamma-ray detectors', *Lawrence Berkeley National Laboratory* **LBNL-52403**. http://repositories.cdlib.org/lbnl/LBNL-52403.

Macri, J. R., Dönmez, B., Widholm, M., Hamel, L.-A., Julien, M., Narita, T., Ryan, J. M. and McConnell, M. L. (2004), 'Single-sided CZT strip detectors', *Proc. SPIE* **5501**, 208.

Macri, J. R., Hamel, L.-A., Julien, M., Miller, R. S., Dönmez, B., McConnell, M. L., Ryan, J. M. and Widholm, M. (2003), 'Single-sided CZT strip detectors', *Nuclear Science Symposium Conference Record, 2003, IEEE* **5**, 3385.

Malm, H. L. (1972), 'A mercuric iodide gamma-ray spectrometer', *IEEE Trans. Nucl. Sci.* **NS-19**, 263.

Matteson, J. L., Coburn, W., Duttweiler, F., Gassaway, T. M., Heindl, W. A., Leblanc, P. C., MacDonald, D., Pelling, M. R., Peterson, L. E., Rothschild, R. E., Skelton, R. T., Hink, P. L. and Crabtree, C. (1996), 'CdZnTe strip detectors for high energy X-ray astronomy', *Proc. SPIE* **2859**, 58.

McConnell, M. L., Macri, J. R., Ryan, J. M., Larson, K., Hamel, L.-A., Bernard, G., Pomerleau, C., Tousignant, O., Leroux, J.-C. and Jordanov, V. (2000), 'Three-dimensional imaging and detection efficiency performance of orthogonal coplanar CZT strip detectors', *Proc. SPIE* **4141**, 157.

Moss, C. E., Ianakiev, K. D., Prettyman, T. H., Smith, M. K. and Sweet, M. R. (2001), 'Multi-element, large volume CdZnTe detectors', *Nucl. Instr. & Meth. A* **458**, 455.

Mueller, B., O'Connor, M. K., Blevis, I., Rhodes, D. J., Smith, R., Collins, D. A. and Phillips, S. W. (2003), 'Evaluation of a small cadmium zinc telluride detector for scintimammography', *The Journal of Nuclear Medicine* **44**, 602.

Parnham, K. B., Grosholz, J., Davis, R. K., Vydrin, S. and Cupec, C. A. (2001), 'Development of a CdZnTe-based small field of view gamma camera', *Proc. SPIE* **4508**, 134.

Prantzos, N. and Diehl, R. (1996), 'Radioactive ^{26}Al in the galaxy: observations versus theory', *Phys. Rep.* **267**, 1.

Quadrini, E. M., Conti, G., D'Angelo, S., Fiorini, M., Uslenghi, M., Natalucci, L. and Ubertini, P. (2005), 'CZT detectors for a new generation gamma-ray telescopes', *Proc. SPIE* **5898**, 58980O.

Ramo, S. (1939), 'Currents induced by electron motion', *Proc. of the I.R.E.* **27**, 584.

Redus, R. H., Pantazis, J. A., Huber, A. C., Jordanov, V. T., Butler, J. and Apotovsky, B. (1997), *"Semiconductors for Room-Temperature Radiation Detector Applications II," Material Research Society Symposium Proceedings: Semiconductors for Room-Temperature Radiation Detector Applications II, (eds. R.B. James, et. al.)* **487**, 101.

Rothschild, R. E., Heindl, W. A., Matteson, J. L. and Pelling, M. R. (2003), 'Design and performance of a ruggedized large-area CZT detector module for hard X-ray astronomy', *Nucl. Instr. & Meth. A* **505**, 126.

Ryan, J. M., Dönmez, B., Macri, J. R., McClish, M., McConnell, M. L., Miller, R. S., Widholm, M., Hamel, L.-A. and Julien, M. (2003), 'Development of CZT strip detector modules for 0.05 to 1 MeV gamma-ray imaging and spectroscopy', *Proc. SPIE* **4851**, 885.

Ryan, J. M., Macri, J. R., McConnell, M. L., Dann, B. K., Cherry, M. L., Guzik, T. G., Doty, F. P., Apotovsky, B. A. and Butler, J. F. (1995), 'Large area sub-millimeter resolution CdZnTe strip detector for astronomy', *Proc. SPIE* **2518**, 292.

Rybicki, G. B. and Lightman, A. P. (1979), *Radiative Processes in Astrophysics*, Wiley-VCH.

Schmidt, M. (2001), 'Luminosities and space densities of short gamma-ray bursts', *Astrophys. J.* **559**, L79.

Shockley, W. (1938), 'Currents to conductors induced by a moving point charge', *J. Appl. Phys.* **9**, 635.

Shor, A., Eisen, Y. and Mardor, I. (1999), 'Optimum spectroscopic performance from CZT γ- and X-ray detectors with pad and strip segmentation', *Nucl. Instr. & Meth. A* **428**, 182.

Stahle, C. M., Parsons, A., Bartlett, L. M., Kurczynski, P., Krizmanic, J. F., Barbier, L. M., Barthelmy, S. D., Birsa, F., Gehrels, N., Odom, J., Palmer, D., Sappington, C., Shu, P., Teegarden, B. J. and Tueller, J. (1996), 'CdZnTe strip detector for arc second imaging and spectroscopy', *Proc. SPIE* **2859**, 74.

Takahashi, T. and Watanabe, S. (2001), 'Recent progress in CdTe and CdZnTe detectors', *IEEE Trans. Nucl. Sci.* **48**, 950.

van Paradijs, J., Kouveliotou, C. and Wijers, R. A. M. J. (1995), 'Gamma-ray burst afterglows', *Annu. Rev. Astron. Astrophys* **38**, 379.

Verger, L., Boitel, M., Gentet, M. C., Hamelin, R., Mestais, C., Mongellaz, F., Rustique, J. and Sanchez, G. (2001), 'Characterization of CdTe and CdZnTe detectors for gamma-ray imaging applications', *Nucl. Instr. & Meth. A* **458**, 297.

Whited, R. C. and Schieber, M. M. (1979), 'Cadmium telluride and mercuric iodide gamma radiation detectors', *Nucl. Instr. & Meth.* **162**, 113.